

UNIVERSIDADE DE SÃO PAULO
ESCOLA DE ENGENHARIA DE SÃO CARLOS

DANIEL JARDÓN ÁLVAREZ

Study of advanced ion conducting polymers
by relaxation, diffusion and spectroscopy NMR methods

São Carlos
2016

DANIEL JARDÓN ÁLVAREZ

Study of advanced ion conducting polymers
by relaxation, diffusion and spectroscopy NMR methods

This thesis presented to the Graduate program in Materials Science and Engineering at the Universidade de São Paulo to obtain the degree of Doctor of Science.

Concentration area:
Development, Characterization and Material Application.

Advisor:
Prof. Dr. Tito José Bonagamba

Corrected Version

(Original version available at the program unit)

São Carlos
2016

AUTHORIZE THE REPRODUCTION AND DISSEMINATION OF TOTAL OR PARTIAL COPIES OF THIS DISSERTATION OR THESIS, BY CONVENTIONAL OR ELECTRONIC MEDIA FOR STUDY OR RESEARCH PURPOSE, SINCE IT IS REFERENCED.

Jardón Álvarez, Daniel

J37s

Study of advanced ion conducting polymers by relaxation, diffusion and spectroscopy NMR methods/
Daniel Jardón Álvarez; orientador Tito José Bonagamba.
São Carlos, 2016.

Tese (Doutorado) - Programa de Pós-Graduação em
Ciência e Engenharia de Materiais e Área de
Concentração em Desenvolvimento, Caracterização e
Aplicação de Materiais -- Escola de Engenharia de São
Carlos da Universidade de São Paulo, 2016.

1. NMR. 2. Polymer Electrolytes. 3. Relaxometry. 4.
Chemical Exchange. 5, Diffusion. I. Título

FOLHA DE JULGAMENTO

Candidato: Químico **DANIEL JARDON ALVAREZ**.

Título da tese: "Estudo de polímeros condutores iônicos avançados com métodos de relaxação, difusão e espectroscopia por RMN".

Data da defesa: 11/08/2016.

Comissão Julgadora:

Resultado:

Prof. Titular **Tito José Bonagamba**
(Presidente)
(Instituto de Física de São Carlos/IFSC)

Aprovado

Prof. Associado **José Pedro Donoso Gonzalez**
(Instituto de Física de São Carlos/IFSC)

aprovado

Prof. Titular **Hellmut Eckert**
(Instituto de Física de São Carlos/IFSC)

aprovado

Prof. Associado **Said Rahnamaye Rabbani**
(Instituto de Física/IF-USP)

Aprovado

Prof. Dr. **Gerson Luiz Mantovani**
(Universidade Federal do ABC/UFABC)

APROVADO

Coordenador do Programa de Pós-Graduação em Ciências e Engenharia de Materiais:

Prof. Titular **Antonio José Felix de Carvalho**

Presidente da Comissão de Pós-Graduação:
Prof. Associado **Luis Fernando Costa Alberto**

ACKNOWLEDGMENTS

I would like to thank everyone who has helped and supported me during the elaboration of this thesis.

First, my advisor Prof. Tito Bonagamba for his support, trust and help throughout this thesis. His mentorship and guidance are greatly appreciated.

Prof. Klaus Schimdt-Rohr for receiving me in his laboratory and for giving me great scientific and academic advices.

My friends and colleagues from the LEAR group Arthur, Camila, Christian, Elton, Everton, Mariane, Roberson and Rodrigo. For the friendship, the support, the scientific discussions, for always being willing to help and for making our lab a great place.

The technicians of our group Aparecido, João and Edson for their great efforts and help with anything related to NMR instrumentation.

Furthermore, Prof. Didier Gimes, Trang Phan and Bérengère Pelletier from the University of Marseille for sending us the triblock copolymers and for showing me their laboratory. Prof. Éder Tadeu Gomes Cavalheiro and Priscila Cervini Assumpção from the IQSC/USP for the DSC measurements. My friends and colleagues from the OSU.

My family Ana, Teresa and Jesus whom I missed a lot, while being far from home. They always believed in me and supported me.

A special thanks to Pamela for her love, comprehension and patience and for always staying by my side.

And finally, CAPES for the scholarship.

ABSTRACT

JARDON ALVAREZ, D. **Study of advanced ion conducting polymers by relaxation, diffusion and spectroscopy NMR methods.** 115p. Tese (Doutorado) –Escola de Engenharia de São Carlos, Universidade de São Paulo, São Carlos, 2016.

Advances on secondary lithium ion batteries imply the use of solid polymer electrolytes, which represent a promising solution to improve safety issues in high energy density batteries. Through dissolution of lithium salts into a polymeric host, such as poly(ethylene oxide) (PEO), ion conducting polymers are obtained. The Li^+ ions will be localized in the proximity of the oxygen atoms in the PEO chains and thus, their motion strongly correlated with the segmental reorientation of the polymer. Nuclear magnetic resonance (NMR) spectroscopy, translational diffusion coefficients and transverse relaxation times (T_2) contribute to the understanding of the involved structures and the ongoing dynamical processes in ionic conductivity. Nuclei with different motional freedom can present different T_2 times. $T_2 \times T_2$ exchange experiments enable studying exchange processes between nuclei from different motional regimes. In this work, three different ion conducting polymers were studied. First, PEG was doped with different amounts of LiClO_4 . ^7Li NMR relaxometry measurements were done to study dynamical behavior of the lithium ions in the amorphous phase. All samples presented two lithium types with clearly differentiated T_2 times, indicating the presence of two regions with different dynamics. The mobility and consequently the T_2 times, increases with temperature. It was observed, that the doping ratio strongly influences the dynamics of the lithium ions, as the amount of crystalline PEG is reduced while increasing the polarity of the sample. A local maximum of the mobility was observed for $y = 8$. With the $T_2 \times T_2$ exchange experiments exchange rates between both lithium sites were quantified. Second, the triblock copolymer PS-PEO-PS doped with LiTFSI was studied with high resolution solid state NMR techniques as well as with ^7Li relaxometry measurements. $T_{1\rho}$ and spin diffusion measurements gave insight on the influence of the doping and the PS/PEO ratio on the mobility of the different segments and on interdomain distances of the lamellar phases. Third, multiple quantum diffusion measurements were applied on poly(ethylene glycol) distearate (PEGD) doped with LiClO_4 . Therefore, triple quantum states of the $3/2$ nucleus ^7Li were excited. After optimizing the experimental procedure, it was possible to obtain reliable diffusion coefficients using triple quantum states.

Keywords: NMR. Polymer electrolytes. Relaxometry. Chemical exchange. Diffusion.

RESUMO

JARDON ALVAREZ, D. **Estudo de polímeros condutores iônicos avançados com métodos de relaxação, difusão e espectroscopia por RMN.** 115p. Tese (Doutorado) – Escola de Engenharia de São Carlos, Universidade de São Paulo, São Carlos, 2016.

O avanço da tecnologia em baterias secundárias de íons lítio envolve o uso de polímeros condutores iônicos como eletrólitos, os quais representam uma solução promissora para obter baterias de maior densidade de energia e segurança. Polímeros condutores são formados através da dissolução de sais de lítio em uma matriz polimérica, como o poli(óxido de etileno) (PEO). Os íons de lítio estão localizados próximos aos oxigênios do PEO, de tal forma que seu movimento está correlacionado com a reorientação das cadeias poliméricas. Espectroscopia por Ressonância magnética nuclear (RMN), junto com medidas de difusão translacional e tempos de relaxação transversal (T_2) contribuem para elucidar as estruturas e os processos dinâmicos envolvidos na condutividade iônica. Núcleos com diferente liberdade de movimentação podem ter tempos de T_2 diferentes. Experimentos de $T_2 \times T_2$ permitem correlacionar sítios de diferentes propriedades dinâmicas. Neste trabalho, três diferentes polímeros condutores iônicos foram estudados. Primeiro, PEG foi dopado com LiClO_4 . As propriedades dinâmicas dos íons lítio na fase amorfa foram estudadas com medidas de relaxometria por RMN do núcleo ^7Li . Todas as razões de dopagem apresentaram dois T_2 diferentes, indicando dois tipos de lítio com dinâmica diferente. A mobilidade, e consequentemente os tempos T_2 aumentam com aumento da temperatura. Foi identificado que a dopagem fortemente influencia a dinâmica dos íons lítio, devido à redução da fase cristalina PEG e o aumento da polaridade na amostra. Um máximo local da mobilidade foi observado para $y = 8$. Com o experimento $T_2 \times T_2$ foram quantificadas as razões de troca entre os dois tipos de lítio. Segundo, o copolímero tribloco PS-PEO-PS dopado com LiTFSI foi analisado através de técnicas de RMN de estado sólido de alta resolução assim como através de medidas de relaxação de ^7Li . Medidas de $T_{1\rho}$ e difusão de spin mostraram a influência da dopagem e da razão PS/PEO na mobilidade dos diferentes segmentos e nas distâncias interdomínio das fases lamelares. Terceiro, medidas de difusão através de estados de múltiplos quanta foram feitas em diesterato de polietileno glicol (PEGD) dopado com LiClO_4 . Estados de triplo quantum foram criados no núcleo ^7Li , spin $3/2$. Após garantir a eficiência das ferramentas desenvolvidas, foi possível obter coeficientes de difusão confiáveis.

Palavras-chave: RMN. Eletrólitos Poliméricos. Relaxometria. Troca química. Difusão.

LIST OF ABBREVIATIONS

3Q	Triple Quantum
BPP	Bloembergen Pound Purcell
CP	Cross Polarization
CPMG	Carr-Purcell-Meiboom-Gill
DSC	Differential Scanning Calorimetry
FID	Free Induction Decay
FWHM	Full Width at Half Maximum
ILT	Inverse Laplace Transform
MAS	Magic Angle Spinning
MQ	Multiple Quantum
NMR	Nuclear Magnetic Resonance
PEG	Poly(ethylene glycol)
PEGD	Poly(ethylene glycol) distearate
PEO	Poly(ethylene oxide)
PFG	Pulse Field Gradient
PS	Polystyrene
RMSD	Root-Mean-Square Deviation
rf	Radio Frequency
SE	Spin Echo
SPE	Solid Polymer Electrolyte
STE	Stimulated echo
TEM	Transmission Electron Microscopy
TOSS	Total Suppression of Spinning Sidebands

CONTENTS

1	Introduction.....	15
2	Theoretical Background.....	19
2.1	Ion Conducting Polymers	19
2.1.1	Basic Concepts of Polymers	19
2.1.2	Solid Polymer Electrolytes	20
2.2	Nuclear Magnetic Resonance	24
2.2.1	Basic Principles of NMR Spectroscopy	24
2.2.2	NMR Spectroscopy Experiments	37
2.3	Relaxation in NMR.....	42
2.3.1	Theory of Relaxation	42
2.3.2	NMR Relaxometry Experiments	51
2.4	Translational Diffusion.....	55
2.4.1	Self-Diffusion in NMR	55
2.4.2	NMR Diffusion Measurements.....	56
3	Experimental.....	61
3.1	Sample Preparation	61
3.2	Measurements and Data Processing	62
4	Results and Discussion	65
4.1	PEG/LiClO ₄	65
4.1.1	DSC.....	65
4.1.2	Relaxation	67
4.2	Solid Triblock Copolymer Electrolyte PS-PEO-PS/LiTFSI.....	80
4.2.1	The Polymer PS-PEO-PS	80
4.2.2	The Salt LiTFSI	85
4.3	PEGD Multiple Quantum Coherence Diffusion Measurements	93

4.3.1	^7Li NMR Spectroscopy of PEGD-LiClO ₄ ($y = 5$).....	93
4.3.2	Multiple Quantum Coherence Excitation.....	94
4.3.3	Multiple Quantum Coherence Detection.....	96
4.3.4	Multiple Quantum Pulse Gradient Measurements	99
5	Conclusions and Outlook	103
	REFERENCES.....	109

1 Introduction

One of the biggest challenges in modern materials science and engineering is to develop new materials, which satisfy the increasing demand on production, storage and transport of energy. High volumetric and gravimetric energy density and lightweight make lithium ion batteries interesting for these applications. (1-2) Lithium metal batteries (where lithium metal is the anode material) are of great interest, since they present the highest energy density among the different types of batteries. (3) Nevertheless, due to dendrite formation, this type of battery is related with serious safety issues: dendrite formation can lead to short-cuts and destruction of the battery. (3) An approach to overcome this safety issue is the use of solid polymer electrolytes, since electrolytes with large mechanical stability can avoid dendrite formation. (4)

Since the discovery of ionic conductivity in PEO/Na⁺ (PEO, poly(ethylene oxide)) in 1975 by Wright (5) and the subsequent suggestion by Armand (6) of using ion conducting polymers as solid electrolytes in lithium ion batteries, this research field has attracted a lot of interest in the scientific community. (7–11) Conducting polymers via lithium ions present various advantages as electrolytes in batteries such as safety and higher design flexibility. Nevertheless, it is still a challenge to improve their electrochemical properties. (12)

The mechanical stability of PEO is not sufficient to completely avoid dendrite formation. In this context, synthesis of block copolymers becomes interesting, since it allows combining components with different properties. For instance, in the triblock copolymer PS-PEO-PS, ionic conductivity is guaranteed by the PEO block, in which salts can be dissolved, while the polystyrene (PS) blocks account for mechanical stability. (4,13–18) Commonly, an improvement in ionic conductivity, obtained by an increment of the PEO percentage in the copolymer comes along with a decrease of mechanical stability. (13) Consequently, it is necessary to find a compromise between good ionic conduction and sufficient mechanical resistance avoiding dendrite formation.

Nuclear Magnetic Resonance (NMR) is a powerful method for the characterization of substances. The development of the magic-angle spinning (MAS) technique has turned the acquisition of high-resolution solid-state spectra routinely possible. The parameters obtained from NMR experiments, such as chemical shifts, relaxation times, quadrupolar coupling constants, lineshapes, diffusion coefficients or exchange rates are sensitive to the coordination environment surrounding the observed nuclei and the dynamical processes they are involved

in. (19-20) This makes NMR a useful experimental tool, which allows studying the charge carrier as well as the host matrix of ion conducting materials independently. From those studies, it is possible to obtain information such as kind and number of diffusing ions, activation energies, jump rates or correlation effects, as well as structural and morphological properties. (20-21)

Transverse relaxation is mediated by fluctuations of the local magnetic fields in proximity of the nuclei. These fluctuations originate from the rotational and translational motions of the nuclei. In this way, nuclei with different motional freedom can have different transverse relaxation times (T_2). The CPMG technique (named after they developers Carr-Purcell-Meiboom-Gill) (22-23) allows measuring T_2 relaxation time distributions. Measurements of T_2 relaxation times can contribute to understand the dynamic processes involved in ionic conductivity. (20)

The two-dimensional exchange experiment $T_2 \times T_2$, obtained by concatenating two CPMGs and its one-dimensional variants, (24–27) allow to correlate sites with different transverse relaxations. This makes it possible to obtain information on the possible diffusive paths, and even to characterize their specific exchange rates. (26) Relaxation exchange, in contrast to conventional Fourier transform exchange experiments, does not require different precession frequencies of the involved sites but different relaxation rates. In many cases, heterogeneities of the sample do not reflect on chemical shift differences. Relaxation exchange experiments have mainly gain popularity in the field of porous media such as reservoir rocks, (24,28-29) cements, (30) bones (31) or ceramics, (27) but have also been used in a large variety of areas, like biological tissue (32-33) or proton exchange membranes. (34) To our knowledge, they have not been used to characterize the ions in polymer electrolytes. The here presented ion conducting polymers present a ^7Li spectrum with signals with strongly overlapping chemical shifts, while the T_2 relaxation time distribution clearly differentiates two sites.

The use of pulse field gradients (PFG) in NMR allows measuring translational diffusion coefficients, which are important for understanding ionic conductivity in this type of materials. (20,35-36) An interesting property of the isotope ^7Li is that its nucleus possesses an electric quadrupole moment. It is possible to measure diffusion coefficients using multiple quantum (MQ) states. (37–40) This technique can represent an advantage in systems with slow diffusions, such as the encountered in ion conducting polymers, since the sensibility of the NMR diffusion measurement is proportional to the square of the quantum number of the involved species. However, in order to being able to benefit from this property it is necessary that the orientation of the polymeric chains presents high order. This is the case for the

triblock copolymer Poly(ethylene glycol-400) distearate (PEGD) doped with large amounts of LiClO_4 , which presents order in the polymer matrix even at temperatures above the melting temperature.

Goal of this Thesis

The Li-doped ion conductor poly(ethylene glycol) PEG has, between the glass transition temperature (T_g) and the melting point (T_m), at least two phases, vitreous and crystalline. Being the first the principal responsible for the ionic conductivity. In the first part of this work, we apply NMR relaxometry techniques aiming to develop a methodology for studying the Li^+ ions in the amorphous phase. In particular, we propose the use of ^7Li T_2 relaxation time measurements to study dynamical behavior of the lithium ions and the use of $T_2 \times T_2$ exchange experiments, to quantify exchange rates between the two different found Li^+ sites.

In a second part, after validating the relaxometry techniques, we aim to apply them to a more advanced material, of higher complexity, Li-doped triblock copolymers based on poly(ethylene oxide). The triblock copolymer PS-PEO-PS has promising properties for applications as solid polymer electrolyte in lithium metal batteries. It has a lamellar structure, where aliphatic and polar chains form separated layers. Before applying the previously studied relaxometry techniques, it was necessary to gain knowledge about morphological and structural properties of these samples. Therefore, they were studied with high-resolution solid-state NMR techniques. Spin diffusion experiments allowed determining domain sizes of the heterogeneous segments of the block copolymer. Rotating frame relaxation ($T_{1\rho}$) allowed studying dynamical processes of the spectroscopic distinguishable phases. With the combination of the results from ^1H and ^{13}C spectroscopy and ^7Li relaxation measurements, we hope to gain new insights on the mechanisms involved in the ion conduction in the polymer matrix.

To accomplish those goals, we decided to establish various collaborations. The group of Prof. Didier Gigmes from the *Aix-Marseille Université*, specialized in the technique of controlled radical polymerization, (17-18) synthesized the triblock copolymers. In a one-week visit to their laboratories, I had the chance to get to know group and facilities. Furthermore, during a four-month visit at the *Iowa State University* I had the opportunity to learn various

NMR spectroscopy techniques applied on polymers in the group of Prof. Klaus Schmidt-Rohr.

In the last part of this thesis, we explore the application of a different NMR experiment, multiple quantum pulse field gradient diffusion measurement, to the field of solid polymer electrolytes. The efficiency of the developed tools, which allow manipulating the spin system, was guaranteed through a theoretical and experimental study. This made it possible to do translational diffusion measurements using triple quantum states on the ion conducting polymer PEGD doped with LiClO_4 .

2 Theoretical Background

2.1 Ion Conducting Polymers

2.1.1 Basic Concepts of Polymers

Polymers are macromolecules of large molecular weight composed of repeat units. They could be either organic, inorganic or even hybrids, but in this work we will focus only on organic polymers. The molecular weight of a polymer will depend on the molecular weight of the repeat unit and the number of times it repeats. Due to the polymerization process polymers could have strong heterogeneity in the degree of polymerization, or polydispersity. Therefore, the polymer molecular weight will be given as an average value of the sample. (41)

There are multiple ways the repeat units can be aligned along the chains. This alignment will strongly affect their chemical, physical and mechanical properties. They can be aligned as linear polymers without ramifications, forming single chains. If the main chains present some ramifications, they are called branched polymers. In crosslinked polymers the main chains are joined one to another by the ramifications at various points. (41)

If a polymer has more than one repeat unit, it is termed copolymer. Copolymers are of great interest for material scientists since the combination of various monomers can lead to new and exclusive properties. The physicochemical and mechanical properties of a copolymer will depend on the way the repeat units are arranged. The different types of copolymers are: alternating, random, block and graft copolymers and are summarized in Figure 1 for a copolymer composed of two repeat units. (41)

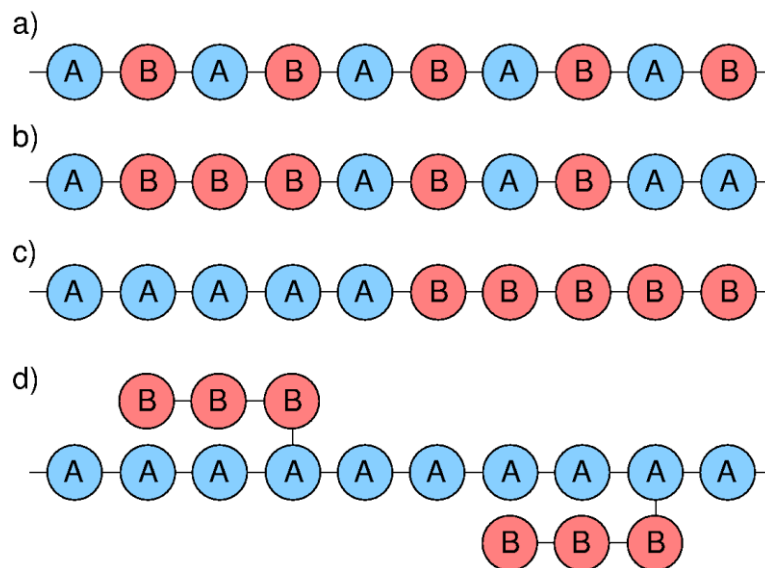


Figure 1 - Schematic representations of a) alternating, b) random, c) block and d) graft copolymers composed of two repeat units A and B.

Source: By the author.

Crystallinity in polymers is complex due to the magnitude of the involved molecules. As a consequence of their size and heterogeneity polymers are often semicrystalline, which means they are partially crystalline and partially amorphous. Besides the chemical composition and the molecular structure (linear polymers have a higher tendency to crystallize), the degree of crystallinity of a polymer depends strongly on its thermal history. (41) Furthermore, the presence of chemical distinct phases, in block copolymers or in semicrystalline systems can lead to self-organized systems with microphase-separated structures. The morphology and the domain size of the segregated phases will depend on their ratio and nature. Typical encountered morphologies are spherical, cylindrical, double gyroidal or lamellar. (42-43)

2.1.2 Solid Polymer Electrolytes

Introduction

Among the various types of batteries, lithium metal batteries (where lithium metal is the anode material) present the highest energy density. (3) Nevertheless, after various cycles, formation of dendrites can occur, which implies a high safety issue, since dendrites will lead to short-cuts and destruction of the battery. (3) Consequently, various solutions to overcome this problem appeared. For instance, *Sony Energytech Inc.* commercialized in 1996 the first rechargeable lithium battery using lithiated carbon (LiC_6), as the anode material. (3) The use

of carbon instead of lithium metal reduced considerably the high security risks related to the later one. On the downside, the substitution of the anode material reduced the energy density of the electrochemical devices. Therefore, another approach involved replacing the liquid electrolyte by a solid electrolyte, which could mechanically avoid the formation of dendrites and allow the use of lithium metal as anode. In this context ion conducting polymers represent a promising option as electrolytes of high ionic conductivity paired with mechanical robustness and were therefore termed solid polymer electrolytes (SPE) (3).

PEG/PEO doped with Lithium Salts

In 1975 Wright (5) first reported ionic conductivity in a polymer-salt system, PEO/Na⁺ (PEO, poly(ethylene oxide)). Soon after, Armand (6) suggested the use of ion conducting polymers as solid electrolytes in rechargeable batteries. The presence of oxygen atoms in the PEO (or PEG, poly(ethylene glycol)) structure makes the chains polar, allowing good dissolution of lithium ions in its matrix. The salt concentration in this type of systems is commonly given by the oxygen to lithium ratio $y = [\text{O}]/[\text{Li}]$.

It has been reported that ionic conductivity mainly occurs in the amorphous phase (above the glass transition temperature T_g) (44) and efforts to avoid crystallization have been done ever since. The mobility of the chains enable translational diffusion of the ions in the solid polymer, turning it a good ion conductor and thus a potential electrolyte. Since the lithium ions are close to the PEO oxygen atoms, it is believed that its dynamics are strongly correlated to segmental reorientations of the polymer. (45) But actually, much is still unknown on the chemical structure and ion transport in PEO. (3)

The chain mobility is strongly correlated to the glass transition temperature of the polymer, after which the amorphous region becomes elastomeric. Therefore polymers with low T_g present good ion conducting properties at room temperature. On the other hand, too low T_g values are related with higher tendency to crystallization. In this context, phase diagrams are a valuable tool. A phase diagram of PEO-LiClO₄ is shown in Gray's book *Solid Polymer Electrolytes*. (7) For this system various phases were reported: crystalline complexes (PEO)₆:LiClO₄ and (PEO)₃:LiClO₄, crystalline pure PEO, as well as amorphous phases. (7,46)

Poly(ethylene oxide) of low molecular weight is commonly termed poly(ethylene glycol), PEG. Studies on the influence of the doping amount on ionic conductivity of PEO

and PEG have shown a maximal ion conductivity for $y = 8$ to 10 . (47-48) The presence of a maximum occurs due to the action of opposed effects. Increment of salt concentration inhibits the crystallization of the pure PEO, if the compound is completely elastomeric, larger conductivity values will be obtained. (47) Furthermore, the number of charge carriers will increase. On the other hand, too large amounts of salt will cause a reduction of available sites and benefit formation of ion pair clusters. (48) Also, the overall polarity of the samples will increase which in turn will stiffen the polymer chains, reducing their mobility. (48)

However, the mechanical stability of PEO/PEG at high temperatures ($60-80^{\circ}\text{C}$), where the largest capacities are obtained, is not sufficient to completely avoid dendrite formation. (3)

Triblock Copolymer PS-PEO-PS

Electrolytes with high mechanical stability can stop dendrite growth in Li metal batteries. On the other hand, highest ionic conductivity is present in soft polymers, such as PEO. Several studies have been done, aiming to combine polymers with high shear modulus with polymers with good ion conducting properties, through the synthesis of block copolymers. The group of Balsara (4,13) presented a strategy to obtain copolymers in which mechanical and electrical properties are decoupled. The most common architectures are AB diblock and ABA triblock copolymers, where A is the block responsible for mechanical stability and B is the block responsible for ion conductivity. (11) In polystyrene-poly(ethylene oxide) (PS-PEO) diblock copolymers the mechanical properties will be governed by the aliphatic PS block, while the PS block should have no influence on the electrical properties of the PEO block. The polymer Polystyrene (PS), despite having a low cost, presents good mechanical properties with a T_g of approximately 100°C , thus above the temperature of operation. Since PS has no polar heteroatom in its structure it cannot dissolve the lithium salts in its structure. Most of this copolymers present a lamellar morphology. (4,13,16)

The normalized conductivity $\sigma_n(T)$ for block copolymers directly indicates the conductivity efficiency of the PEO block as compared to a PEO homopolymer at the same temperature and is given by:

$$\sigma_n(T) = \frac{\sigma(T)}{f \phi_{PEO} \sigma_{PEO}(T)} \quad (1)$$

where $\sigma(T)$ is the measured conductivity, f a morphology related factor (in case of randomly orientated lamellae $f = 2/3$), ϕ_{PEO} the volume fraction of the PEO block in the copolymer and

$\sigma_{PEO}(T)$ the conductivity of the homopolymer. Thus, $\sigma_n(T) = 1$ represents the theoretical limit at which PEO in the block copolymer presents the same conducting properties as the PEO homopolymer. While the conductivity increases with temperature, the normalized conductivity is not affected, indicating that both homopolymer and block copolymer have the same temperature dependency. (13)

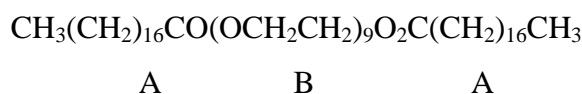
Since the ion transport in PEO was related to segmental motions of the polymer chains, the conductivity is expected to be independent of M_{PEO} over a high molecular weight limit. While for the homopolymer this limit is already reached at about 3 kg/mol, (49) for the block copolymer conductivity continues increasing up to at least 60 kg/mol (4) (for LiTFSI and $y = 12$). Furthermore, for lower doping ratios, the normalized conductivities are considerably lower than the theoretical limit, $\sigma_n(T) = 1$, for molecular weights up to 100 kg/mol. (13) As possible explanations for this drastic difference, two different approaches were proposed: First, at the PS-PEO interface the dielectric constant of PEO is lower, which could reduce the degree of dissociation of the salts in this region. (14) And second, block copolymers stretch when they form ordered phases, thus the Li^+ ions are tighter coordinated to PEO chains in low molecular weight copolymers than in stretched PEO of high molecular weight copolymers, leaving to increasing conductivity with molecular weight. (16)

Structural and morphological studies of the triblock copolymer PS-PEO-PS without salt showed that the relative amount of the different blocks, at a constant PEO molecular weight of 10 kg/mol, is of crucial importance. (16) The amount of PS will affect the PEO block, in the sense that large amounts will inhibit crystallization of PEO. This could be related to the previous mentioned stretching of the PEO, which limits the capacity of folding of the chains. On the other side, if PEO is the dominant block, the PS block will present larger mobility, which will even become close to that of PEO itself. (16)

Triblock Copolymer Poly(Ethylene Glycol) Distearate (PEGD)

Poly(ethylene glycol-400) distearate (PEGD) is a triblock copolymer of the type ABA. The blocks A are aliphatic hydrocarbon branches and block B is poly(ethylene glycol). Only the central block is capable of dissolving alkali metal salts, due to the presence of the oxygen atoms in its chemical structure. The PEGD molecule presents phase segregation between the apolar crystalline phase and the polar quasi liquid PEG phase. (50) The PEGD used in this

work has low molecular weight ($M_{\text{PEGD}} = 946$ g/mol with $M_{\text{PEG}} = 400$ g/mol), being the chemical formula:



Through dissolution of LiClO_4 , an ion conducting polymer is obtained. Ionic conductivity and thermal properties strongly depend on the amount of salt. (51) An increment in the salt concentration will increase the glass transition temperature T_g of the mobile phase (from $T_g = -68^\circ\text{C}$ for pure PEGD to $T_g = -20^\circ\text{C}$ for $y = 5$). On the other hand, the melting point T_m of the stearate phase remains constant ($T_m \approx 35^\circ\text{C}$). (52) The ion conductivity in the melt phase presents a maximum at a doping amount of $y = 9$. (51)

PEGD exhibits an interesting phenomenon, frequently found in block copolymers and polymer liquid crystals, the NMR spectra of highly doped PEGD show a sharp ^7Li quadrupolar pattern at temperatures above the polymer melting point. This is attributed to the presence of order in the polymer matrix, which in turn is responsible for anisotropic dynamics of the ions. However, orientation is only observed in the presence of a magnetic field of a few Tesla and with addition of appropriate amounts of salt. (53) This orientation is maintained up to an order-disorder transition temperature T_{OD} , which depends on the doping ratio. For the strongly doped sample with $y = 5$, $T_{\text{OD}} \approx 80^\circ\text{C}$, while for the sample with less LiClO_4 , $y = 9$, $T_{\text{OD}} \approx 46^\circ\text{C}$. (53) At temperatures around the melting point two phases coexist, thus the obtained ^7Li spectra showed two overlapping quadrupole powder pattern. (52) Through annealing of the sample above T_{OD} in the presence of an external magnetic field and subsequent cooling, it is possible to ensure that the sample is completely in the ordered state (53).

2.2 Nuclear Magnetic Resonance

2.2.1 Basic Principles of NMR Spectroscopy

The Nuclear Spin

The nuclear magnetic resonance spectroscopy, shortly NMR-spectroscopy, is a technique that studies the physical behavior of nuclei under the influence of an external magnetic field.

Nuclei can possess a spin \hat{I} . From spin results, as an intrinsic property, an angular momentum \hat{J} and a magnetic moment $\hat{\mu}$. (19) The spin, angular momentum and magnetic moment operators are related according to

$$\hat{\mu} = \gamma \hat{J} = \gamma \hbar \hat{I} \quad (2)$$

being γ the gyromagnetic ratio, a nucleus specific constant. For a single spin, a consistent set of spin operators, \hat{I}^2 , \hat{I}_x , \hat{I}_y and \hat{I}_z , determine all properties. They are related according to:

$$\hat{I}^2 = \hat{I}_x^2 + \hat{I}_y^2 + \hat{I}_z^2 \quad (3)$$

where \hat{I}^2 commutes with \hat{I}_z . Their eigenfunctions, $|l, m\rangle$, and eigenvalues, l and m , respectively, are:

$$\hat{I}^2 |l, m\rangle = l(l+1) |l, m\rangle \quad (4)$$

$$\hat{I}_z |l, m\rangle = m |l, m\rangle \quad (5)$$

where the quantum number m may be any of the $2l+1$ values $l, l-1, \dots, -l$, and l is either an integer or a half-integer. The eigenfunctions $|l, m\rangle$ are spherical harmonics. (54) Note that the factor \hbar is included as part of the operator as is convenient and common in the NMR literature. (42)

In presence of an external magnetic field $\vec{B}_0 = (0, 0, B_0)$, the Zeeman interaction usually dominates the behavior of the nuclear spin system. The Zeeman Hamiltonian is given by:

$$\hat{H} = -\gamma B_0 \hat{I}_z. \quad (6)$$

The eigenvalues of the Hamiltonian obtained from the eigenfunctions $|l, m\rangle$ are the Energies $E_{l,m}$ of the different possible states of the spin. Thus, according to:

$$\hat{H} |l, m\rangle = E_{l,m} |l, m\rangle, \quad (7)$$

the allowed energies are:

$$E_{l,m} = -\gamma B_0 m. \quad (8)$$

Furthermore, the selection rule of NMR states (55):

$$\Delta m = \pm 1. \quad (9)$$

Therefore, the energy difference ΔE between two states is given by γB_0 . This transition energy corresponds to the Larmor frequency (ω_0 or ω_L). The population difference between the energy levels corresponds to a magnetization on the z-axis and at equilibrium it is described by the Boltzmann distribution. This difference in energy and population is the basis of NMR. The population, p_m , of each eigenstate, $|m\rangle$, is: (19)

$$p_m = \frac{e^{-E_m/kT}}{\sum_{m'} e^{-E_{m'}/kT}}. \quad (10)$$

The Density Matrix

It is convenient to describe an ensemble of spin systems through the density matrix $\hat{\rho}$. Each spin system is in one of the possible eigenstates, ψ , with a probability p_ψ . Analogously, each spin system in the whole ensemble may be considered to be in the same superposition state, Ψ :

$$\Psi = \sum_{\psi} \sqrt{p_{\psi}} \psi. \quad (11)$$

Furthermore, the states of any spin system can be written as a sum over a basis set of functions $|m\rangle$ (for instance the eigenfunctions of the spin operators represent an appropriate basis set):

$$\psi = \sum_m c_m |m\rangle. \quad (12)$$

The expectation value of an operator \hat{Q} is:

$$\langle \hat{Q} \rangle = \sum_{\psi} p_{\psi} \sum_{m,m'} c_{\psi m}^* c_{\psi m'} \langle m | \hat{Q} | m' \rangle. \quad (13)$$

Alternatively, it can be written as:

$$\langle \hat{Q} \rangle = Tr \left\{ \sum_{\psi} p_{\psi} |\psi\rangle \langle \psi| \mathbf{Q} \right\}, \quad (14)$$

where \mathbf{Q} is the matrix representation of $\sum_{m,m'} \langle m | \hat{Q} | m' \rangle$. The spin density operator $\hat{\rho}$ is defined

as: (19)

$$\hat{\rho} = \sum_{\psi} p_{\psi} |\psi\rangle\langle\psi|. \quad (15)$$

Leaving to following expression for the expectation value:

$$\langle\hat{Q}\rangle = Tr\{\hat{\rho}Q\}. \quad (16)$$

The matrix representation of the density matrix presents some interesting properties. The diagonal elements $\hat{\rho}_{mm}$ (equation (17)) are the populations of the states $|m\rangle$ while the off-diagonal elements $\hat{\rho}_{mm'}$ (equation(18)) are the coherences between states $|m\rangle$ and $|m'\rangle$. (54)

$$\hat{\rho}_{mm} = \sum_{\psi} p_{\psi} c_{\psi m}^* c_{\psi m} = \overline{c_{\psi m}^* c_{\psi m}} \quad (17)$$

$$\hat{\rho}_{mm'} = \sum_{\psi} p_{\psi} c_{\psi m}^* c_{\psi m'} = \overline{c_{\psi m}^* c_{\psi m'}}. \quad (18)$$

The overbar indicates the average over all spin systems. At thermal equilibrium the coherences between the states are zero, while the populations satisfy the Boltzmann distribution as given above. (54) The equilibrium spin density matrix is:

$$\hat{\rho}_{eq} = \frac{e^{\frac{\gamma B_0 \hat{I}_z}{kT}}}{Tr(e^{\frac{\gamma B_0 \hat{I}_z}{kT}})}. \quad (19)$$

Under consideration of the high temperature approximation, which is valid for temperatures above 1 K, (42) the density matrix can be simplified to:

$$\hat{\rho}_{eq} \approx \frac{1}{2} \left(\hat{1} + \frac{\gamma B_0}{kT} \hat{I}_z \right). \quad (20)$$

It is useful to classify the coherences of the density matrix by their coherence order. In the Zeeman basis the order $q_{mm'}$ of the coherence $\rho_{mm'}$ is defined as: (54)

$$q_{mm'} = m - m'. \quad (21)$$

Where m and m' are the eigenvalues of \hat{I}_z of their respective eigenfunctions, according to equation (5). The maximal coherence order q_{max} in a spinsystem of n spins I is defined as: $q_{max} = 2In$.

Time Evolution of the Density Matrix

While the spin density operator describes the state of the ensemble of spin systems, any interaction that changes this state is described by a Hamiltonian. The effects caused on the spin density operator are given by the von Neumann (or Liouville-von Neumann) equation: (42)

$$\frac{d}{dt} \hat{\rho} = -i [\hat{H}, \hat{\rho}]. \quad (22)$$

The formal solution of the von Neumann equation for a time-independent Hamiltonian is given by:

$$\hat{\rho}(t) = e^{-i\hat{H}t} \hat{\rho}(0) e^{i\hat{H}t}. \quad (23)$$

To analyze the effects of the propagators $e^{\pm i\hat{H}t}$ on the density matrix it is possible to use the Baker-Campbell-Hausdorff Equation:

$$\hat{\rho}(t) = \hat{\rho}(0) + it[\hat{\rho}(0), \hat{H}] - \frac{t^2}{2!} [[\hat{\rho}(0), \hat{H}], \hat{H}] - \frac{it^3}{3!} [[\hat{\rho}(0), \hat{H}], \hat{H}], \hat{H}] + \dots \quad (24)$$

Evolution of the Density Matrix under the Zeeman Interaction

It is useful to analyze the free evolution of the density matrix in terms of its populations and coherences considering only the effect of the Zeeman Hamiltonian ($\hat{H} = -\gamma B_0 \hat{I}_z = \omega_L \hat{I}_z$). Therefore, first the density matrix is decomposed in terms of the coherence order q : (56)

$$\hat{\rho}(t) = \sum_q \hat{\rho}^q(t). \quad (25)$$

Subsequently, application of the Hamiltonian on the components leads to:

$$\begin{aligned} \hat{\rho}^{q_{mm'}}(t) &= e^{-i\hat{H}t} \hat{\rho}^{q_{mm'}}(0) e^{i\hat{H}t} \\ &= c_m c_m^* e^{-i\omega_L t \hat{I}_z} |m\rangle \langle m'| e^{i\omega_L t \hat{I}_z} \\ &= c_m c_m^* e^{-i\omega_L t m} e^{i\omega_L t m'} |m\rangle \langle m'| \\ &= c_m c_m^* e^{-i\omega_L t (m-m')} |m\rangle \langle m'| \\ &= e^{-i\omega_L t q_{mm'}} \rho^{q_{mm'}}. \end{aligned} \quad (26)$$

This result implies that the Zeeman Hamiltonian will not change the coherence order of any component of the density matrix. Furthermore, the populations are not affected, while the coherences will oscillate with $\cos(q\omega_L t) - i\sin(q\omega_L t)$. This represents the precession of the magnetization around the external field B_0 and in the case of single quantum coherence it is related to the complex observable NMR signal.

The Density Matrix in the Rotating Frame

It will prove useful to eliminate the effect of the Larmor rotation by transition to a frame that rotates with the same frequency: $\omega_R = \omega_L$. The rotating frame spin density operator is related to the fixed frame density operator by: (42)

$$\hat{\rho}_R(t) = e^{i\omega_R t \hat{I}_z} \hat{\rho}(t) e^{-i\omega_R t \hat{I}_z}. \quad (27)$$

The Effect of Radio-Frequency Pulses

Transition between the energy levels are induced under the action of an additional magnetic field $\vec{B}_1(t)$. (42) This time dependent field has to oscillate at a frequency close to the resonance frequency, usually in the radio-frequency (rf) range. The Hamiltonian describing the effect of both the static B_0 and the oscillating B_1 (which will be taken to oscillate along the x-axis) fields is:

$$\hat{H} = \hat{H}_0 + \hat{H}_1 = -\gamma(\hat{I}_z B_0 + 2\hat{I}_x B_1 \cos(\omega_{rf} t)). \quad (28)$$

The oscillating \vec{B}_1 field may be described as two counter rotating components. One component rotates in the same sense as the nuclear spins, while the other rotates in the opposite sense. However, in most cases this second component has no significant effect on the spin system, (19) so that equation (28) can be rewritten as:

$$\hat{H} = -\gamma(\hat{I}_z B_0 + B_1 e^{-i\omega_{rf} t \hat{I}_z} \hat{I}_x e^{i\omega_{rf} t \hat{I}_z}). \quad (29)$$

Furthermore, the Hamiltonian can be transformed into the rotating frame. In a frame rotating about B_0 at a frequency ω_{rf} the Hamiltonian becomes:

$$\hat{H}_R = -(\omega_0 - \omega_{rf}) \hat{I}_z - \gamma B_1 \hat{I}_x, \quad (30)$$

and, if the pulse is on-resonance with the spin system ($\omega_{rf} = \omega_0$):

$$\hat{H}_R = \hat{H}_{R,1} = -\gamma B_1 \hat{I}_x. \quad (31)$$

The flip angle θ caused by the pulse on the spin system is given by:

$$\theta_{rf} = \gamma B_1 \tau_{rf} = \omega_1 \tau_{rf}. \quad (32)$$

Application of pulses on a spin system allows changing the coherence order of any component of the spin density matrix, as shown in equation (33) for a pulse of arbitrary phase φ . For instance, it is possible to excite coherence from a state of thermal equilibrium by applying a pulse.

$$e^{-H_1(\varphi)t} \hat{\rho}^q(t_1) e^{H_1(\varphi)t} = \sum_{q'} \hat{\rho}^{q'}(t_2) e^{-i\Delta q \varphi}. \quad (33)$$

Each coherence component that is transferred by the pulse will gain a phase shift $\Delta q \varphi$, where Δq is the coherence order difference $\Delta q = q' - q$. (56)

Ensemble of Spin 1/2: Pauli Matrices

Consider a sample of magnetically equivalent and independent spins 1/2, which will behave as an ensemble of isolated spins 1/2. An appropriate set of spin operators for such spin systems are the Pauli matrices: (42)

$$\hat{I}_z = \frac{1}{2} \begin{pmatrix} 1 & 0 \\ 0 & -1 \end{pmatrix} \quad \hat{I}_x = \frac{1}{2} \begin{pmatrix} 0 & 1 \\ 1 & 0 \end{pmatrix} \quad \hat{I}_y = \frac{1}{2} \begin{pmatrix} 0 & -i \\ i & 0 \end{pmatrix}. \quad (34)$$

Furthermore, consider the sample was placed into an external magnetic field, B_0 , for enough time in order to reach thermal equilibrium. The spin density matrix in the rotating frame was given in equation (20). Since the unity operator $\hat{1}$ commutes with all operators and has no importance in most cases it will not be considered in the further discussion. (42) Therefore, the initial state can be written as:

$$\hat{\rho}(0) \sim \frac{1}{2} \frac{\gamma B_0}{kT} \hat{I}_z \sim \hat{I}_z. \quad (35)$$

Ensemble of Spin-1/2: A 90° Pulse and the NMR Signal

The effect caused by an rf pulse along the x-axis on the spin system can be described as follows:

$$\hat{\rho}(1) = e^{-i\hat{H}_1 \tau_{rf}} \hat{\rho}(0) e^{i\hat{H}_1 \tau_{rf}} \quad (36)$$

$$\hat{\rho}(1) = \frac{1}{\sqrt{2}} \begin{pmatrix} \cos(\frac{\omega_1 \tau_{rf}}{2}) & i \sin(\frac{\omega_1 \tau_{rf}}{2}) \\ i \sin(\frac{\omega_1 \tau_{rf}}{2}) & \cos(\frac{\omega_1 \tau_{rf}}{2}) \end{pmatrix} \frac{1}{2} \begin{pmatrix} 1 & 0 \\ 0 & -1 \end{pmatrix} \frac{1}{\sqrt{2}} \begin{pmatrix} \cos(\frac{\omega_1 \tau_{rf}}{2}) & -i \sin(\frac{\omega_1 \tau_{rf}}{2}) \\ -i \sin(\frac{\omega_1 \tau_{rf}}{2}) & \cos(\frac{\omega_1 \tau_{rf}}{2}) \end{pmatrix}.$$

Thus, for a flip angle $\theta_{rf} = 90^\circ$:

$$\begin{aligned} \hat{\rho}(1) &= \frac{1}{\sqrt{2}} \begin{pmatrix} 1 & i \\ i & 1 \end{pmatrix} \frac{1}{2} \begin{pmatrix} 1 & 0 \\ 0 & -1 \end{pmatrix} \frac{1}{\sqrt{2}} \begin{pmatrix} 1 & -i \\ -i & 1 \end{pmatrix} \\ \hat{\rho}(1) &= \frac{1}{2} \begin{pmatrix} 0 & -i \\ i & 0 \end{pmatrix} = \hat{I}_y. \end{aligned} \quad (37)$$

The pulse equalized the populations of the two states and furthermore, converted the population difference into coherences. (54) Finally, after the pulse the magnetization is allowed to evolve freely under the Zeeman interaction:

$$\begin{aligned} \hat{\rho}(2) &= e^{-i\hat{H}_z t_1} \hat{\rho}(1) e^{i\hat{H}_z t_1} \\ \hat{\rho}(2) &= \frac{1}{2} \begin{pmatrix} 0 & -i \cdot e^{-i\omega_L t_1} \\ i \cdot e^{i\omega_L t_1} & 0 \end{pmatrix} = \hat{I}_y \cos(\omega_L t_1) - \hat{I}_x \sin(\omega_L t_1). \end{aligned} \quad (38)$$

Note that the solution of equation (26) was used and the coherence order here is $q_{mm} = 1$. This final expression is proportional to the quadrature-detected NMR signal, which is obtained by taking the trace $Tr(\hat{\rho} \hat{I}_-)$, with $\hat{I}_- = \hat{I}_x - i\hat{I}_y$. The NMR spectrum can be obtained by Fourier transformation of the quadrature signal. (42)

Ensemble of Spin 1/2: The Spin Echo

The spin echo is obtained by application of a 180° pulse (for instance along the x-axis) while the magnetization is in the transverse plane:

$$\begin{aligned} \hat{\rho}(3) &= e^{-i\hat{H}_1 \tau_{180}} \hat{\rho}(2) e^{i\hat{H}_1 \tau_{180}} \\ \hat{\rho}(3) &= -\hat{I}_y \cos(\omega_L t_1) - \hat{I}_x \sin(\omega_L t_1). \end{aligned} \quad (39)$$

After the pulse the magnetization evolves freely again:

$$\hat{\rho}(4) = e^{-i\hat{H}_z t_2} \hat{\rho}(3) e^{i\hat{H}_z t_2}, \quad (40)$$

and for $t_2 = t_1$ it becomes:

$$\hat{\rho}(4) = -\hat{I}_y = -\hat{\rho}(1). \quad (41)$$

The spin echo is useful for refocusing the Zeeman interaction, heteronuclear dipolar coupling and magnetic field inhomogeneities. (42) The total pulse sequence is shown graphically in Figure 2.

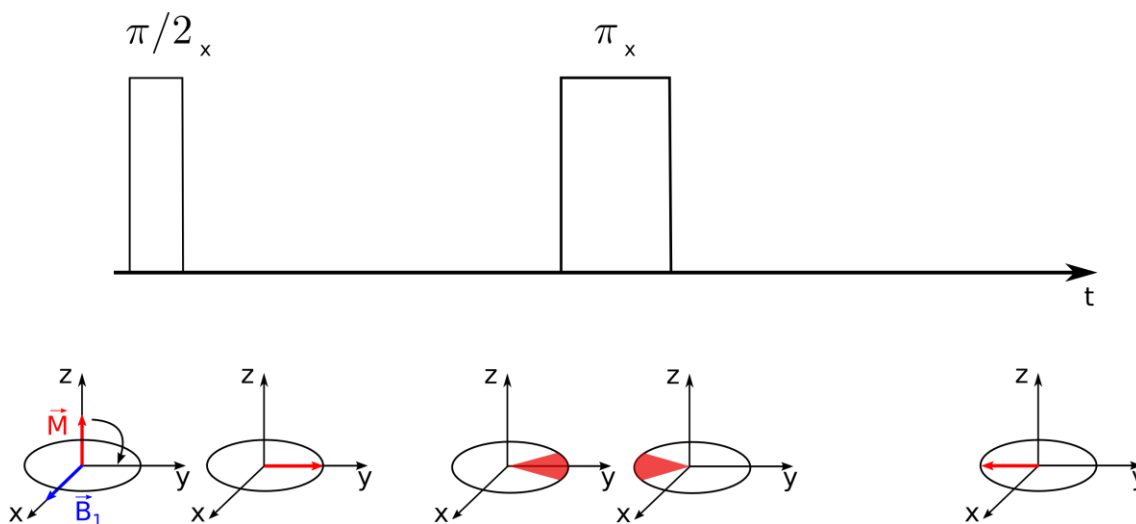


Figure 2 - Spin Echo pulse sequence.
Source: Adapted from SCHMIDT-ROHR. (42)

Nuclear Spin Interactions

Until now, the spin system was described just in terms of the Zeeman interaction; however, the Zeeman interaction contains no relevant structural information itself. Each nucleus feels magnetic and electric fields originating from the sample, which are crucial for spectroscopic applications. (57) These interactions are included in the internal spin Hamiltonian \hat{H}_{int} given as:

$$\hat{H}_{\text{int}} = \hat{H}_{\text{CS}} + \hat{H}_{\text{DD}} + \hat{H}_J + \hat{H}_Q \quad (42)$$

where \hat{H}_{CS} represents the operator of the chemical shift, which describes the interaction of the external magnetic field and the electron cloud surrounding the spins. \hat{H}_{DD} is the Hamiltonian of the direct magnetic dipole-dipole coupling, it represents the direct magnetic interaction between nuclear spins. The J-coupling is given by \hat{H}_J , it represents the indirect coupling between nuclear spins through the electrons between them. \hat{H}_Q is the Hamiltonian

of the quadrupolar coupling and represents the electric interaction of a nuclear electric quadrupole moment with the surrounding electric field gradient. (54)

The internal nuclear Spin interactions can be written in a general form as:

$$\hat{H}_{int} = \hat{\mathbf{I}} \hat{\mathbf{A}}_{loc} \hat{\mathbf{J}} \quad (43)$$

where $\hat{\mathbf{I}}$ is a nuclear spin vector, $\hat{\mathbf{J}}$ is the source of the local magnetic field at the nucleus which may be originated by either another spin, of equal or different nature, or the external magnetic field and \mathbf{A}_{loc} is a second-rank Cartesian tensor which describes the strength and orientation dependence of the local spin interaction. (19)

Irreducible Spherical Tensor Operators

Before further describing the nuclear spin interactions it will be useful to introduce the concept of spherical tensor operators. In some cases, due to some specific symmetry properties of the spherical tensor operators, this formalism has some advantages over the classical Cartesian spin operators \hat{I}_x, \hat{I}_y and \hat{I}_z . For a rank l there are $2l + 1$ different spherical tensor operators \hat{T}_{lm} with order $m = -l, -l+1, \dots, l-1, l$. A specific and useful symmetry property of the irreducible spherical tensor operators is that under rotations their rank does not change and the result of the rotation can be expressed as a linear combination of irreducible tensor operators of the same rank as the initial. (19)

In this work the irreducible tensor operator formalism was used to calculate excitation of multiple quantum coherences for ${}^7\text{Li}$, a spin 3/2 nucleus. Therefore, the necessary commutation relations of the Baker-Campbell-Hausdorff equation (shown previously, equation (24)) were based on the articles published by Bowden and Hutchison. (58-59)

The internal nuclear spin interaction in terms of the irreducible spherical tensor operators is given as:

$$\hat{H}_{int} = \hat{\mathbf{I}} \hat{\mathbf{A}}_{loc} \hat{\mathbf{J}} = \sum_{l=0}^2 \sum_{m=-l}^{+l} (-1)^m \Lambda_{l,-m} \hat{T}_{lm} \quad (44)$$

where $\Lambda_{l,-m}$ is a component of a spherical tensor and \hat{T}_{lm} of a spherical tensor operator. (19)

Chemical Shift

The presence of an external magnetic field induces electronic currents in a molecule. Those will in turn generate a local magnetic field \vec{B}_s . (42) The interaction of the local field with the nuclear spin is called the shielding interaction and it can alter the nuclear resonance frequency. This shift of the resonance frequency is called chemical shift. (19) The induced local field is linearly dependent on the applied field: (54)

$$\vec{B}_s = \sigma \vec{B}_0 \quad (45)$$

where σ is the chemical shift tensor, a 3x3 matrix. The chemical shift Hamiltonian acting on a spin is:

$$\hat{H}_{CS} = \gamma \hat{I} \sigma \vec{B}_0. \quad (46)$$

Direct Dipole-Dipole Coupling

The magnetic moments of the nuclei interact through space, this interaction is called direct dipolar coupling (in contrast to the indirect dipolar coupling which is mediated by electron clouds). The Hamiltonian of the direct dipolar interaction between two nuclear spins, i and j , is given by

$$\hat{H}_{DD} = -\frac{\mu_0}{4\pi} \hbar \gamma_i \gamma_j \frac{3(\hat{I}^i \cdot \vec{r}_{ij} / r_{ij})(\hat{I}^j \cdot \vec{r}_{ij} / r_{ij}) - \hat{I}^i \cdot \hat{I}^j}{(r_{ij})^3} \quad (47)$$

where μ_0 is the permeability of vacuum, \vec{r}_{ij} the vector between the two nuclei and $r_{ij} = |\vec{r}_{ij}|$. (42) Alternatively, it is possible to resume the dipolar interaction into a second rank Cartesian tensor D to rewrite the equation as:

$$\hat{H}_{DD} = -\hat{I}^i D \hat{I}^j \quad (48)$$

or, in terms of a spherical tensor operator (19):

$$\hat{H}_{DD} \sim \Lambda_{20} \hat{T}_{20}. \quad (49)$$

In an isotropic liquid, the secular components (components of the Hamiltonian which commute with \hat{I}_z) of the dipole-dipole coupling are essentially averaged out to zero. In solids, it usually is responsible for large linebroadenings. Nonetheless, dipolar couplings also play an important role in liquids, since the non-secular components cause relaxation. (54)

Quadrupolar Coupling

Nuclei with a spin larger than 1/2 have in addition to the magnetic dipole moment an electric quadrupole moment, which interacts with the electric field gradient generated by the electron clouds surrounding the nuclei. This will have an effect on the nuclear spin system. The quadrupole interaction Hamiltonian is given by:

$$\hat{H}_Q = \frac{eQ}{2I(2I-1)\hbar} \hat{\mathbf{I}}\mathbf{V}\hat{\mathbf{I}} \quad (50)$$

where \mathbf{V} is the electric field gradient tensor, e the elementary charge and Q the quadrupole moment. (42) Thus, eQ is constant for a given nuclear isotope. The magnitude of the quadrupolar interaction will depend strongly on the molecular environment, for instances, symmetrical ionic environments will present small local field gradients and consequently the nuclei in such an environment will have small quadrupolar couplings. (54)

The quadrupolar couplings appearing in this work, from the quadrupolar moment of the spin 3/2 nucleus ${}^7\text{Li}$, are small and therefore can be treated as perturbations of the Zeeman interaction. Furthermore, only the secular term $\hat{H}_Q^{(1)}$ will be considered, leaving to: (54)

$$\hat{H}_Q^{(1)} = \omega_Q^{(1)} \frac{1}{6} (3\hat{I}_z^2 - I(I+1)\hat{1}) \quad (51)$$

with $\omega_Q^{(1)}$, the first-order quadrupolar coupling given by:

$$\omega_Q^{(1)} = \frac{3eQV_{zz}}{2I(2I-1)\hbar}. \quad (52)$$

If the Cartesian spin operators are replaced by spherical tensor operators, the first order quadrupolar coupling Hamiltonian can be written as: (19)

$$\hat{H}_Q^{(1)} \sim V_{20}\hat{T}_{20}. \quad (53)$$

Quadrupolar nuclei have more than two angular momentum eigenstates along the z-axis, according to equation (5) for spin 3/2 there are four eigenstates. Figure 3 shows the energy levels of a spin 3/2 nucleus and the effect of the quadrupolar coupling to first order. The relative intensities of the peaks of the central and satellite transitions at $-\omega_Q/2$, 0 and $\omega_Q/2$ are 3:4:3.

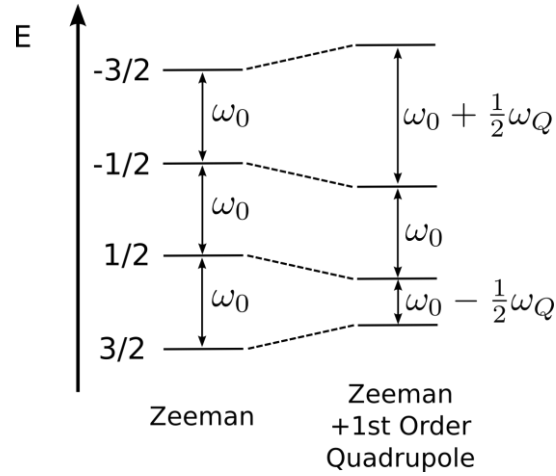


Figure 3 - Effect of the quadrupole coupling to first order on the Zeeman interaction for a spin 3/2. ω_0 is the Larmor frequency and ω_Q the quadrupole coupling.

Source: By the author.

The relevant Cartesian \hat{I}_x, \hat{I}_y and \hat{I}_z and irreducible spherical spin operators for spins 3/2 are given in their matrix representation Figure 4 and Figure 5: (60)

$$\hat{I}_z = \frac{1}{2} \begin{pmatrix} 3 & 0 & 0 & 0 \\ 0 & 1 & 0 & 0 \\ 0 & 0 & -1 & 0 \\ 0 & 0 & 0 & -3 \end{pmatrix} \quad \hat{I}_x = \frac{1}{2} \begin{pmatrix} 0 & \sqrt{3} & 0 & 0 \\ \sqrt{3} & 0 & 2 & 0 \\ 0 & 2 & 0 & \sqrt{3} \\ 0 & 0 & \sqrt{3} & 0 \end{pmatrix} \quad \hat{I}_y = \frac{1}{2i} \begin{pmatrix} 0 & \sqrt{3} & 0 & 0 \\ -\sqrt{3} & 0 & 2 & 0 \\ 0 & -2 & 0 & \sqrt{3} \\ 0 & 0 & -\sqrt{3} & 0 \end{pmatrix}$$

Figure 4 - Cartesian spin operators for a single spin 3/2.

Source: By the author.

$$\begin{aligned}
\hat{T}_{1,0} &= \frac{1}{2\sqrt{5}} \begin{pmatrix} 3 & 0 & 0 & 0 \\ 0 & 1 & 0 & 0 \\ 0 & 0 & -1 & 0 \\ 0 & 0 & 0 & -3 \end{pmatrix} & \hat{T}_{2,0} &= \frac{1}{2} \begin{pmatrix} 1 & 0 & 0 & 0 \\ 0 & -1 & 0 & 0 \\ 0 & 0 & -1 & 0 \\ 0 & 0 & 0 & 1 \end{pmatrix} & \hat{T}_{3,0} &= \frac{1}{2\sqrt{5}} \begin{pmatrix} 1 & 0 & 0 & 0 \\ 0 & -3 & 0 & 0 \\ 0 & 0 & 3 & 0 \\ 0 & 0 & 0 & -1 \end{pmatrix} \\
\hat{T}_{1,1} &= \sqrt{\frac{3}{10}} \begin{pmatrix} 0 & -1 & 0 & 0 \\ 0 & 0 & -\frac{2}{\sqrt{3}} & 0 \\ 0 & 0 & 0 & -1 \\ 0 & 0 & 0 & 0 \end{pmatrix} & \hat{T}_{2,1} &= \sqrt{\frac{1}{2}} \begin{pmatrix} 0 & -1 & 0 & 0 \\ 0 & 0 & 0 & 0 \\ 0 & 0 & 0 & 1 \\ 0 & 0 & 0 & 0 \end{pmatrix} & \hat{T}_{3,1} &= \frac{1}{\sqrt{5}} \begin{pmatrix} 0 & -1 & 0 & 0 \\ 0 & 0 & \sqrt{3} & 0 \\ 0 & 0 & 0 & -1 \\ 0 & 0 & 0 & 0 \end{pmatrix} \\
\hat{T}_{2,2} &= \sqrt{\frac{1}{2}} \begin{pmatrix} 0 & 0 & 1 & 0 \\ 0 & 0 & 0 & 1 \\ 0 & 0 & 0 & 0 \\ 0 & 0 & 0 & 0 \end{pmatrix} & \hat{T}_{3,2} &= \sqrt{\frac{1}{2}} \begin{pmatrix} 0 & 0 & 1 & 0 \\ 0 & 0 & 0 & -1 \\ 0 & 0 & 0 & 0 \\ 0 & 0 & 0 & 0 \end{pmatrix} \\
\hat{T}_{3,3} &= \begin{pmatrix} 0 & 0 & 0 & -1 \\ 0 & 0 & 0 & 0 \\ 0 & 0 & 0 & 0 \\ 0 & 0 & 0 & 0 \end{pmatrix}
\end{aligned}$$

Figure 5 - Irreducible tensor operators \hat{T}_{lm} of rank 1 and order m for a single spin 3/2.
Source: By TELLES. (60)

2.2.2 NMR Spectroscopy Experiments

Magic Angle Spinning (MAS)

Magic Angle Spinning (MAS) is a technique used in most solid state NMR experiments. In MAS experiments (Figure 6) the sample is placed in a rotor and rotated about an axis oriented at the magic angle with respect to the external magnetic field ($\theta_{magic} = 54.75^\circ$). The aim of this technique is to average out the effect of the anisotropic interactions: chemical shift anisotropies, homonuclear and heteronuclear dipolar couplings and quadrupolar couplings to first order. (19)

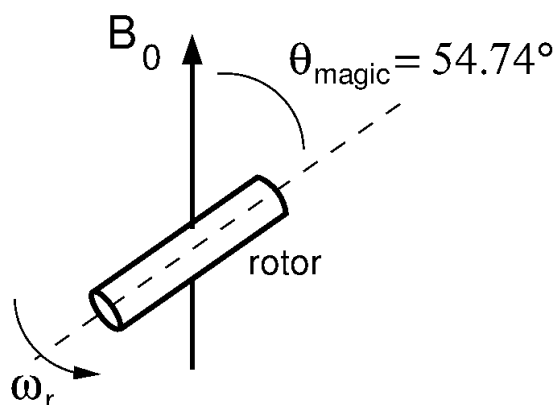


Figure 6 - Spinning of a sample around an axis oriented at the magic angle θ_{magic} with respect to the external magnetic field.

Source: By the author.

The general condition which has to be satisfied, in order to have an efficient removal of the anisotropic effects, is that the spinning frequency of the rotor is fast compared to the spectral linewidth. However, if the spinning frequency is not sufficiently large, the spectrum will present extra lines. These lines are separated by a frequency equal to the spinning frequency or integer multiples of it, called spinning sidebands.

Cross-Polarization

Cross-polarization (CP) is used to increase the signal to noise ratio and to avoid long relaxation times. (19) Cross polarization is mediated by the dipolar interaction between the ^1H and X spins. In this section a simplified theoretical explanation is given in order to clarify the important concepts. Figure 7 shows the pulse sequence of the cross-polarization experiment.

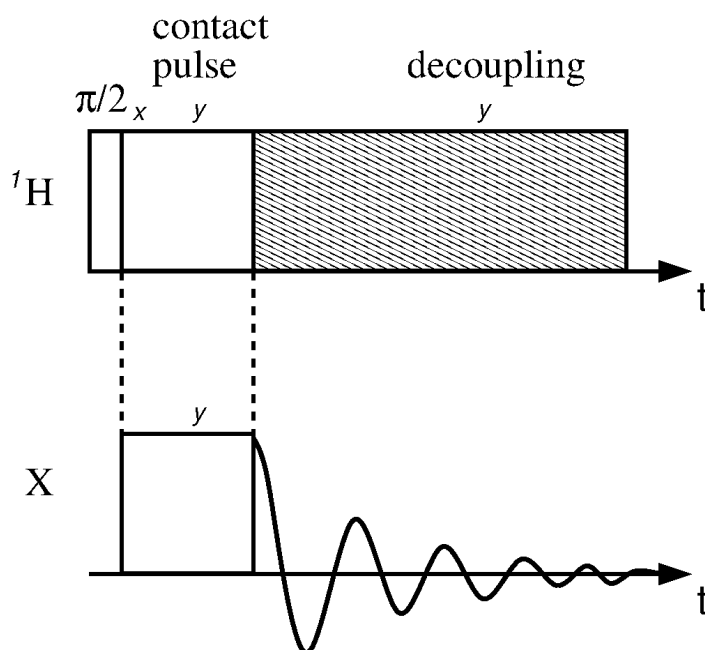


Figure 7 - Pulse sequence of the cross-polarization experiment $\text{X}\{{}^1\text{H}\}$ with heteronuclear decoupling.
Source: By the author.

First, a $\pi/2$ pulse flips the ${}^1\text{H}$ magnetization into the transverse plane. Parallel to the magnetization an on-resonance ${}^1\text{H}$ contact pulse is applied, the resulting field $B_1({}^1\text{H})$ is called spin-lock field. This field has two functions, it locks the magnetization and it acts as quantization axis for the ${}^1\text{H}$ spins. However, the weaker $B_1({}^1\text{H})$ field is not able to lock the same amount of polarization as the external magnetic field.

At the same time, an analogue $B_1(\text{X})$ spin-lock field is applied, which acts as quantization axis for the X spins. At the beginning, the two X states are equally populated. The dipolar coupling, which only contains operators acting on the z -axis, cannot affect the net energy of the spin system in the rotating frame. Thus, a transition from the energetic lower state into the energetic higher state of a ${}^1\text{H}$ spin in the rotating state is compensated by the dipolar coupling through the opposite transition of an X spin, but can only occur if the energy gap in both transitions is equal. Therefore the Hartmann-Hahn condition (equation (54)) has to be fulfilled, which experimentally implies that the spin-lock fields have to be set carefully. (19)

$$\gamma_H B_1({}^1\text{H}) = \gamma_X B_1(\text{X}). \quad (54)$$

Note that in figure Figure 7 a pulse is applied on the ${}^1\text{H}$ channel during the acquisition of the X nuclei. This high power irradiation cancels the effect of the direct and indirect

heteronuclear dipolar couplings of the ^1H spins on the X spins. This technique is called heteronuclear decoupling.

$T_{1\rho}$ Measurement

For measuring the longitudinal relaxation time in the rotating field, $T_{1\rho}$, the magnetization is locked by the \vec{B}_1 field during a time τ in the spin-lock experiment (Figure 8). (42) The magnetization along the locking field will not experience dipolar dephasing and therefore decay only due to the relaxation in the rotating time with the time constant $T_{1\rho}$. Since \vec{B}_1 is much smaller than \vec{B}_0 , $T_{1\rho}$ will be sensible to different molecular motions than T_1 , in the order of tens of kHz instead of hundreds of MHz (42).

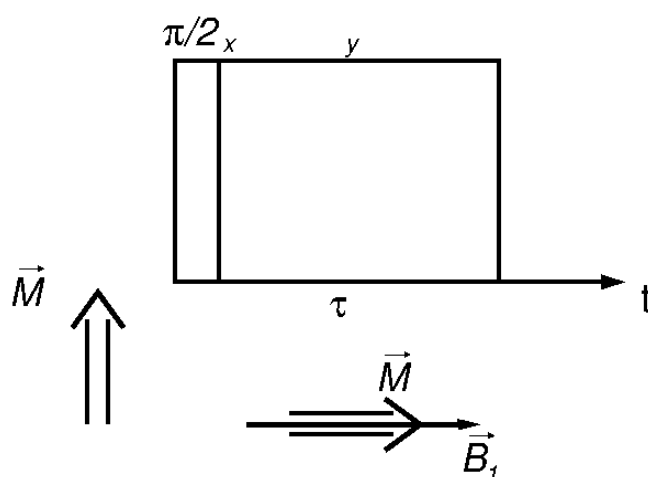


Figure 8 - Pulse sequence of the spin-lock experiment for measuring $T_{1\rho}$.
Source: Adapted from SCHMIDT-ROHR. (42)

Spin Diffusion

Spin diffusion is the diffusion of coherent magnetization without the diffusion of matter and is mediated by dipolar couplings. (19) The time dependence of the diffusion process contains information on the domain sizes and morphology in heterogeneous polymers. (42) The spin diffusion experiment allows to determine distances in a range from 0.1 to 200 nm. In Figure 9, the pulse sequence of the ^1H Goldman Shen experiment is shown (with subsequent CP and $^{13}\text{C}\{^1\text{H}\}$ detection and heteronuclear decoupling).

Suppose a heterogeneous sample with two regions of different mobility. In order to select the magnetization of one component while suppressing the other, the difference in

transverse relaxation can be used, which itself is due to dipolar couplings. (42,61) Therefore, first a $\pi/2$ pulse flips the magnetization in to the transverse plane, then the system is allowed to evolve freely until only magnetization from the mobile region remains. A second pulse stores the magnetization in the z-axis and during a time t_m , the ^1H spin diffusion occurs. Finally, the last pulse brings the magnetization back to the transverse plane for detection. The t_m dependence of the magnetization increment gives direct information of the domain sizes. (42)

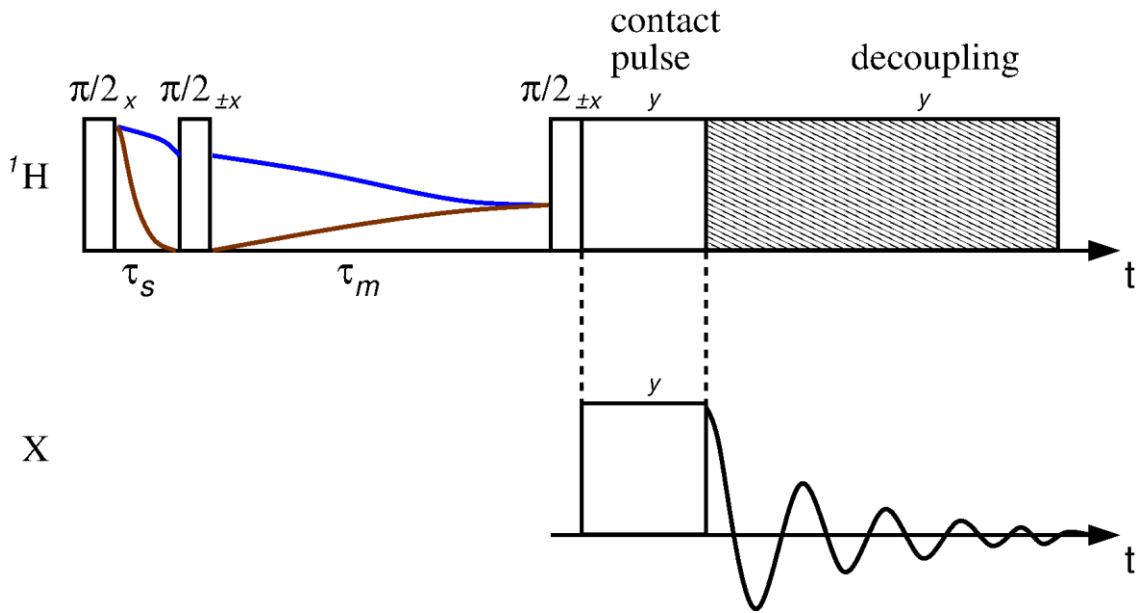


Figure 9 - Pulse sequence of the Goldman-Shen spin diffusion experiment with CP and heteronuclear decoupling.

Source: By the author.

To analyze the diffusion curves, a diffusion model considering Fick's second law is used. For a two component system it is useful to apply the initial rate approximation since it simplifies the problem by assuming an initial linear dependence of the signal intensity with $\sqrt{t_m}$. The average size of the mobile phase d_{MP} can be obtained as

$$d_{MP} = 4\varepsilon \frac{\sqrt{D_{RP}D_{MP}}}{\sqrt{D_{RP}} + \sqrt{D_{MP}}} \sqrt{\frac{t_m^{s,0}}{\pi}} \quad (55)$$

where ε is the number of orthogonal directions relevant for the diffusion process (lamellae: $\varepsilon = 1$; cylinders: $\varepsilon = 2$; spheres/cubes: $\varepsilon = 3$). (42) From the plot of the signal intensity vs. $\sqrt{t_m}$, it is possible to obtain $\sqrt{t_m^s}$ from the intersection of the extrapolation of the linear

part of the curve with the equilibrium value. Subsequently by dividing by the volumetric fraction ϕ_{RP} we obtain

$$\sqrt{t_m^{s,0}} = \frac{\sqrt{t_m^s}}{\phi_{RP}}. \quad (56)$$

D_{RP} and D_{MP} are the spin diffusion coefficients of the rigid and mobile phase respectively. In this work, for the rigid phase (PS) $D_{RP} = 0.8 \text{ nm}^2/\text{ms}$ was used, as indicated in literature, (62) while for the mobile phase (PEO) it was calculated according to

$$D_{MP} = 8.2 \cdot 10^{-6} T_2^{-1.5} + 0.007 \quad (57)$$

Finally, the inter-domain distance is determined by following relationship: (42)

$$d_I = \frac{d_{MP}}{\varepsilon \sqrt{\phi_{MP}}} = \frac{d_{MP}}{\phi_{MP}} \quad (58)$$

2.3 Relaxation in NMR

2.3.1 Theory of Relaxation

Autocorrelation Function and Spectral Density

Nuclear Spin Relaxation is an incoherent effect, and thus not reversible. Relaxation is caused by the distribution of local fields and depends on their magnitude as well as on their fluctuation rates. (42,63) This dependency was first described by Bloembergen, Purcell and Pound in the so called BPP theory. (64)

Fluctuations of the local magnetic fields may be caused, for example, by molecular reorientations. The ergodic hypothesis states that the average over an ensemble of particles is equal to the average of a single particle over time. Figure 10(a) shows a rapid and a slow randomly fluctuating function $f(t)$. The average in this model will supposed to be zero. In general, the fluctuation behavior of a randomly fluctuating function $f(t)$ can be described in terms of its autocorrelation function $G(\tau)$. Suppose a function as follows: (54)

$$G(\tau) = \langle f(t) \cdot f(t + \tau) \rangle. \quad (59)$$

Note that $G(\tau)$ is independent of t . For small values of τ , $G(\tau)$ tends to be large, while for large τ it tends to zero, as shown in Figure 10(b). Assuming an exponential behavior the curve can be described as:

$$G(\tau) = G(0)e^{-|\tau|/\tau_c}. \quad (60)$$

The spectral density $J(\omega)$ is defined as the Fourier transform of the autocorrelation function (54)

$$J(\omega) = \frac{\tau_c}{1 + \omega^2 \tau_c^2}. \quad (61)$$

In the case of fast fluctuating fields, the spectral density is broad, while for slow fluctuating fields it is sharp (Figure 10(c)). Nonetheless, the area under the curve does not depend on τ_c .

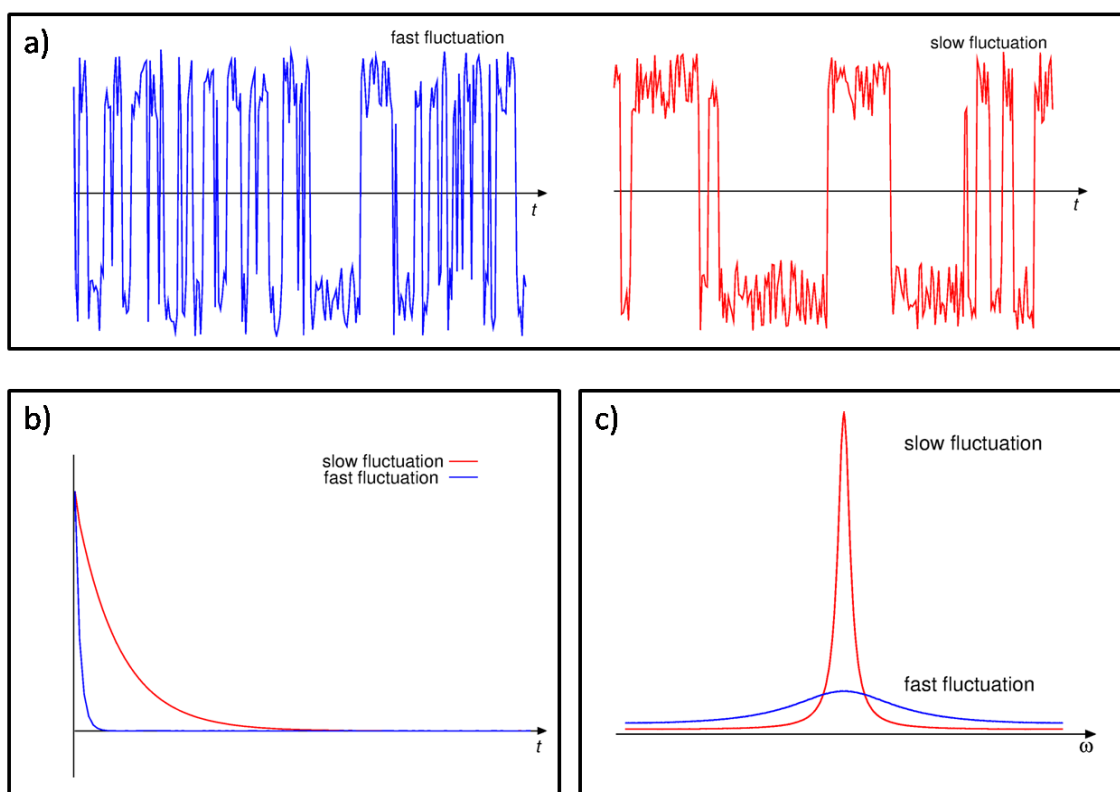


Figure 10 - Fast and slow random fluctuations between two sites (a) and their respective autocorrelation function (b) and spectral density (c).

Source: Adapted from LEVITT. (54)

Transition Probabilities

Consider a system of spin 1/2 nuclei, which in the presence of an external magnetic field will have two possible energy eigenstates $|m\rangle$, $|1/2\rangle$ and $|-1/2\rangle$, with populations p_+ and p_- respectively and $N = p_+ + p_-$. A perturbation, such as the presence of an alternating field, will induce transitions between the eigenstates. The transition probability per second

from state $|1/2\rangle$ to $|-1/2\rangle$ is denoted W_- and the reverse transition W_+ (Figure 11). Thus the evolution of the population p_+ is given by following equation: (62)

$$\frac{dp_+}{dt} = p_-W_+ - p_+W_- . \quad (62)$$

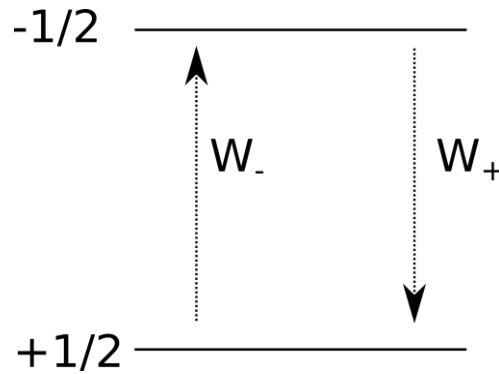


Figure 11 - Transition probabilities between two energy eigenstates of a spin 1/2 in the presence of an external magnetic field.

Source: By the author.

Time-dependent perturbation theory predicts that the transition probabilities induced by an interaction $V(t)$ between two states of different energies in one direction and in the reverse direction to be equal, (65) thus $W_+ = W_- = W$, which simplifies equation (62) to:

$$\frac{dp_+}{dt} = W(p_- - p_+) . \quad (63)$$

Let us define a variable, n , describing the population difference between both states $n = p_+ - p_-$. The kinetic equation for the population difference is obtained straightforwardly:

$$\frac{dn}{dt} = -2Wn , \quad (64)$$

whose solution is:

$$n = n(0)e^{-2Wt} . \quad (65)$$

This result implies that in the presence of an alternating field any initial population difference will cancel out with time. Furthermore, in the absence of an alternating field ($W = 0$), the populations do not change. This is fundamentally incorrect, since it is known that if a sample is placed into an external magnetic field, a difference in the populations will arise according to the Boltzmann distribution (see equation (10)) causing a net magnetization. (65)

In order to obtain a non-zero population difference at the Boltzmann equilibrium the transition probabilities must be unequal in such a way that:

$$p_- W_{\downarrow} = p_+ W_{\uparrow} \quad (66)$$

where W_{\uparrow} is the thermally corrected transition probability from state $|1/2\rangle$ to $|-1/2\rangle$ and W_{\downarrow} the inverse transition. The thermally corrected transitions can be justified by postulating a coupling between the spin system and the lattice. As a consequence, the rate transition will also depend on the probability of the lattice being in an eigenstate which allows the transition. Therefore, nuclear population will be in thermal equilibrium with the lattice. (65)

The differential equation describing the time evolution of the population difference can now be written as:

$$\frac{dn}{dt} = N(W_{\downarrow} - W_{\uparrow}) - n(W_{\downarrow} + W_{\uparrow}). \quad (67)$$

The solution of which is:

$$n = n_0(1 - e^{-t(W_{\downarrow} + W_{\uparrow})}), \quad (68)$$

where:

$$n_0 = N \frac{(W_{\downarrow} - W_{\uparrow})}{(W_{\downarrow} + W_{\uparrow})}. \quad (69)$$

Furthermore, let us define:

$$\frac{1}{T_1} = W_{\downarrow} + W_{\uparrow}. \quad (70)$$

The spin-lattice relaxation rate or longitudinal relaxation rate is the sum of the transition probabilities between the states and T_1 is a characteristic time related to the duration needed by the populations of a sample to reach thermal equilibrium. (65)

Relaxation Rates by Randomly Fluctuating Fields

Consider a spin system placed in a large static magnetic field B_0 orientated along the z-axis. Furthermore, each spin experiences a different local field $b_{loc}(t)$ which is weak compared to the static field and also fluctuates randomly in time. For simplicity the mean

square of those weak fluctuating components will be assumed to be equal in all directions (66):

$$\langle b_{loc,x}^2 \rangle = \langle b_{loc,y}^2 \rangle = \langle b_{loc,z}^2 \rangle = \langle b_{loc}^2 \rangle. \quad (71)$$

It can be shown that the transition probabilities, responsible for reaching the Boltzmann distribution at equilibrium, are given by the random field model as:

$$W_{\downarrow} + W_{\uparrow} = \frac{1}{T_1} = \gamma^2 \langle b_{loc}^2 \rangle J(\omega_0), \quad (72)$$

thus, the longitudinal relaxation rate depends on the spectral density at the Larmor frequency. Also, note that the longitudinal relaxation depends only on the contribution of local fields along the x and y direction. (57) This relaxation mechanism is non-secular, since it does change the energy of the system without altering its wavefunction. (66)

Furthermore, it is possible to analyze the effect of the local field fluctuations not only on the populations of the density matrix but also on its coherences. The characteristic time describing the relaxation of the off-diagonal terms of density matrix is the transverse relaxation time, T_2 .

$$\frac{1}{T_2} = \frac{1}{2} \gamma^2 \langle b_{loc}^2 \rangle J(0) + \frac{1}{2} \gamma^2 \langle b_{loc}^2 \rangle J(\omega_0) = \frac{1}{2} \gamma^2 \langle b_{loc}^2 \rangle J(0) + \frac{1}{2} \frac{1}{T_1}. \quad (73)$$

According to equation (72), two different contributions affect the transverse relaxation time. A non-secular component, depending on $J(\omega_0)$, but also a secular component, caused by the fluctuation of the local fields along the z-axis, which depends on the spectral density at zero frequency. (66)

Different relaxation mechanisms can be responsible for the local magnetic fields, such as dipolar coupling, chemical shift anisotropy or quadrupolar coupling. The expressions of the T_1 and T_2 relaxation times are different for each relaxation mechanism. (57)

In summary, the BPP theory shows that the relaxation rates (T_1^{-1} and T_2^{-1}) are essentially proportional to the spectral density and depend on the principal interaction causing relaxation. In Figure 12 typical T_1 and T_2 curves are shown. Note that T_1 passes through a minimum in contrast to T_2 . Viscosity increases from left to right.

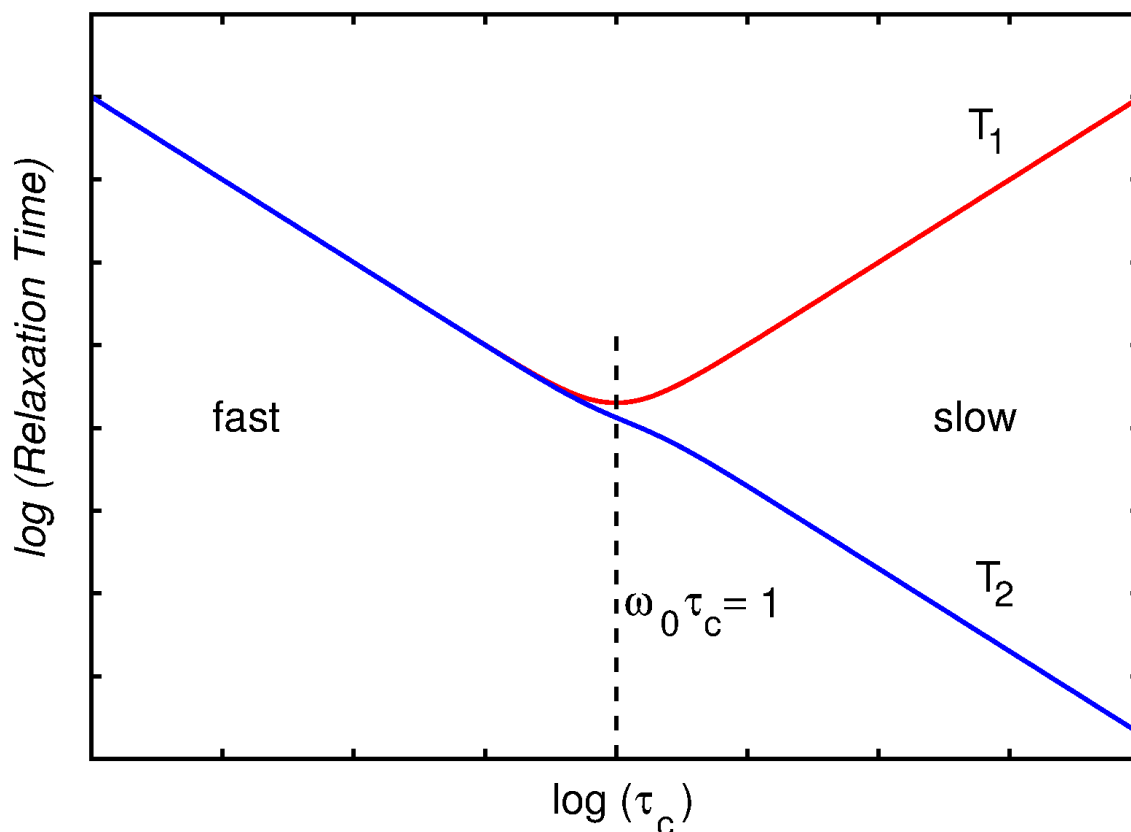


Figure 12: T_1 and T_2 relaxation time dependence on the correlation time according to the BPP theory.
Source: By the author.

Relaxation Mechanisms

Until now, relaxation was treated in terms of isolated spins placed in randomly fluctuating fields. In this section, the influence of the internal spin interactions (see section 2.2.1) on the relaxation behavior will be presented. ^7Li relaxation in ion conducting polymers is caused by two mechanisms, quadrupolar and dipolar couplings. Dipolar relaxation, both homo- and heteronuclear, is caused by the random fluctuations of the through-space dipolar couplings of the spins. Quadrupolar relaxation is caused by the interaction of the nuclear quadrupole moment with the fluctuating electric field gradients at the nucleus. It is important to note, that even if the secular part of the interactions are averaged to zero, the non-secular parts will still be important for the processes of relaxation. (54)

The dipolar interactions cannot be treated as a source of randomly fluctuating fields but have to be analyzed in terms of the four energy levels obtained from the interaction between two spins. (67) The transition probabilities and relaxation rates are given by the

Solomon equations. (54) From these equations, the T_1 and T_2 relaxation times for the homonuclear dipolar coupling in terms of the spectral density functions are given by:

$$\frac{1}{T_1} = \frac{3}{10} b^2 (J(\omega_0) + 4J(2\omega_0)) \quad (74)$$

and

$$\frac{1}{T_2} = \frac{3}{20} b^2 (3J(0) + 5J(\omega_0) + 2J(2\omega_0)). \quad (75)$$

Where b , the dipolar coupling constant, depends on the distance r between the spins:

$$b = -\frac{\mu_0}{4\pi} \frac{\hbar\gamma^2}{r}. \quad (76)$$

Note that in contrast to the treatment of the random fluctuating fields, the relaxation times also depend on the spectral density function at twice the Larmor frequency $J(2\omega_0)$.

The relaxation times for the case in which the quadrupolar relaxation mechanism is predominant are given by: (68)

$$\frac{1}{T_1} = 2a_c (J(\omega_0) + 4J(2\omega_0)) \quad (77)$$

and

$$\frac{1}{T_2} = a_c (3J(0) + 5J(\omega_0) + 2J(2\omega_0)). \quad (78)$$

With a_c :

$$a_c = -\frac{3}{400} \left(\frac{eQV_{zz}}{\hbar} \right)^2 \left(1 + \frac{\eta^2}{3} \right) \frac{2I+3}{I^2(2I-1)}. \quad (79)$$

Where eQ is the nuclear quadrupole moment, V_{zz} the anisotropy of the electric field gradient tensor and η the quadrupolar asymmetry parameter.

The Bloch Equations

The equation of motion of the magnetization in an external magnetic field is given by:

$$\frac{d}{dt} \vec{M} = \gamma \vec{M} \times \vec{B} \quad (80)$$

with $\vec{B} = (0,0,B_0)$. Including the phenomenological description of the longitudinal and transverse relaxation to this equation leads to the Bloch equations: (69)

$$\frac{d}{dt} \vec{M} = \gamma \vec{M} \times \vec{B} - \frac{(M_z(t) - M_z^0)}{T_1} \vec{z} - \frac{(M_x(t)\vec{x} + M_y(t)\vec{y})}{T_2}, \quad (81)$$

where M_z^0 is the magnetization along z at the equilibrium. The formal solution of this equation in the rotating frame and on resonance ($\omega_0 = 0$) are given by: (63)

$$M_z(t) = M_z^0 - (M_z^0 - M_z(0)) e^{-\frac{t}{T_1}} \quad (82)$$

and

$$M_{x,y}(t) = e^{-\frac{t}{T_2}} M_{x,y}(0). \quad (83)$$

Chemical Exchange and the Bloch-McConnell Equations

NMR provides a powerful tool for studying exchange of a nucleus between environments, in which it presents different NMR parameters. Chemical exchange can occur due to chemical reactions or conformational transitions, inter- or intramolecularly. (70) Any exchange involves the passing of a kinetic barrier, and thus, require a certain activation Energy E_A . The reaction rate constant, k , follows an Arrhenius-law: (21)

$$k = A e^{-E_A/RT} \quad (84)$$

where A is a pre-exponential factor and R is the gas constant.

Consider a system with two sites with magnetization M_a and M_b , at dynamical equilibrium and with exchange rates k_{ab} and k_{ba} :



If the two sites have different populations at equilibrium, k_{ab} and k_{ba} will be different according to:

$$\frac{k_{ab}}{k_{ba}} = \frac{M_0^b}{M_0^a}. \quad (86)$$

The time evolution of the magnetization considering both relaxation and exchange, is given by the Bloch-McConnell equations: (71):

$$\frac{d}{dt} \vec{M}_z(t) = [\mathbf{K} - \mathbf{R}_1] [\vec{M}_z(t) - \vec{M}_0] \quad (87)$$

$$\frac{d}{dt} \vec{M}_{x,y}(t) = [\mathbf{K} - \mathbf{R}_2] \vec{M}_{x,y}(t), \quad (88)$$

where

$$\vec{M}_z = \begin{bmatrix} M_z^a \\ M_z^b \end{bmatrix}, \quad \vec{M}_{x,y} = \begin{bmatrix} M_{x,y}^a \\ M_{x,y}^b \end{bmatrix} \quad \text{and} \quad \vec{M}_0 = \begin{bmatrix} M_0^a \\ M_0^b \end{bmatrix} \quad (89)$$

and

$$\mathbf{K} = \begin{bmatrix} -k_{ab} & k_{ba} \\ k_{ab} & -k_{ba} \end{bmatrix} \quad \text{and} \quad \mathbf{R}_{1,2} = \begin{bmatrix} \frac{1}{T_{1,2}^a} & 0 \\ 0 & \frac{1}{T_{1,2}^b} \end{bmatrix}. \quad (90)$$

Furthermore, defining: (54)

$$\mathbf{L}_{1,2} = [\mathbf{K} - \mathbf{R}_{1,2}] = \begin{bmatrix} -\frac{1}{T_{1,2}^a} - k_{ab} & k_{ba} \\ k_{ab} & -\frac{1}{T_{1,2}^b} - k_{ba} \end{bmatrix} \quad (91)$$

the solutions of the differential equations (87) and (88) can be written as:

$$\vec{M}_z(t) = \vec{M}_0 - e^{(L_1 t)} [\vec{M}_0 - \vec{M}_z(0)] \quad (92)$$

and

$$\vec{M}_{x,y}(t) = e^{(L_2 t)} \vec{M}_{x,y}(0). \quad (93)$$

Note that the Larmor frequencies of both sites were considered to be equal and on-resonance with the rotating frame. In order to calculate the exponential of a matrix it is useful to diagonalize it first:

$$e^{(L_{1,2} t)} = \mathbf{U}_{1,2} \begin{pmatrix} e^{-\lambda_{1,2}^+ t} & 0 \\ 0 & e^{-\lambda_{1,2}^- t} \end{pmatrix} \mathbf{U}_{1,2}^{-1}, \quad (94)$$

where $\lambda_{1,2}^n$ are the eigenvalues of $\mathbf{L}_{1,2}$ and the corresponding eigenvectors are the columns of the matrix $\mathbf{U}_{1,2}$. (32)

2.3.2 NMR Relaxometry Experiments

Inversion Recovery

The Inversion Recovery (IR) experiment is commonly used to obtain longitudinal relaxation times T_1 . The experiment (Figure 13) consists of a π pulse, which inverts the population of the magnetization, followed by a variable delay, τ , during which the magnetization tends to relax back to the thermal equilibrium with the characteristic time T_1 . Finally, a $\pi/2$ pulse flips the magnetization to the transversal plane for acquisition. The evolution of the longitudinal magnetization in the IR experiment, as a function of τ , can be obtained directly from equation (82) and is:

$$\vec{M}_z(\tau) = \vec{M}_0(1 - 2e^{-(\tau/T_1)}). \quad (95)$$

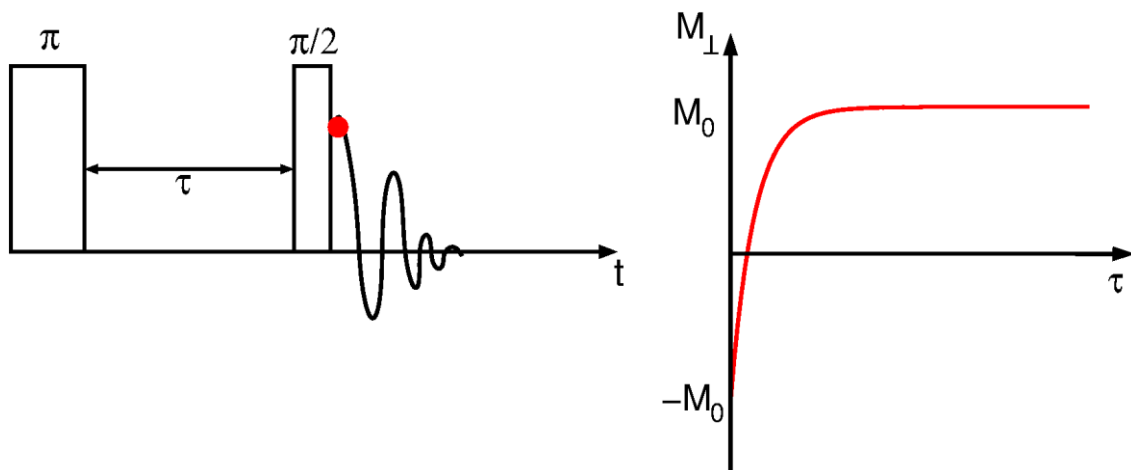


Figure 13 - Pulse sequence of the Inversion Recovery experiment (left) and evolution of the measured magnetization as a function of τ , the time between the pulses (right).

Source: By the author.

CPMG

The Carr-Purcell-Meiboom-Gill (22-23) experiment is used to obtain T_2 relaxation times. By acquiring the signal echoes, relaxation effects caused by interactions of inhomogeneous origins are refocused. (72) The application of an echo train presents two advantages as compared to acquiring a Spin-Echo with increasing echo times. First, a considerable time saving, since the entire decay is measured in a single experiment and

second, diminution of the error caused by diffusion. (22) The pulse sequence of the CPMG experiment is shown in Figure 14. The decay of the magnetization is described by equation

$$(83) (\vec{M}_{\perp}(t) = e^{-\frac{t}{T_2}} \vec{M}_{\perp}(0)).$$

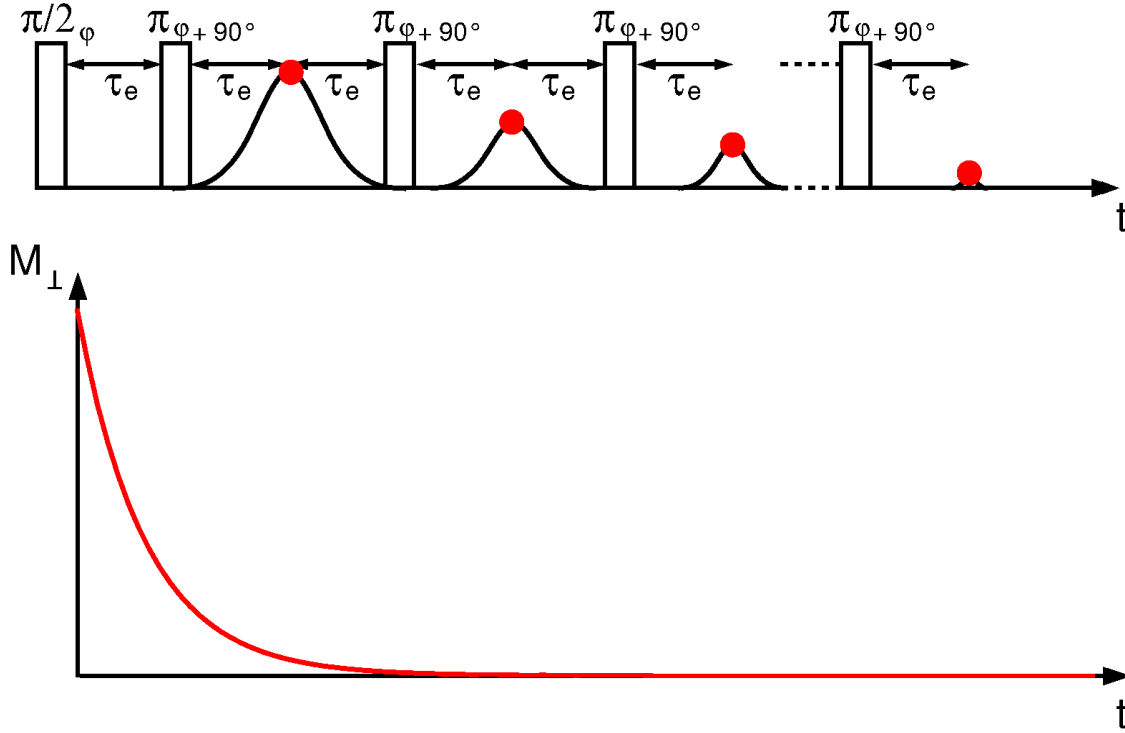


Figure 14 - Pulse sequence of the CPMG experiment and evolution of the measured magnetization as a function of t . Acquisition occurs at the top of the echoes, represented by the red dots.

Source: By the author.

$T_1 \times T_2$ Correlation

$T_1 \times T_2$ maps allow correlating longitudinal and transverse relaxation times. (73) Therefore, a CPMG echo train is concatenated to an inversion recovery pulse sequence (Figure 15). A proper description of the magnetization can be obtained by combining equations (82) and (83), and will depend on both τ_1 and τ_e .

$$\vec{M}_{\perp}(\tau_1, t) = e^{(L_2 t)} (\vec{M}_0 - 2\vec{M}_0 e^{(L_1 \tau_1)}). \quad (96)$$

In this equation, the exchange rates were not disregarded as it was done in the description of the Inversion Recovery and the CPMG experiments. The reason for this, is that in this work the relaxation parameters obtained from this experiment were used as starting parameters for the fittings of the exchange curves. In order to obtain accurate exchange rates it is important

to consider that in case of fast exchange rates the obtained decays may not be purely from relaxation, but also have components due to the exchange processes.

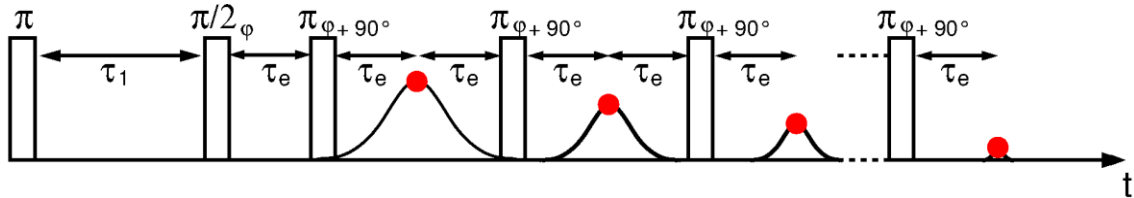


Figure 15 - Pulse sequence of the $T_1 \times T_2$ correlation experiment. Acquisition occurs at the top of the echoes, represented by the red dots.

Source: By the author.

$T_2 \times T_2$ Exchange

$T_2 \times T_2$ exchange NMR experiments are commonly used in the field of porous media, (24,27–31) but have also been used in a large variety of areas, like biological tissue (32-33) or proton exchange membranes. (34) Exchange (in this work, ion/molecule migration among different polymer sites) occurs mainly during the mixing time, τ_m , between two encoding sequences (CPMGs), while only the echoes of the second CPMG are acquired. (24–26) During τ_m the magnetization is stored in the longitudinal direction, to avoid further transverse relaxation. The 2D pulse sequence is shown in Figure 16. By doing a 2D inverse Laplace transformation (ILT) of the measured dataset, 2D exchange maps are obtained. In those maps, nuclei that remain in the same environment appear as diagonal peaks, while those who migrate to another environment will appear outside the diagonal. For sufficiently short τ_m , only signal on the diagonal is obtained, for increasing τ_m (if exchange occurs in the system in the given timescale) off-diagonal peaks will appear. The evolution of the diagonal and off-diagonal peaks depends on the exchange rate and correlation time of the ongoing exchange process. (26) The magnetization of the $T_2 \times T_2$ 2D exchange experiment is:

$$\vec{M}_{\perp}(t_1, \tau_m, t_2) = 2 e^{(L_2 t_2)} e^{(L_1 \tau_m)} e^{(L_2 t_1)} \vec{M}_0. \quad (97)$$

The factor 2 appears due to the phase cycling, which requires two steps in order to correct for the T_1 relaxation during the mixing time. (32) A general solution to equation (97) is presented in the literature, (25,28) however it is of difficult algebraic interpretation due to the large number of terms appearing in the expression.

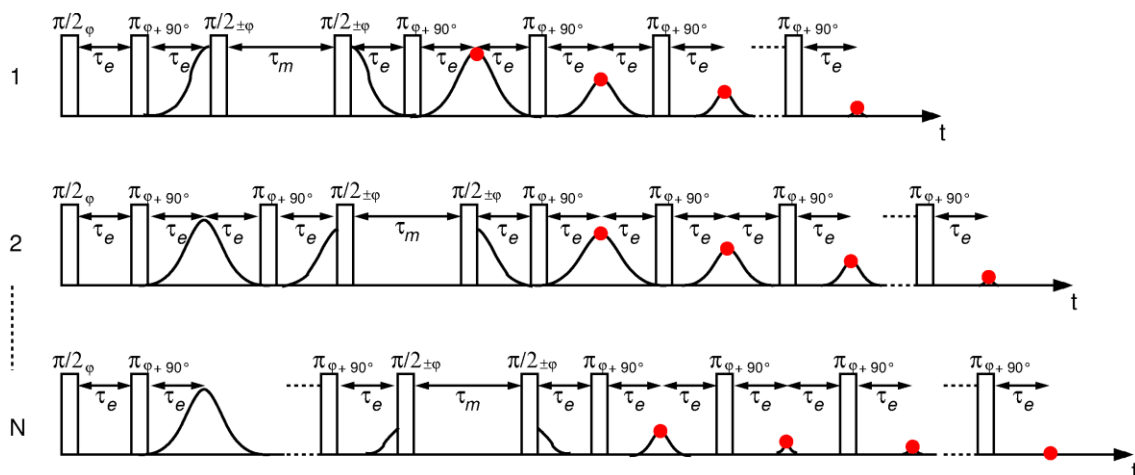


Figure 16 - 2D $T_2 \times T_2$ exchange pulse sequence. Two CPMGs are separated by a mixing time τ_m . Acquisition occurs at the top of the echoes, represented by the red dots.

Source: By the author.

Since this 2D experiment is very time-consuming, some 1D variants of the $T_2 \times T_2$ exchange experiment were proposed. (26-27) A filter applied previous to the mixing time will suppress the magnetization coming from one of the motional distinct sites. This filter can exploit either differences in the transverse (Figure 17) or in the longitudinal (Figure 18) relaxation times of the present sites. By increasing τ_m , the suppressed signal will reappear, as exchange occurs. Exchange rates and correlation times can be obtained from the mixing time dependency of the signals.

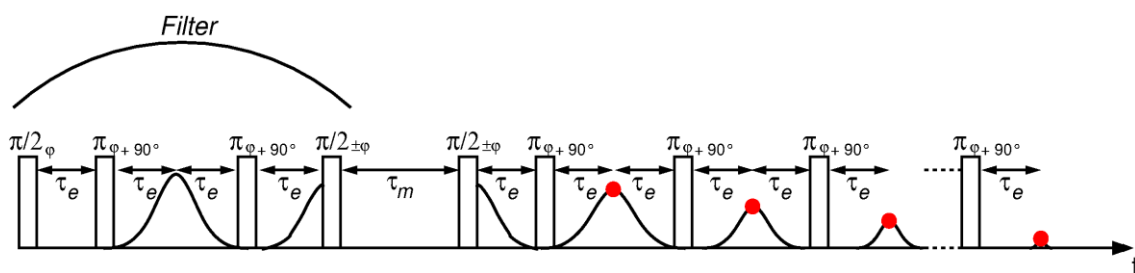


Figure 17 - 1D $T_2 \times T_2$ exchange experiment with T_2 filter. The first part of the pulse sequence, before τ_m , acts as a filter. Acquisition occurs at the top of the echoes, represented by the red dots.

Source: By the author.

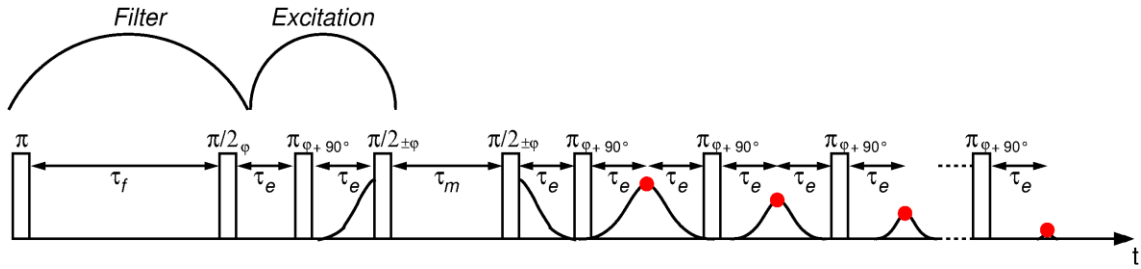


Figure 18 - 1D $T_2 \times T_2$ exchange experiment with T_1 filter. The first part of the pulse sequence, before τ_m , acts as a filter. Acquisition occurs at the top of the echoes, represented by the red dots.

Source: By the author.

The magnetization equation for the 1D variants can be obtained straightforwardly (26,32), and are given for the T_2 and T_1 filter respectively:

$$\vec{M}_{\perp}(t_f, \tau_m, t_2) = 2e^{(L_2 t_2)} e^{(L_1 \tau_m)} e^{(L_2 t_f)} \vec{M}_0 \quad (98)$$

$$\vec{M}_{\perp}(\tau_f, t_1, \tau_m, t_2) = 2e^{(L_2 t_2)} e^{(L_1 \tau_m)} e^{(L_2 t_1)} (\vec{M}_0 - 2\vec{M}_0 e^{(L_1 \tau_1)}). \quad (99)$$

2.4 Translational Diffusion

2.4.1 Self-Diffusion in NMR

Molecular diffusion is the phenomenon of material transport by atomic motion. It can be differentiated between interdiffusion and self-diffusion. Interdiffusion refers to changes in concentration over time between two regions of different concentrations, while self-diffusion refers to molecular motion in a region without concentration gradients. Essentially, self-diffusion is a random translational motion driven by the thermal agitation of the molecules. (74)

The definition of the diffusion coefficient, D , is given by Fick's first law of diffusion, which states that D is the proportionality constant relating the particle flux and the gradient of the particle concentration, c :

$$\vec{J} = -D\nabla c. \quad (100)$$

In order to analyze how the concentration changes with time due to the diffusion, it is possible to derive from Fick's first law, Fick's second law: (74)

$$\frac{dc}{dt} = D\nabla^2 c. \quad (101)$$

The effects of diffusion on the macroscopic nuclear magnetization are described by the Bloch-Torrey equation: (63)

$$\frac{d}{dt} \vec{M} = \gamma \vec{M} \times \vec{B} - \frac{(M_z(t) - M_z^0)}{T_1} \vec{z} - \frac{(M_x(t) \vec{x} + M_y(t) \vec{y})}{T_2} + D \nabla^2 \vec{M}. \quad (102)$$

In NMR, it is possible to create a well defined and known spatially dependent magnetic field gradient, \vec{g} . This gradient turns it possible to label the nuclei in the sample spatially. This is necessary to quantify the effect of the diffusion on the magnetization, since without a magnetic field gradient and supposing an ideal external magnetic field without any inhomogeneity, diffusion would not affect the magnetization.

The effect of the magnetic field gradient on the Larmor frequency of the nuclei will depend on their position inside the sample, such that: (74)

$$\omega_{eff}(p, \vec{r}) = q(\gamma B_0 + \gamma(\vec{g}, \vec{r})) = q(\omega_0 + \gamma(\vec{g}, \vec{r})). \quad (103)$$

Note that in this equation the effect of quantum coherence order q on the Larmor frequency was considered (see chapter 2.2.1 Basic Principles of NMR Spectroscopy) and the gradient was set parallel to the static magnetic field B_0 along the z -axis.

2.4.2 NMR Diffusion Measurements

Stejskal and Tanner Spin Echo (PFG-SE)

The use of pulse field gradients (PFG) in NMR experiments permits measuring translational diffusion coefficients of the involved nuclei in a straightforwardly way. The Stejskal and Tanner Spin Echo pulse sequence, (75) shown in Figure 19, is a modification of the simple Spin Echo pulse sequence. After a $\pi/2$ pulse flips the magnetization to the transversal plane, a gradient pulse of duration δ and magnitude g is applied. Therefore, after a time τ , the nuclear spin will have experienced a phase shift whose magnitude will depend on their respective position. The magnetization has been spatially coded.

After a time τ past the first rf pulse, a π pulse inverts the sign of the precession and subsequently another gradient pulse of equal duration and magnitude is applied. If no diffusion occurs during the experiment, the second gradient will reverse the effects of the first gradient and the relative intensity of the echo will only depend on the T_2 relaxation coefficient. On the other hand, if the spins have moved, the second gradient will not

completely refocus the spin phases and the echo intensity will be attenuated. The degree of attenuation will increase with larger gradient intensity.

The transverse magnetization at the echo maximum ($t = 2\tau$) will depend on the times δ , Δ , and τ , as well as on the gradient intensity g according to the Stejskal-Tanner equation (equation (104)). Diffusion coefficients can be obtained by analyzing the decay of the magnetization as a function of the gradient intensity:

$$M(g) = M_0 e^{-\frac{2\tau}{T_2}} e^{-D\gamma^2 g^2 \delta^2 (\Delta - \frac{\delta}{3})} \quad (104)$$

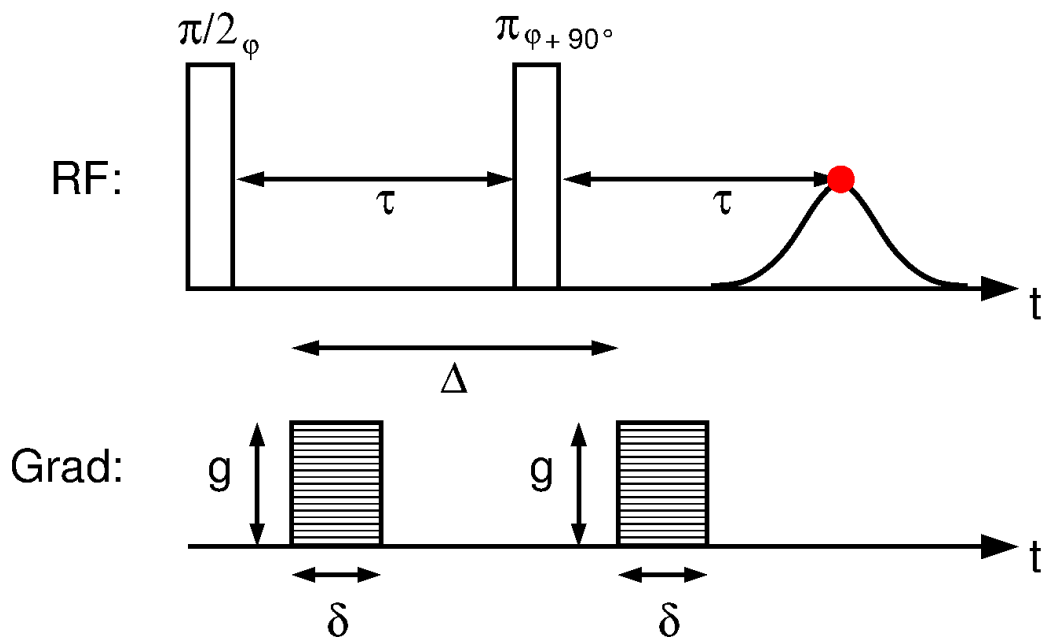


Figure 19 - Pulse sequence of the Stejskal and Tanner pulse field gradient Spin Echo experiment. For measuring diffusion coefficients, the experiment is repeated multiple times with varying gradient pulse intensity. Acquisition occurs at the top of the echo, represented by the red dot.

Source: By the author.

Pulse Field Gradient Stimulated Echo (PFG-STE)

In the case of a sample presenting short T_2 relaxation times and low diffusion coefficients, the attenuation obtained in the PFG-SE experiment might be insufficient. Stimulated echoes can be a solution to this problem. (76) In the Stimulated Echo pulse sequence, the magnetization is stored in the longitudinal direction during the time Δ (Figure 20). Therefore, the relaxation during the time τ_m will depend on T_1 instead of T_2 . The decay of the echo magnetization at $t = \tau_m + 2\tau$ is given by:

$$M(g) = \frac{M_0}{2} e^{-\frac{2\tau}{T_2} - \frac{\tau_m}{T_1}} e^{-D\gamma^2 g^2 \delta^2 (\Delta - \frac{\delta}{3})}. \quad (105)$$

Note the factor 1/2 which is intrinsic to the Stimulated Echo as compared to the simple echo. Therefore, in order to the PFG-STE be an advantage as compared to the PFG-SE sequence, the longitudinal relaxation time has to be considerably larger than the transverse relaxation time.

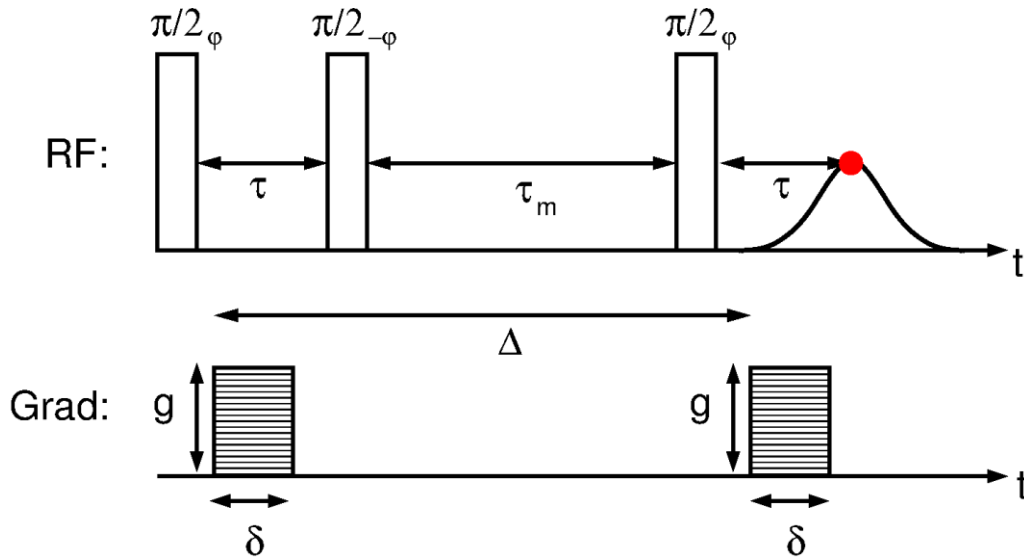


Figure 20 - Pulse sequence of the Stejskal and Tanner pulse field gradient stimulated echo experiment. For measuring diffusion coefficients, the experiment is repeated multiple times with varying gradient pulse intensity. The magnetization is stored in the longitudinal direction. Acquisition occurs at the top of the echo, represented by the red dot.

Source: By the author.

Multiple Quantum Pulsed Gradient Spin Echo (MQPGSE)

Another solution to the problem of low diffusion coefficients and relaxation times for elements with quadrupolar isotopes, as it is the case of ^7Li ($I=3/2$), is the use of multiple quantum ($q > 1$) techniques. (37) Since the precession frequency of higher coherence order will be q times faster than the precession of single quantum coherence ($q=1$), the higher coherences will be q times more sensitive to the magnetic field gradients, as shown in the modified Stejskal-Tanner equation. (37)

$$M(g) = M_0 e^{-Dq^2\gamma^2 g^2 \delta^2 (\Delta - \frac{\delta}{3})}. \quad (106)$$

The relaxation attenuation factor was disregarded in this equation, since the transverse relaxation of multiple quantum coherences is not straightforward. (77)

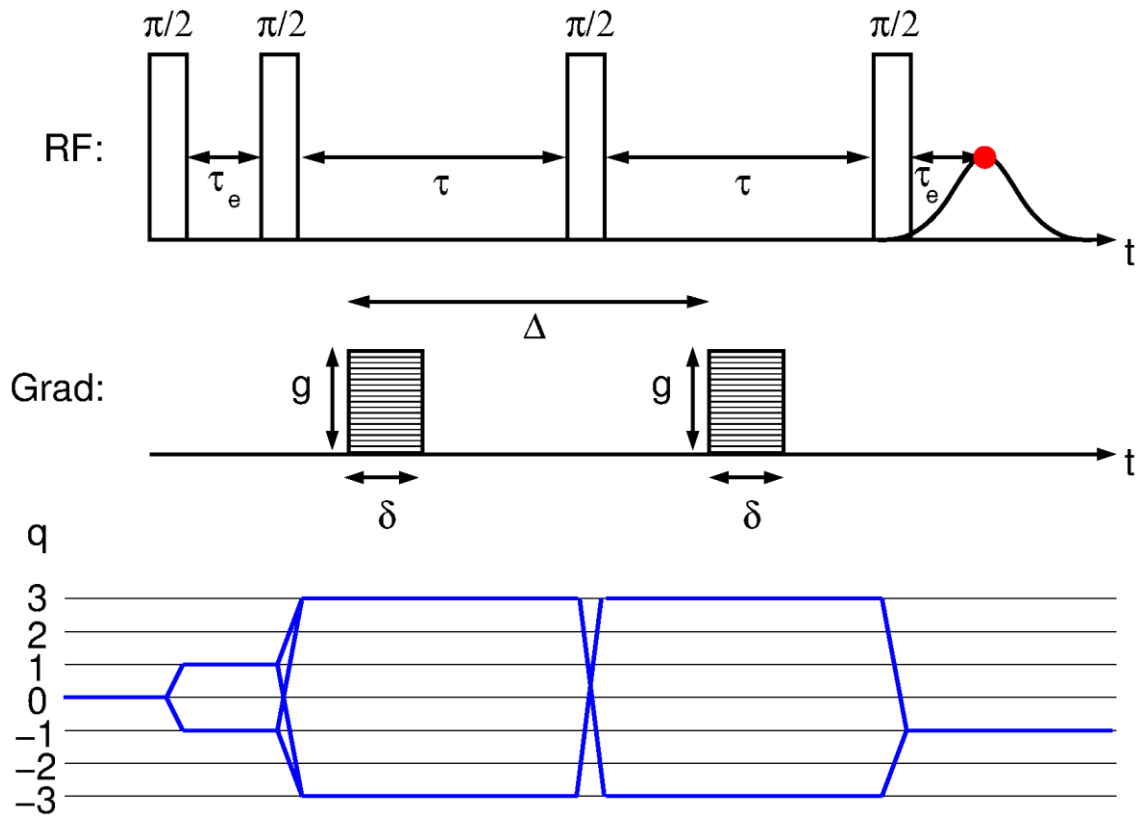


Figure 21 - Pulse sequence and coherence transfer pathway of the MQPGSE experiment for nuclei with spin $3/2$. The desired coherence transfer pathway is emphasized in blue. For measuring diffusion coefficients, the experiment is repeated multiple times with varying gradient pulse intensity. Acquisition occurs at the top of the echo, represented by the red dot.

Source: By the author.

3 Experimental

3.1 Sample Preparation

The doped polymers were obtained by direct dissolution of appropriate amounts of lithium perchlorate (LiClO_4) (Aldrich, 95%) in polyethylene glycol (PEG) (Aldrich, average M_n ca. 2000 g/mol) or poly(ethylene glycol) (400) distearate (PEGD) (Polysciences, average M_n PE block ca. 546 g/mol, average M_n PEG block ca. 400 g/mol) at 80°C for 3 hours under stirring. Afterwards, the samples were dried in a vacuum oven for 12 hours at 70°C and stored in a desiccator.

The triblock copolymers PS-PEO-PS were prepared by our collaborators from the *Aix-Marseille Université* from Prof. Gimes group using the technique of controlled radical polymerization (17,18). Afterwards the polymers were doped with the lithium salt LiTFSI (lithium bis(trifluoromethane sulfonyl) imide). The measured samples are summarized in Table 1 and Table 2, where y is the oxygen-to-lithium ratio.

$$y = [O]/[Li]$$

Table 1 - Prepared samples (denoted with an X).

Sample	$y = 5$	$y = 8$	$y = 9$	$y = 12$	$y = 15$	$y = 20$	$y = 46$	$y = 100$
PEG2000	X							
PEG400D	X							

Source: By the author.

Table 2 - Samples obtained from the group of Prof. Gígenes.

Sample	M _{PEO} (g/mol)	M _{PS} (g/mol)	T _g PEO (°C)	T _g PS (°C)	T _f (°C)	X _c (%)	PEO/PS (%)	y
BP25	35000	107700		90.53	46.1	51.36	25	
SBE25-10	35000	107700	-41.93	99.36		0	25	10
SBE25-25	35000	107700	-47.38	98.29	34.38	34.43	25	25
BP33	35000	72400	-51.68	97.46	43.81	51.36	33	
BP46	35000	38900			48.88	56.16	46	
SBE46-10	35000	38900	-44.45	92.86	20.13	0.81	46	10
SBE46-25	35000	38900	-41.71	94.32	38.05	39.55	46	25
BP69	35000	15300	-45.21		50.39	48.29	69	
SBE69-10	35000	15300	-42.17			0	69	10
SBE69-25	35000	15300	-39.43		36.46	35.74	69	25
SBE100-10	35000	0	-47.51			0	100	10
SBE100-25	35000	0	-40.74		45.67	48.69	100	25

Source: By the author.

3.2 Measurements and Data Processing

The differential scanning calorimetry (DSC) measurements were performed in the IQSC/USP in the group of Prof. Éder Tadeu Gomes Cavalheiro by Priscila Cervini Assumpção, on a DSC Q10 V9.9 Build 303 instrument. Sample weights were 12-14 mg and measurements were performed between -60°C and 300°C at a heating rate of 20 °C/min.

NMR experiments were performed partly in our laboratory in the IFSC/USP and partly in the laboratory of Prof. Klaus Schmidt-Rohr in the *Iowa State University* (ISU). In the ISU, measurements were performed at a magnetic field of 9.4 T, which is equivalent to a ¹H frequency of approximately 400 MHz, using a Bruker Avance 400 spectrometer and a Bruker double-resonance magic angle spinning probehead for 7-mm rotors. All spectra were measured at a spinning frequency of 5 kHz. The ¹H pulse length was 4.2 μs. In the Spin diffusion experiments, contact times of 1 ms, mixing times between 100 μs and 1 s and a recycling delay of 1 s with 40960 scans were used.

In the IFSC, ⁷Li measurements on doped PEG and PS-PEO-PS were done with a Tecmag Discovery spectrometer and a Varian 5-mm liquid probehead at a magnetic field of

9.4 T, which is equivalent to a ${}^7\text{Li}$ frequency of approximately 155 MHz. The sample temperature was maintained at 23 °C throughout the NMR data acquisition with exception of the variable temperature experiments. The ${}^7\text{Li}$ 90° and 180° pulse lengths were 12.25 and 24.5 μs , respectively. For the CPMGs and the FIDs 4 scans were recorded. Each 1D $T_2 \times T_2$ experiment was collected with 256 scans, while the 2D $T_2 \times T_2$ and $T_1 \times T_2$ experiments with 8 scans. The time between echoes was $t_e = 200 \mu\text{s}$ in the CPMGs and the $T_1 \times T_2$ experiments and $t_e = 400 \mu\text{s}$ in the 1D and 2D $T_2 \times T_2$ exchange experiments. Mixing times, t_m , values between 1 ms and 1.5 s were used. The recycle delay in all experiments, besides $T_1 \times T_2$ and Inversion Recovery, was 5 s.

Measurements on PEGD were also done at the IFSC, using a 2T magnet (equivalent to a ${}^7\text{Li}$ frequency of approximately 33 MHz) with a Tecmag Discovery spectrometer and a homemade probehead for 5-mm tubes with a gradient coil. The gradient amplifier for the gradient coil was a Techron 8607. MQ excitation and diffusion experiments were performed at 50°C. The pulse length of the hard ${}^7\text{Li}$ rf pulses was 11 μs . The PFGSE experiment was done with 1024 scans. The triple quantum diffusion experiment was done with 256 scans and 16 phases for the phase incremented pulse.

The T_2 distributions from one- and two-dimensional experiments were obtained through the Inverse Laplace Transform (ILT) using a software written on MATLAB. The value of α , an arbitrary weighting parameter of the ILT, used for the presented result was 10 for the 1D and 0.1 for the 2D experiments.

4 Results and Discussion

The results of this work are divided in three sections. The first (section 4.1), focuses on the polymer PEG doped with different amounts of the LiClO_4 salt. This system was chosen as a model ion conducting polymer due to its relative simple chemical structure. Nevertheless, knowledge on the nature of the different coexisting phases was necessary and thus analyzed through DSC (section 4.1.1). This allowed us to apply sophisticated NMR relaxometry techniques and evaluate them on their reliability as a tool for studying ion conducting systems (section 0).

In a second part, after validating the pertinent relaxometry techniques, we aim to apply them to a material of higher complexity, doped triblock copolymers based on polyethylene oxide (high molecular weight PS-PEO-PS) (section 4.2). But before making this step it was estimated necessary to gain knowledge about morphological and structural properties of these samples, therefore high-resolution solid-state NMR techniques were applied (section 4.2.1). Finally, ion dynamics inside the triblock copolymers were studied with the previously analyzed relaxometry techniques (section 4.2.2).

In the third section (section 4.3), we study the dynamics of the ions in solid polymer electrolytes through diffusion measurements instead of relaxometry. The Multiple Quantum Pulse Gradient Spin Echo (MQPGSE) experiment is a promising tool for obtaining diffusion coefficients, even if those are relatively slow. This technique was applied on the lithium-salt doped PEGD triblock copolymer (section 4.3.4). Therefore, it was necessary to first obtain theoretical and experimental knowledge on MQ excitation and detection (sections 4.3.1, 4.3.2 and 4.3.3).

4.1 PEG/ LiClO_4

4.1.1 DSC

Differential scanning calorimetry (DSC) measurements of PEG were performed on a temperature range previously evaluated by TGA (Thermogravimetric Analysis). In Figure 22 the obtained curves are presented in a temperature range from -50 to 250°C . Pure PEG2000 ($M_n = 2000$ g/mol) presents a large endothermic peak at 53°C indicating melting of the

crystalline phase. The amount of pure PEG crystalline phase was calculated using a perfect heat of fusion of 203 J/g for PEO, (78) leaving to a crystallinity of 89%. The percentages of pure crystalline PEG in the doped samples were calculated from the relative intensities of the endothermic peaks and are listed together with their melting temperatures in Table 3. A clear glass transition at low temperatures is observed for the doped samples. For the pure sample and for the lowest doping ratio however, no glass transitions were identified, probably due to low intensity or for being outside the measured range. Glass transition temperature T_g increases with increasing salt amount as expected (Table 3).

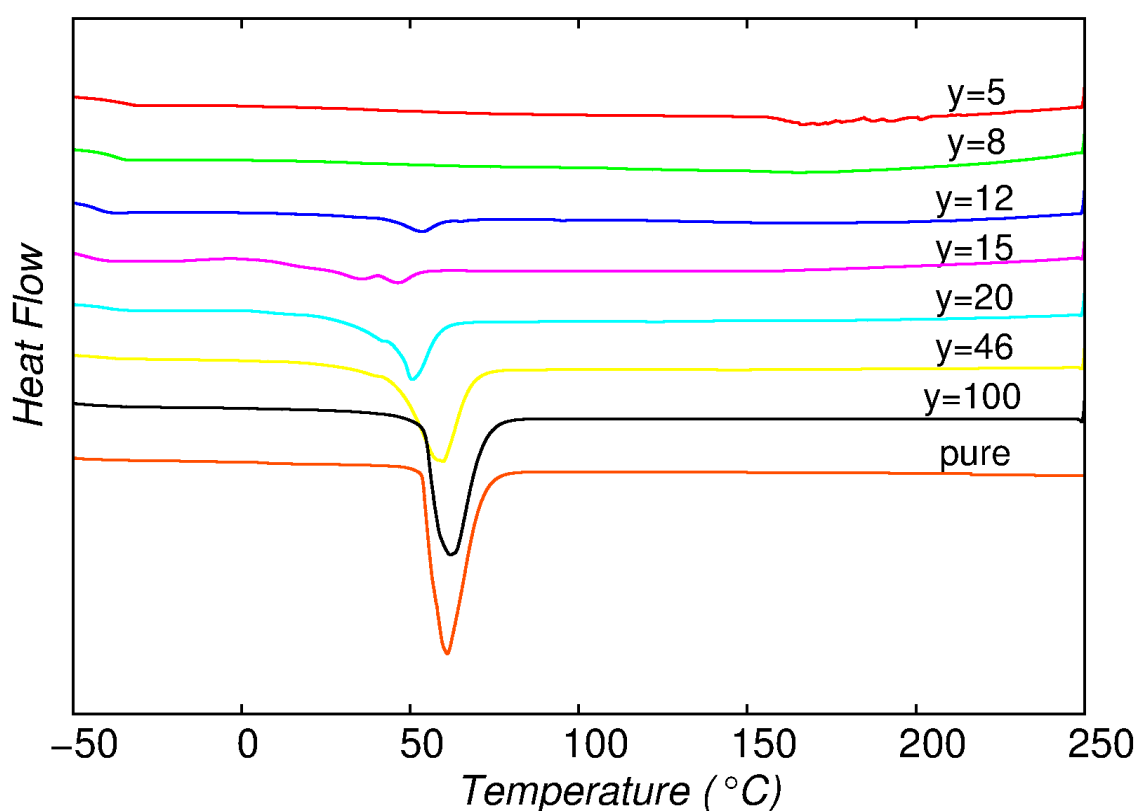


Figure 22: DSC of PEG2000 doped with varying lithium ion concentrations y .
Source: By the author.

Furthermore, with the presence of salt no new crystalline phases appear. Crystalline PEO/LiClO₄ complexes are expected to present melting points at higher temperatures than pure PEO, between 150 and 200°C. (5,46-47) The absence of any complex crystalline phase was attributed to the very low crystallization kinetics of this system. (48,79) Consequently, the Li⁺ ions are exclusively in an amorphous phase. This offers a good chance to study dynamical behavior of the involved ions, which are of special interest due to the fact that, ionic conductivity in these systems is mainly attributed to the amorphous phase.

Table 3 - Melting temperature, crystallinity percentage and glass transition temperature of doped and pure PEG2000 obtained from DSC measurements.

y	5	8	12	15	20	46	100	pure
T _m (°C) (pure PEG)	X	X	48	39	38	50	53	53
X _c (%) (pure PEG)	0	0	7	15	42	69	82	89
T _g (°C)	-34	-36	-41	-43	-51	-50	X	X

Source: By the author.

4.1.2 Relaxation

The spectra, obtained from the FIDs, and the T₂ distributions, obtained from the CPMGs, are shown in Figure 23 and Figure 24, respectively. Quadrupolar coupling was observed only for the samples with very low amounts of salt (y = 46 and y = 100). The absence of quadrupolar coupling in the highly doped samples was attributed to fast translational motion of the lithium ions. (80) On the other hand, poorly doped samples have larger crystallinity, which could cause larger anisotropies and explain the presence of a quadrupolar pattern. The spectra were deconvoluted with two components, one with a Lorentzian lineshape attributed to more mobile lithium ions and another with a Gaussian lineshape attributed to more rigid ions. The central transition of the samples y = 46 and y = 100 was fitted only with a Lorentzian. The relative ratios and the T₂ relaxation times calculated by taking $(FWHM * \pi)^{-1}$ (Full Width at Half Maximum) are listed in Table 4.

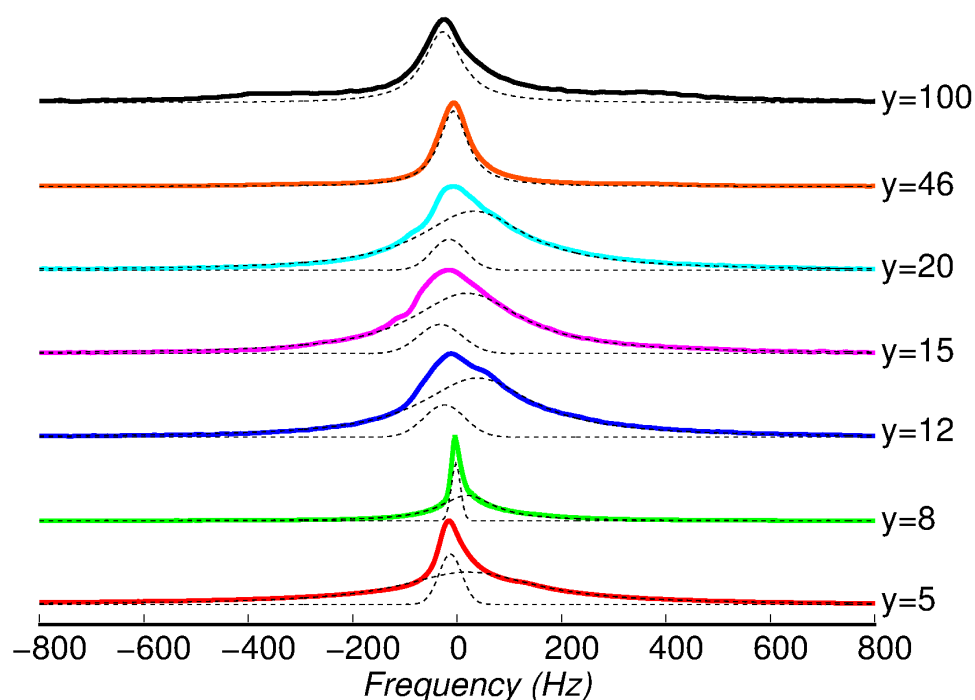


Figure 23 - ${}^7\text{Li}$ normalized spectra for PEG2000 with varying lithium ion concentrations y , deconvolution shown with dotted curves.

Source: By the author.

The ${}^7\text{Li}$ T_2 relaxation time distributions were obtained from the ILT of the exponential decays measured with the CPMG experiment. All samples presented two peaks, indicating the presence of two different lithium ions types of different dynamics. The origin of these two components is not completely clear, but it has been attributed to the presence of isolated ion-pairs. (48) Thus, the shorter relaxation times were attributed to the isolated ion-pairs, which have lower mobility, and the longer to the completely solvated ions, which have higher mobility and are the main responsible for the ion conduction. Alternatively, the presence of two different lithium species may be attributed to different binding mechanisms of the lithium ions and the polymer matrix. It should be noted that independent of the doping level, a constant higher amount of Li^+ ions has lower mobility. The ratios, obtained by fitting the data with log-Gaussian functions, were approximately 80:20 from the spectra and 70:30 from the CPMGs. Otherwise, both experiments present good consistency.

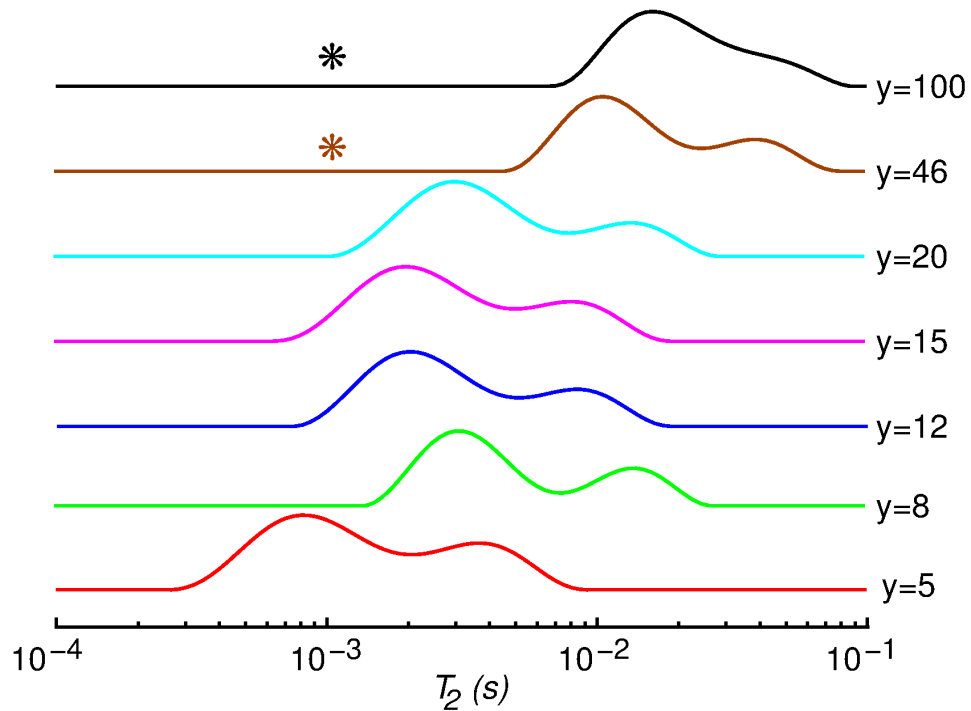


Figure 24 - ${}^7\text{Li}$ T_2 distributions obtained via ILT from the CPMG experiment for PEG2000 with varying lithium ion concentrations y . The stars indicate the estimated relaxation times of the components with quadrupolar interaction.

Source: By the author.

The $T_1 \times T_2$ maps, shown for the sample with $y = 8$ in Figure 25, showed that the lithium T_2 and T_1 relaxation times are inverted, that is, the component with shorter T_2 relaxation times has longer T_1 relaxation times and vice versa. This indicates we are on the right side of the curve shown in Figure 12 and thus in a regime of high viscosity. Note that the differences in T_1 are smaller than in T_2 . Thus, short T_2 and large T_1 were attributed to lithium ions of low mobility. The relaxation times obtained from the $T_1 \times T_2$ maps are summarized in Table 4.

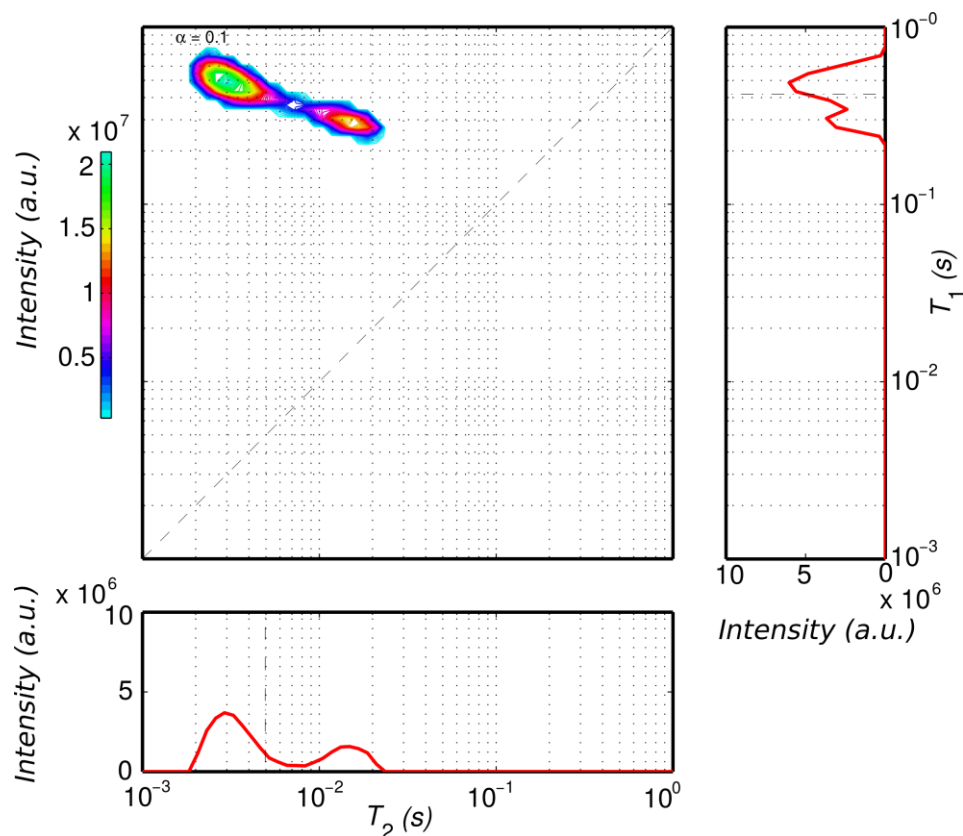


Figure 25: ${}^7\text{Li}$ $T_1 \times T_2$ 2D map of the sample PEG2000 ($y = 8$) at room temperature.
Source: By the author.

It is interesting to look at possible trends of the relaxation times. The dependency on the doping amounts is plotted in Figure 26. T_1 and T_2 behave opposite confirming that we are in a regime of high viscosity. Increment of the salt amount reduces the mobility of both lithium types. This could be explained by the increment of the polarity caused by the enhanced number of ions. As a consequence of the higher polarity, the bindings of the polymeric chains in the complex phases are stronger and thus, the mobility of the ions reduced. This stands in contrast to the behavior of the reduction of the pure PEG crystalline phase. Thus, the influence on the Li^+ mobility of the doping ratio is larger than that of the presence of a crystalline phase. Note that the sample with a doping ratio $y = 8$ is an exception to the outlined trend, presenting higher mobility as expected. This is of special interest since largest conductivity was found for $y = 8$ to 10. (47-48)

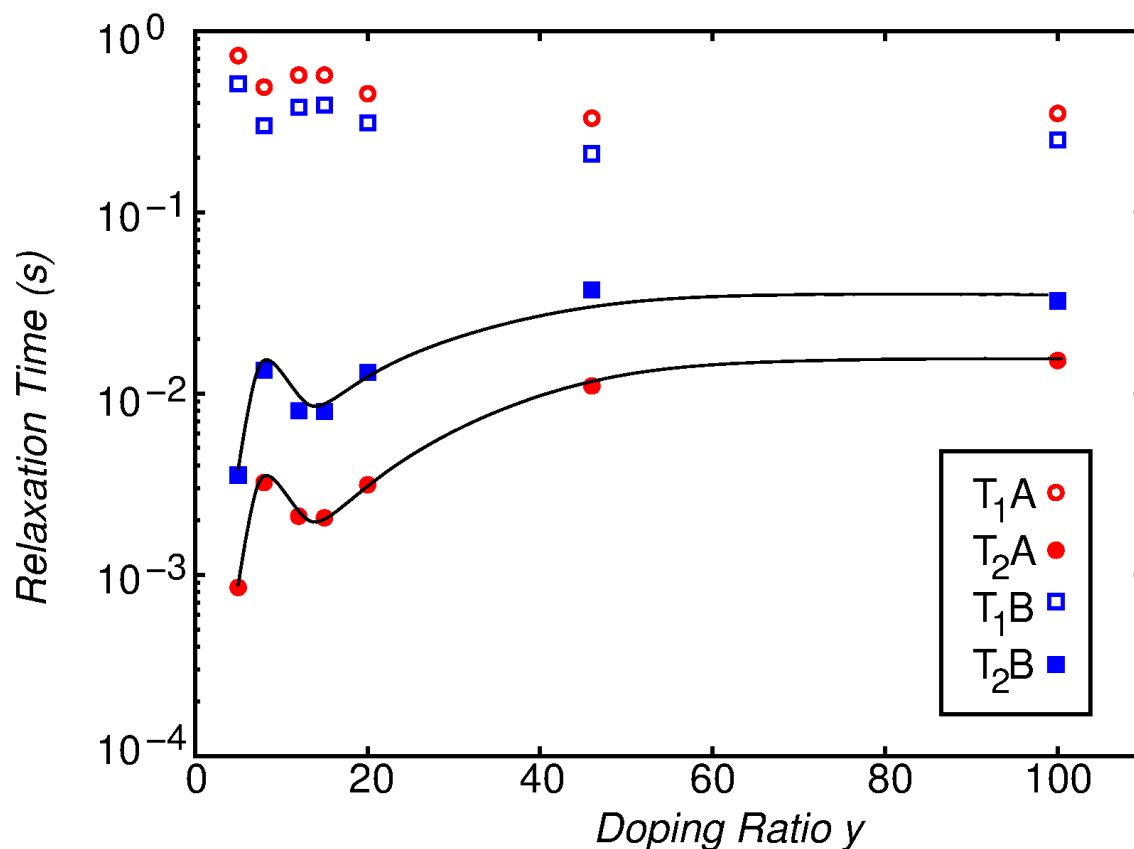


Figure 26 - T_1 and T_2 dependency on the doping ratio y of PEG2000. Trends emphasized by manually drawn line. A and B are the short and long T_2 times respectively.

Source: By the author.

Table 4 - ^7Li T_1 and T_2 relaxation time distribution obtained from the FID and $T_1 \times T_2$ experiments for PEG2000.

Sample PEG 2000	FID				$T_1 \times T_2$					
	rigid		mobile		T_2 (ms)	rigid		mobile		
	T_2 (ms)	Area (%)	T_2 (ms)	Area (%)		T_1 (s)	Area (%)	T_2 (ms)	T_1 (s)	Area (%)
$y = 5$	0.93	85	5.7	15	0.85	0.73	65	3.6	0.51	35
$y = 8$	2.5	80	15	20	3.2	0.49	70	13	0.30	30
$y = 12$	0.85	70	2.1	30	2.1	0.57	70	8.0	0.38	30
$y = 15$	1.2	88	3.2	11	2.1	0.57	70	7.9	0.39	30
$y = 20$	1.1	81	3.1	19	3.1	0.45	74	13	0.31	26
$y = 46$	x	x	x	x	11	0.33	72	37	0.21	28
$y = 100$	x	x	x	x	15	0.35	57	32	0.25	43

Source: By the author.

The temperature dependency of the ${}^7\text{Li}$ relaxation times is shown in Figure 27 for PEG2000 ($y = 8$). Heating up the sample increases the mobility and thus the T_2 relaxation times are shifted to longer times while the difference between both peaks is reduced. Note that for temperatures up to 65°C T_1 and T_2 behave inverse, confirming again the fact that we are on the left side of Figure 12, as pointed out previously. Figure 28 shows the temperature dependency of the samples with doping ratios $y = 8$ and $y = 20$. According to the DSC results (Figure 22), melting of the pure PEG phase in the sample with a doping ratio of $y = 20$ occurs at 38°C . In fact, a small jump at 40°C in the increment of the T_2 relaxation times can be appreciated, indicating that the mobility of the Li^+ ions in the amorphous phase is influenced by the presence of crystallinity in the sample, albeit this effect is small compared to the effect of the doping amount.

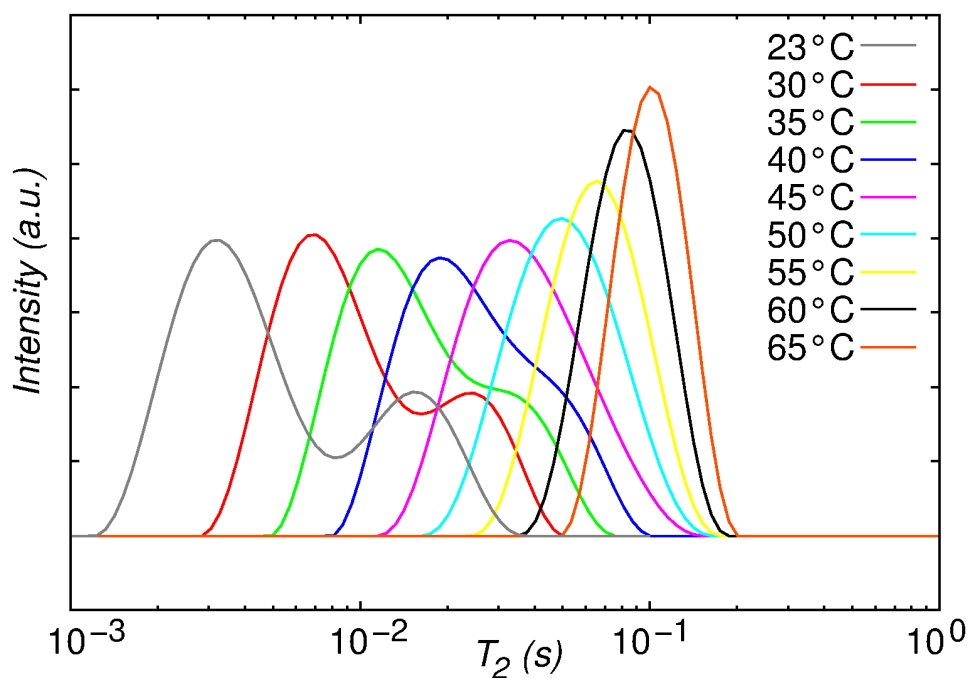


Figure 27 - Temperature dependency of ${}^7\text{Li}$ T_2 distributions in PEG2000 ($y = 8$).
Source: By the author.

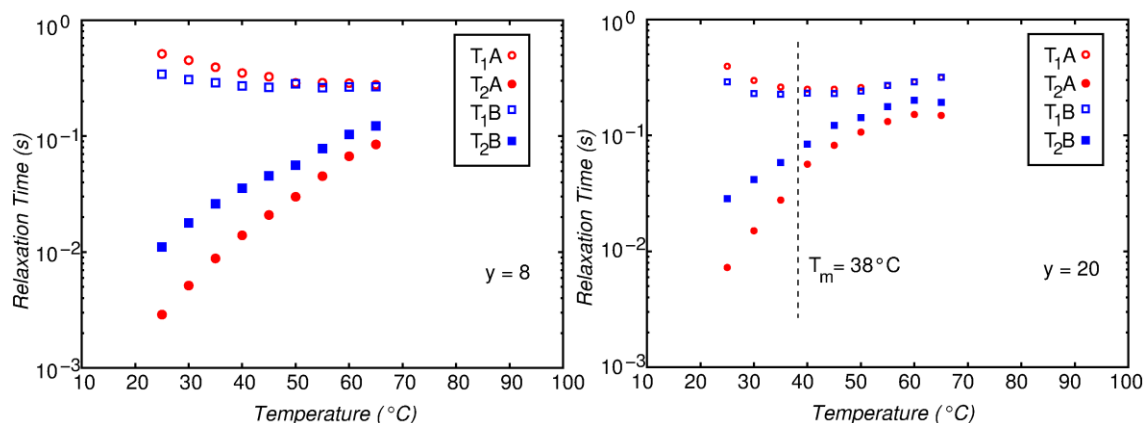


Figure 28 - Temperature dependency of ${}^7\text{Li}$ T_1 and T_2 relaxation times for samples with doping ratios $y = 8$ (left) and $y = 20$ (right). A and B are the short and long T_2 times respectively.

Source: By the author.

Figure 29 shows various two-dimensional maps obtained from the ${}^7\text{Li}$ $T_2 \times T_2$ exchange experiments of sample PEG2000 ($y = 8$), for mixing times τ_m of 1, 60, 500 and 1000 ms. At short mixing times (1 ms) no off-diagonal peaks appear, while with increasing mixing times off-diagonal peaks appear indicating the occurrence of an exchange process between the two different Li^+ ion types. The evolution of the peak intensities for increasing mixing times is shown in Figure 30. The diagonal peaks decay due to the longitudinal and transverse relaxation mechanisms as well as due to the exchange processes. On the other hand, the intensity of the off-diagonal peaks increases due to the ongoing exchange, while simultaneously decaying due to relaxation.

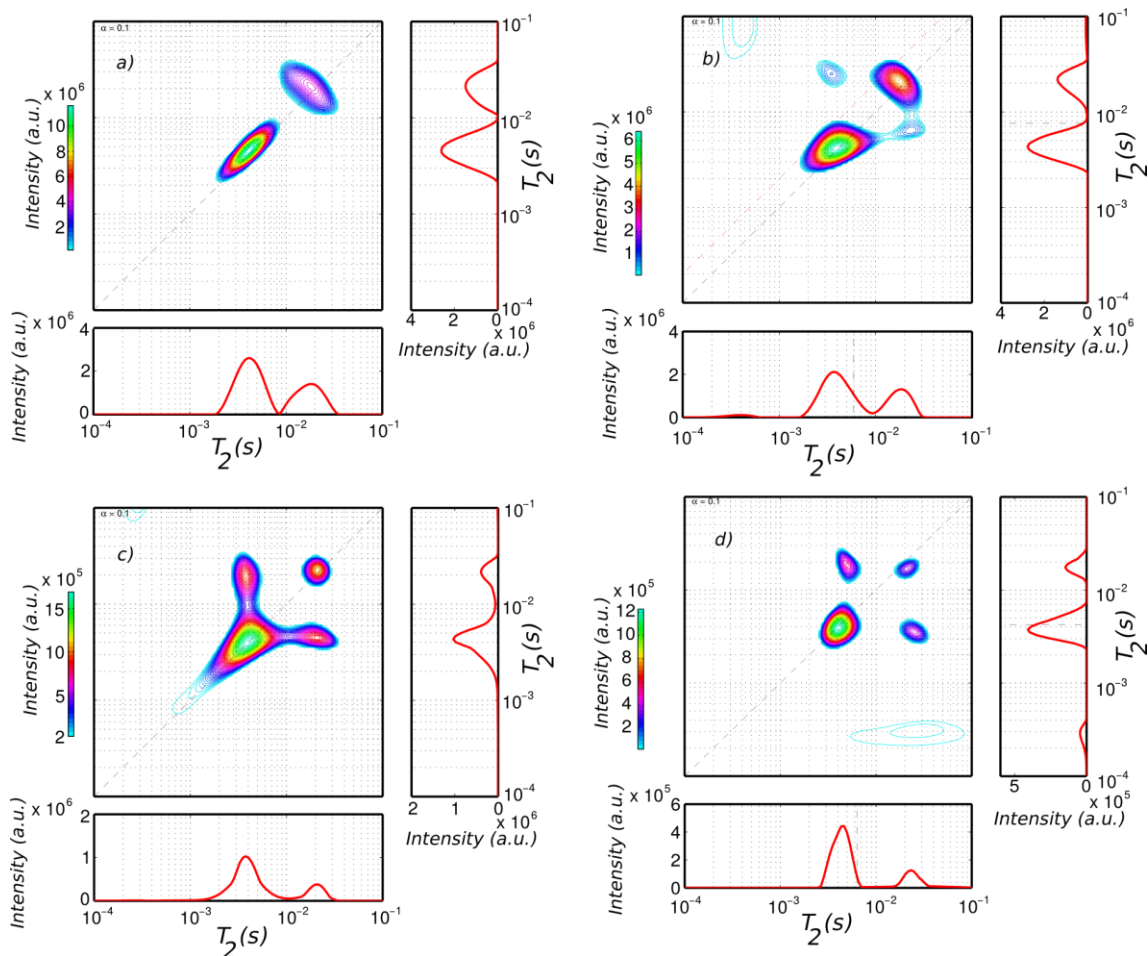


Figure 29 - 2D maps obtained from the ${}^7\text{Li}$ $T_2 \times T_2$ exchange experiment of the sample PEG2000 ($y = 8$) for $\tau_m = 1, 60, 500$ and 1000 ms (for a, b, c and d respectively).

Source: By the author.

By simultaneously fitting all parameters (relaxation times, exchange rates and relative intensities) to the exchange curves (Figure 30) to equation (97) it is possible to obtain the specific exchange rates k and correlation times. (26) The obtained results are summarized in Table 5.

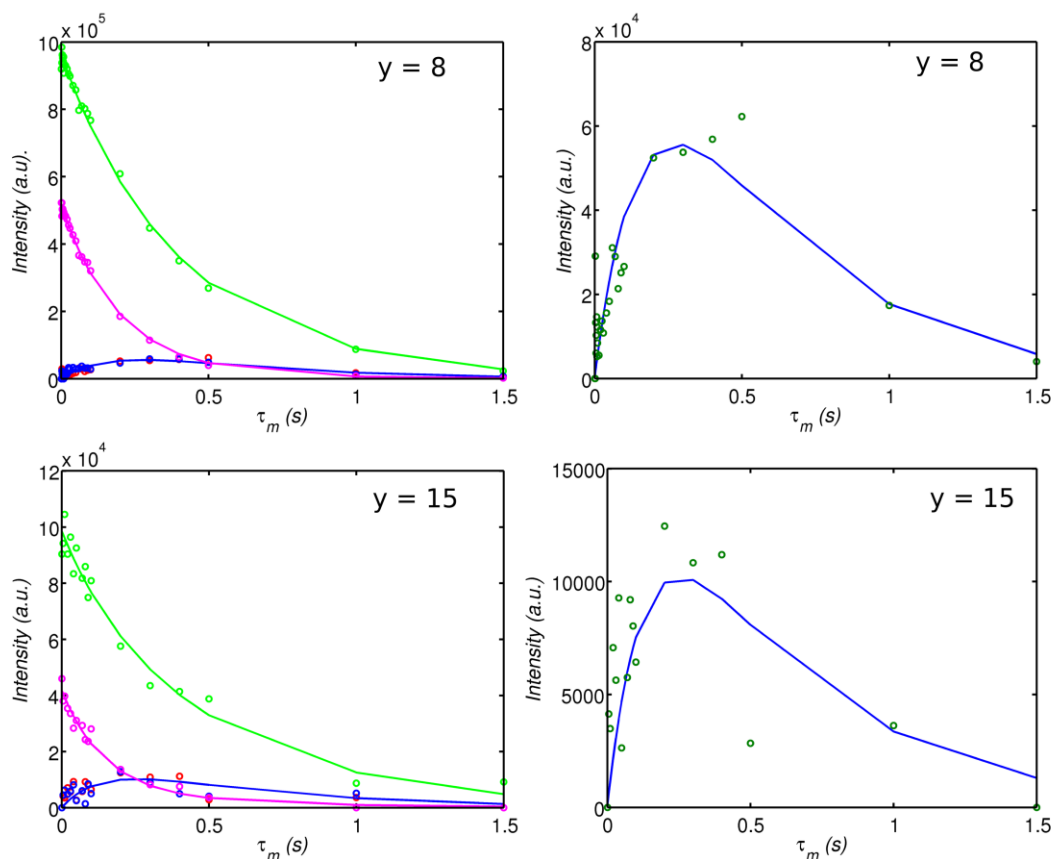


Figure 30 – ${}^7\text{Li}$ signal evolution from 2D $T_2 \times T_2$ exchange experiment and fitted curves. Diagonal peaks: green and magenta; Off-diagonal peaks red and blue (zoom in right figure). For samples PEG2000 ($y = 8$) (top) and PEG2000 ($y = 15$) (bottom).

Source: By the author.

Before doing the 1D $T_2 \times T_2$ exchange experiment it is useful to analyze the effect of the T_2 filter in order to select pertinent filters (Figure 31, left). Once this was done, the mixing time τ_m was varied (Figure 31, right) for the four different chosen filters. The obtained data are shown in Figure 32 to Figure 35. The curves are functions of the initial intensities, the different relaxation times T_1 and T_2 and the exchange ratios k_{ab} and k_{ba} . The parameters obtained from fitting the curves to equation (98), are shown in Table 5, together with the 2D results, and in Figure 36, together with the T_2 relaxation times.

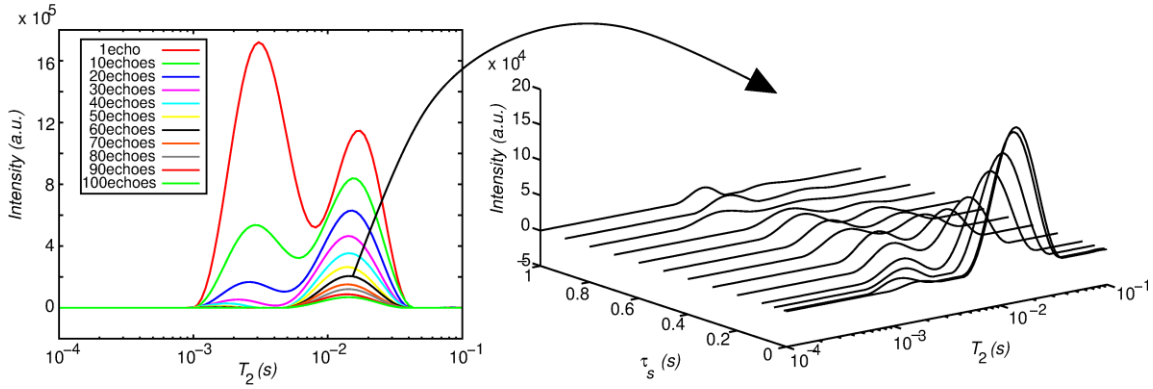


Figure 31 - ^7Li T_2 distributions of the sample PEG2000 ($\gamma = 8$). Left: Filter selection for the 1D $T_2 \times T_2$ experiment. Right: Evolution of T_2 distributions after filter of 60 echoes for increasing τ_m . Source: By the author.

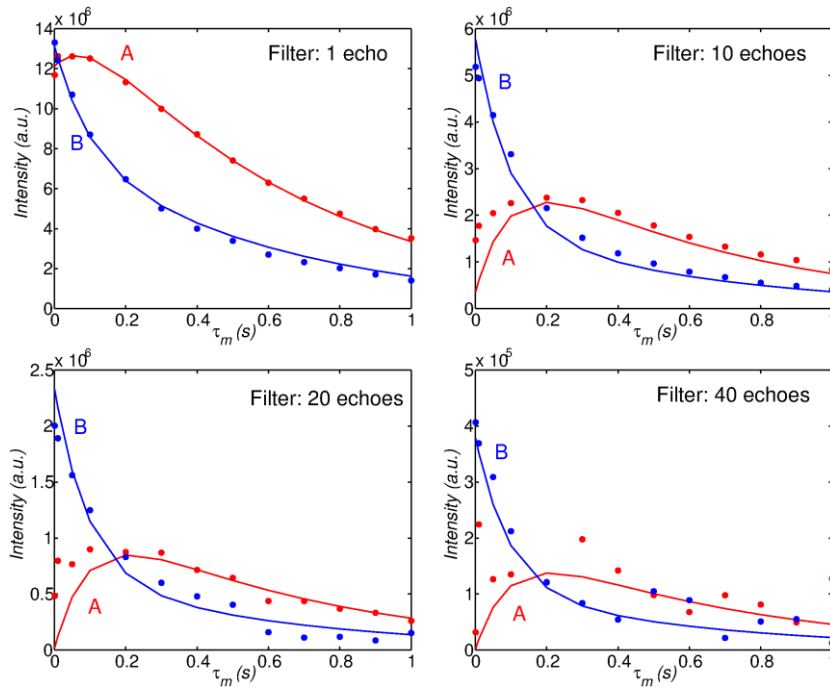


Figure 32 - Fitting curves for the evolution of ^7Li T_2 distribution (A and B are the short and long T_2 times respectively) from the 1D $T_2 \times T_2$ experiment of the sample PEG2000 ($\gamma = 5$). Source: By the author.

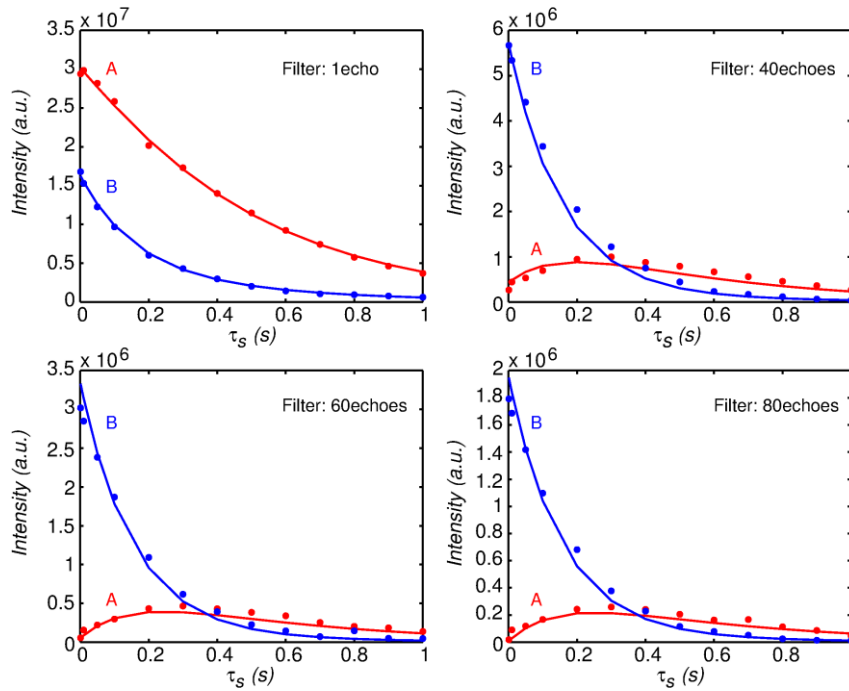


Figure 33 - Fitting curves for the evolution of ${}^7\text{Li}$ T_2 distribution (A and B are the short and long T_2 times respectively) from the 1D $T_2 \times T_2$ experiment of the sample PEG2000 ($\gamma = 8$).

Source: By the author.

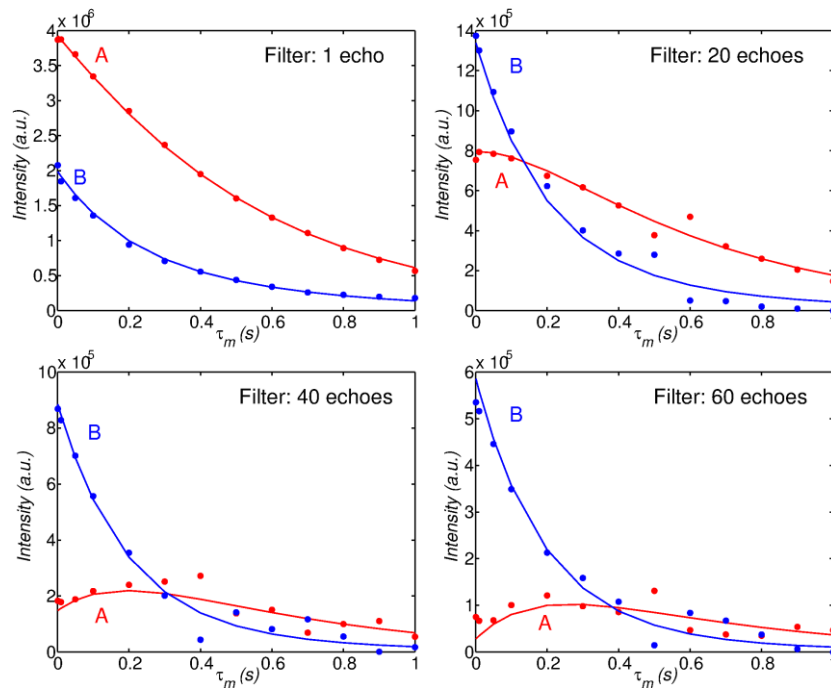


Figure 34 - Fitting curves for the evolution of ${}^7\text{Li}$ T_2 distribution (A and B are the short and long T_2 times respectively) from the 1D $T_2 \times T_2$ experiment of the sample PEG2000 ($\gamma = 15$).

Source: By the author.

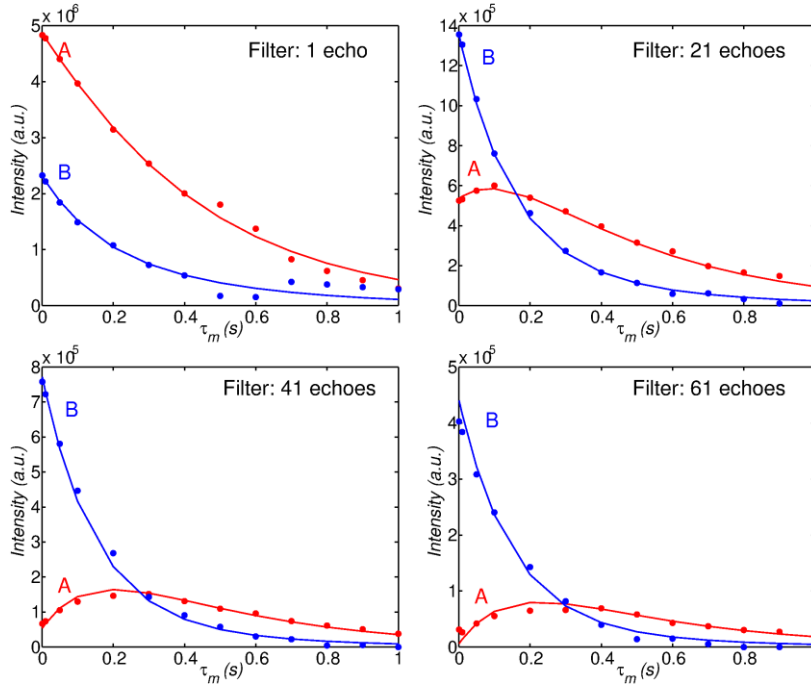


Figure 35 - Fitting curves for the evolution of ${}^7\text{Li}$ T_2 distribution (A and B are the short and long T_2 times respectively) from the 1D $T_2 \times T_2$ experiment of the sample PEG2000 ($y = 20$).

Source: By the author.

Table 5 shows the obtained results. By looking at the initial intensities M_{0a} it can be seen that estimating the signal intensities from the 2D experiment has less reliability, if compared to the areas obtained from the CPMGs (Table 4), then estimating them from the 1D experiment, which shows very good consistency with the CPMGs. Furthermore, the obtained exchange rates from both experiments are consistent in the order of magnitude and in terms of the presented trends. The largest exchange rate k was observed for the sample with the largest doping level ($y = 5$), then, after passing a minimum, k_{ab} increases for decreasing doping amounts. Exchange rates and viscosity of the sample are not directly related. This result implies that higher mobility of the ions does not lead to higher exchange rates and furthermore, it may indicate that for good conductivity, the absence of exchange could be advantageous.

Finally, the root mean square deviation (RMSD) of the exchange curves was obtained according to:

$$RMS = \sqrt{\frac{\sum_i^n (x_{i,\text{exp}} - x_{i,\text{sim}})^2}{n}} \quad (107)$$

The 1D variant presents smaller RMSD, even though the experiment time is considerably shorter. Thus, the 1D experiment presents great advantages as compared to the 2D variant, at least for samples with only two sites.

Table 5 - Initial magnetization, exchange rates and root mean square deviations (RMSD) obtained from the one and two-dimensional ${}^7\text{Li}$ $T_2 \times T_2$ correlation experiments for PEG2000.

Sample PEG 2000	2D				1D			
	M_{0a} (%)	k_{ab} (s^{-1})	k_{ba} (s^{-1})	RMSD (%)	M_{0a} (%)	k_{ab} (s^{-1})	k_{ba} (s^{-1})	RMSD (%)
y = 5	56	8.1	10.4	42	64	3.1	5.4	24
y = 8	73	0.34	0.93	21	67	0.60	1.22	13
y = 15	88	0.29	2.25	31	68	0.67	1.43	13
y = 20	80	0.75	2.89	30	70	0.91	2.13	10

Source: By the author.

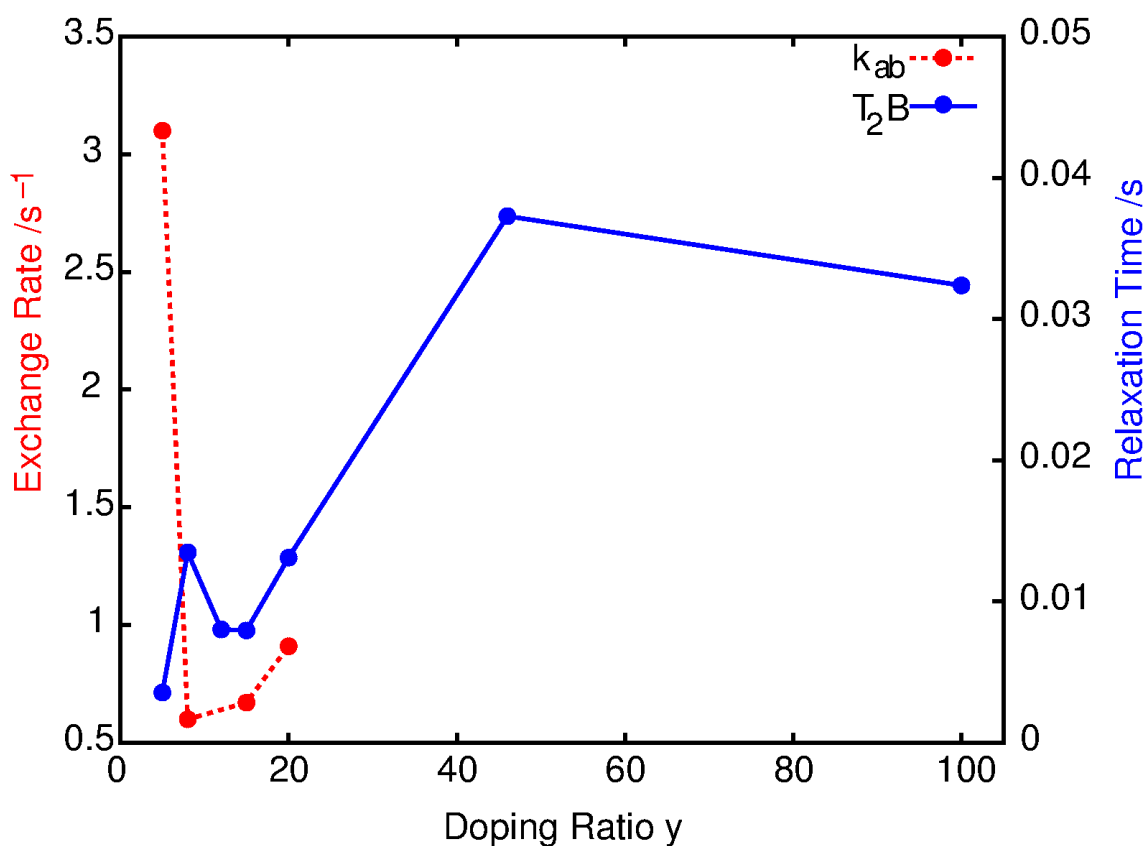


Figure 36 - Evolution of the ${}^7\text{Li}$ T_2 relaxation time (long component) and the exchange rate k_{ab} as functions of the doping ratio y at room temperature.

Source: By the author.

4.2 Solid Triblock Copolymer Electrolyte PS-PEO-PS/LiTFSI

4.2.1 The Polymer PS-PEO-PS

Typical ^1H MAS and $^{13}\text{C}\{^1\text{H}\}$ CPMAS, with TOSS and heteronuclear decoupling, spectra of the triblock copolymers PS-PEO-PS are shown in Figure 37 and Figure 38, respectively. The ^1H spectrum shows three different components, PS, which has a broad peak form (FWHM in the order of 100 ppm), crystalline PEO, which also has a broad peak form, and overlaps with PS, and amorphous PEO, which has a much narrower peak (FWHM in the order of one ppm). The presence of lithium salts causes a broadening of the sharp peak, probably indicating a reduction of mobility of the polymeric chains. The peak at 4.4 ppm could not be assigned. The measured ^1H fractions are consistent with the expected mass fractions of the structure, presence of crystalline PEO was also detected in samples with high doping level, even though not indicated by the DSC measurements shown in Table 2, probably due to their small intensity. In the carbon spectrum the peaks are assigned to the respective PS sites (42) and to PEO. Note that CP spectra are not quantitative. For instances mobile PEO does not CP with efficiency, and thus the observed PEO signal is only from the crystalline part.

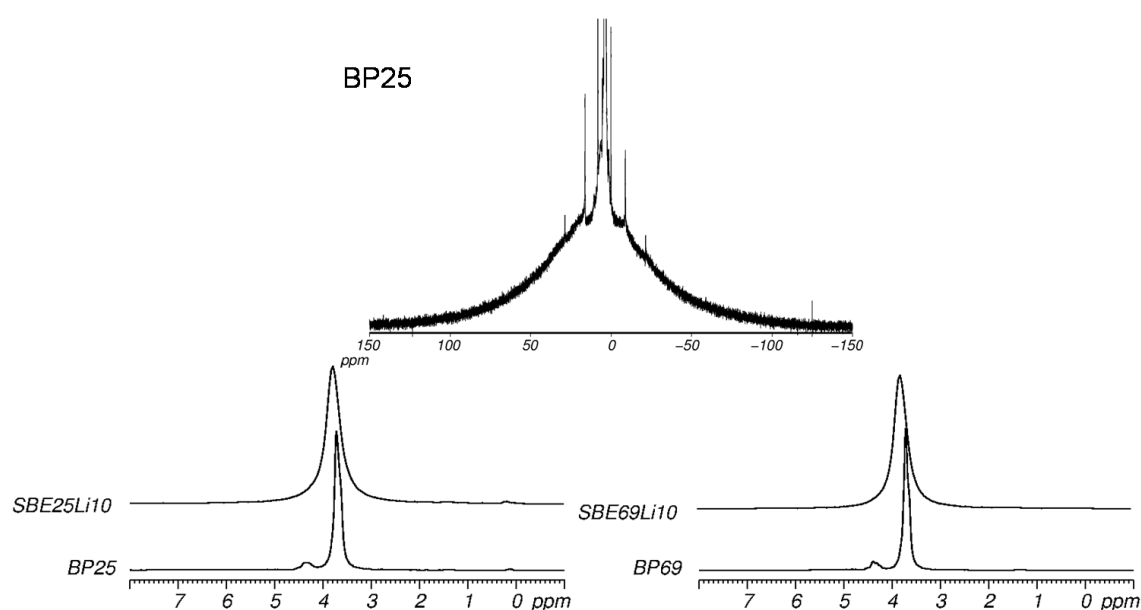


Figure 37 - ^1H MAS spectra of various triblock copolymers obtained at a spinning speed of 5 kHz and at room temperature. PS and crystalline PEO cause broad component, amorphous PEO sharp. Above, the sharp peak was cut off, in order to show the broad peak. Below, only the sharp peak is shown.

Source: By the author.

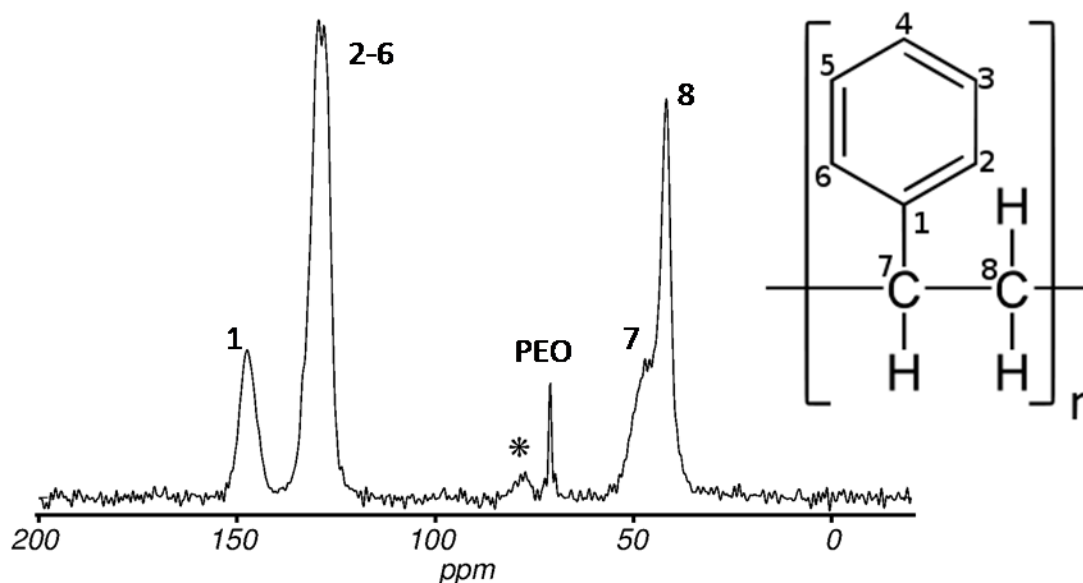


Figure 38 - $^{13}\text{C}\{^1\text{H}\}$ CPMAS with TOSS spectrum of sample SBE25-10, at a spinning speed of 5 kHz and at room temperature. The asterisk indicates a rotational sideband.

Source: By the author.

In a next step, the influence of the doping amounts and of the PS chain lengths on the rotating frame relaxation time $T_{1\rho}$ of the polymer was analyzed. $T_{1\rho}$ relaxation times are sensible to motions in the region of tens of kHz. Here only the $T_{1\rho}$ relaxation times obtained from direct ^1H measurements are shown, but the results obtained from $^{13}\text{C}\{^1\text{H}\}$ CP are equivalent. $T_{1\rho}$ of PS and amorphous PEO are of the same order of magnitude, while crystalline PEO presents $T_{1\rho}$ one order of magnitude smaller. The $T_{1\rho}$ of PS decreases for an increasing PEO/PS ratio, this indicates an increment in its mobility. (81) This behavior was expected, since for smaller PS chain lengths the mobility of the PS domain will be stronger affected by the less rigid PEO domain.

In the case of the PEO phases it can be seen that in highly doped samples only the crystalline part is affected by the PEO/PS ratio and the amorphous part stays stable, while for low salt concentrations the exact opposite is observed. The position of the $T_{1\rho}$ -autocorrelation time curve of amorphous PEO is strongly dependent on its doping amount. (82) Therefore, it would be interesting to do a temperature dependent study of $T_{1\rho}$, to confirm on which side of the $T_{1\rho}$ -autocorrelation time curve we are. However for pure amorphous PEO a decrease of $T_{1\rho}$ indicates a decrease of mobility, which would be the case for the samples with $y = 25$. It is not clear why shorter PS chains would decrease the mobility of the amorphous PEO. However, a possible explanation could be that since the presence of PS inhibits folding of the PEO chains, (16) the inter- and intra-molecular bindings of the PEO chains are debilitated. On

the other hand, the fact that $T_{1\rho}$ of amorphous PEO of the samples with $y = 10$ stays constant could indicate that the mobility of this phase is stronger affected by the salt due to the higher polarity.

The crystalline PEO phase of the samples with $y = 25$ are not affected by the PS chain length, while for the highly doped samples $T_{1\rho}$ decreases, which indicates a higher mobility. (82)

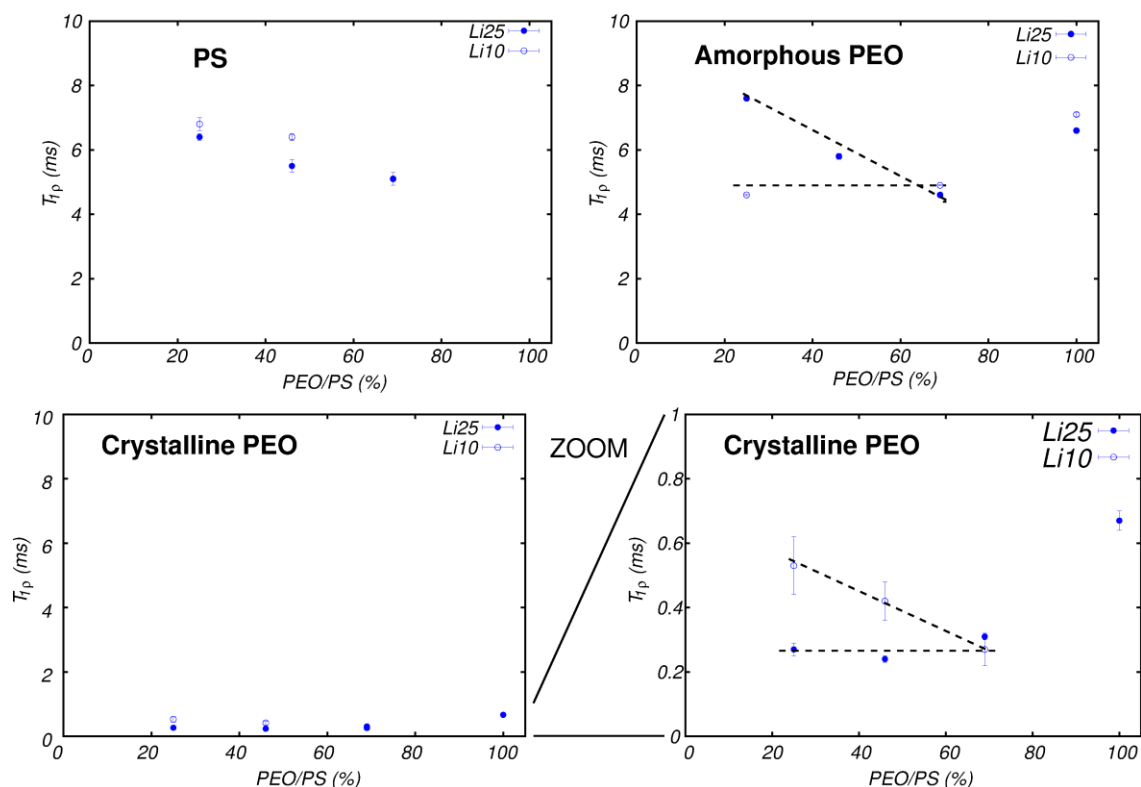


Figure 39 - $T_{1\rho}$ obtained from ^1H spectra for the doped triblock copolymers at a spinning speed of 5 kHz and at room temperature for varying PEO/PS ratio. Some observed trends are signaled with dotted lines.

Source: By the author.

Furthermore, the effects of the PS chain length and the doping level on $T_{1\rho}$ was compared with its effects on the FWHM for the amorphous PEO phase. In Figure 40 both are shown next to each other. It can be seen that in this case they behave in a completely analogous way; both measurements are sensible to motional variations in the same range. For the sample with a doping level of $y = 25$ the line width increases with a reduction of PS, also indicating a decrease of mobility.

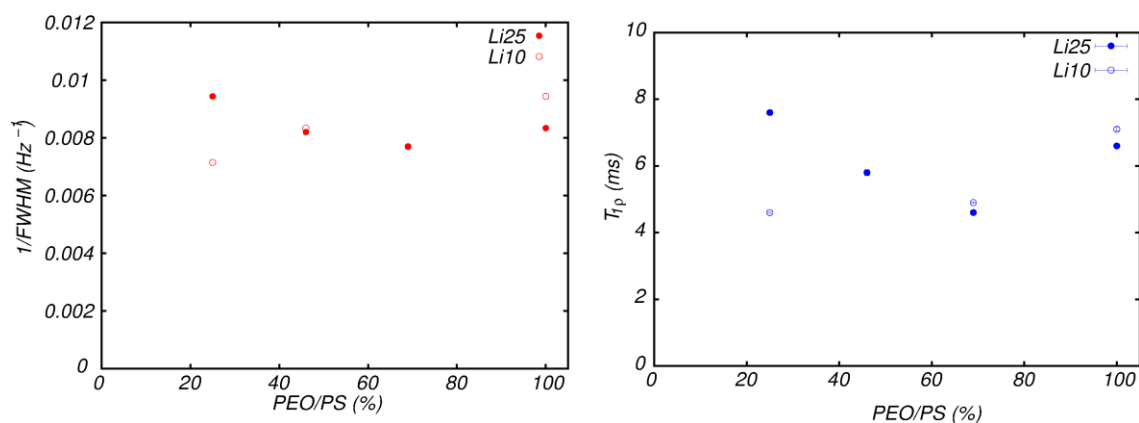


Figure 40 - Comparison between $T_{1\rho}$ and the inverse FWHM of amorphous PEO for the doped triblock copolymers for varying PEO/PS ratio.

Source: By the author.

Figure 41 and Figure 42 show the evolution of the magnetization obtained in the Goldman-Shen spin diffusion experiments. After the selection time the PS signal was filtered out. With increasing mixing times spin diffusion occurs and the intensity of the PEO signal decays while the intensity of the PS signal increases until reaching equilibrium. Note that a T_1 correction was done.

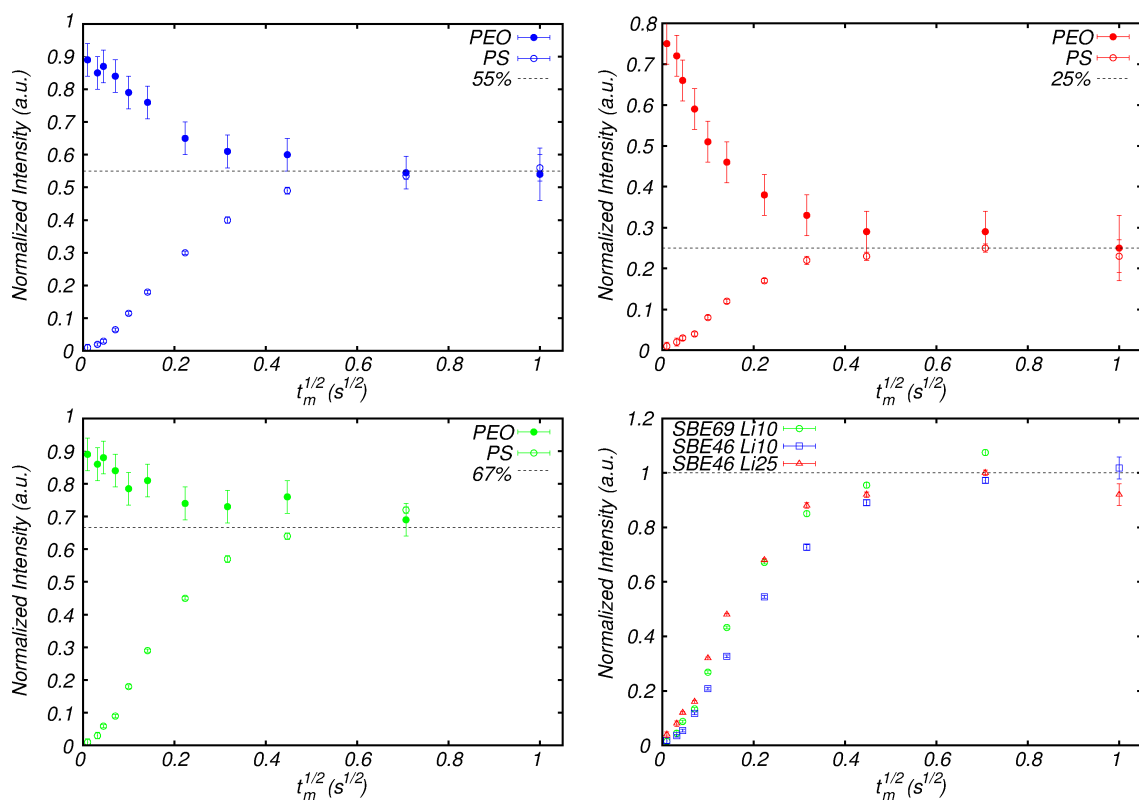


Figure 41 - Spin diffusion of doped triblock copolymers SBE46Li10 (blue), SBE46Li25 (red) and SBE69Li10 (green) obtained with the Goldman-Shen experiment with $^{13}\text{C}\{^1\text{H}\}$ detection at room temperature. The equilibrium (dotted) line was obtained from the ^1H FID intensities.

Source: By the author.

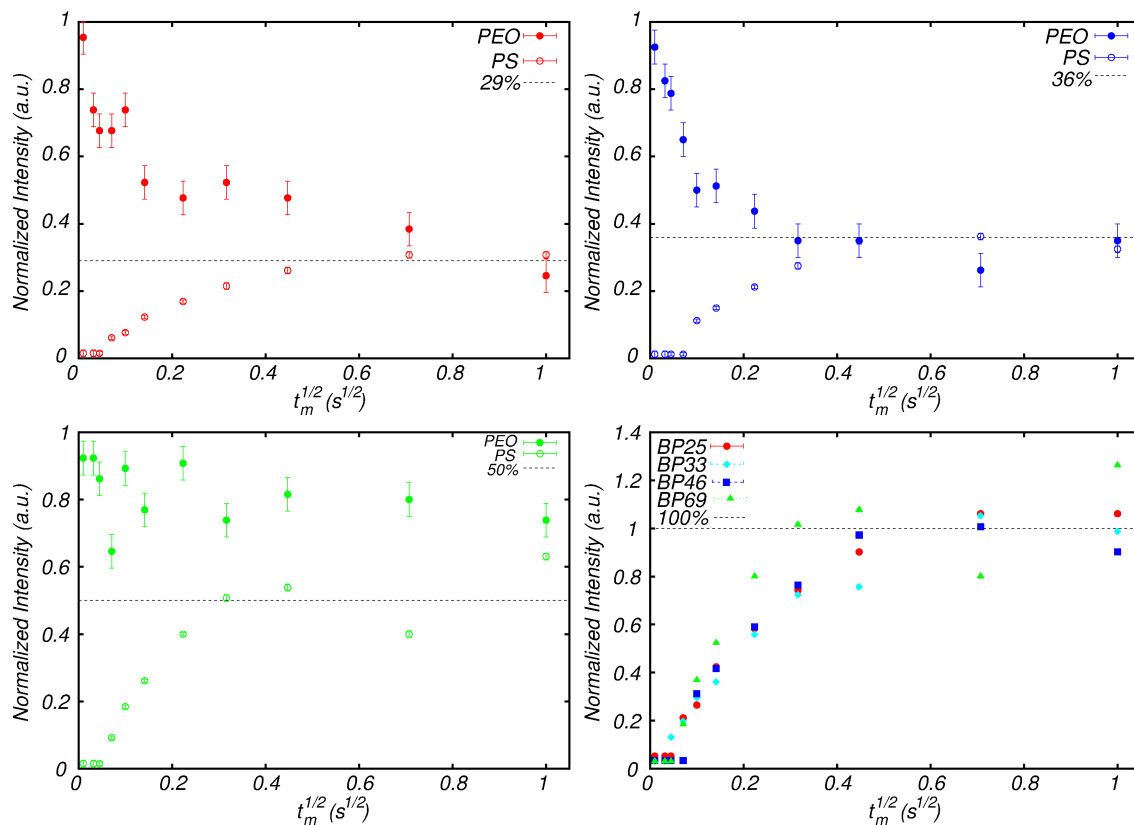


Figure 42 - Spin diffusion of undoped triblock copolymers BP25 (red), BP33 (turquoise), BP46 (blue) and BP69 (green) obtained with the Goldman-Shen experiment with $^{13}\text{C}\{^1\text{H}\}$ detection at room temperature. The equilibrium (dotted) line was obtained from the ^1H FID intensities.

Source: By the author.

The results obtained from spin diffusion curves are summarized in Table 6. Some trends can be seen and are in agreement with TEM measurements of similar samples (not shown here). First, the inter-domain distance d_I increases with increasing PS chain length, as expected. Furthermore d_I also increases with increasing Li^+ ion concentration.

Table 6 - Results from spin diffusion measurements, $D_{RP} = 0.8 \text{ nm}^2/\text{ms}$ and $\varepsilon = 1$ was used. Diffusion coefficient of the mobile phase (D_{MP}); mobile phase diameter (d_{MP}); inter-domain distance (d_I).

Sample	D_{MP} (nm^2/ms)	d_{MP} (nm)	d_I (nm)
SBE46Li10	0.069	12.1	26.9
SBE46Li25	0.067	7.2	16.0
SBE69Li10	0.075	16.9	25.4
BP25	0.029	4.8	18.8
BP33	0.030	6.1	18.3
BP46	0.029	5.8	12.6
BP69	0.025	5.5	8.11

Source: By the author.

4.2.2 The Salt LiTFSI

The doped triblock copolymers were also studied in terms of the lithium ion mobility through ^7Li relaxation measurements, analogue to the techniques used to study the doped homopolymer PEG. The measured ^7Li spectra are shown in Figure 43. Most of the spectra could be fitted with two curves, a broad, having a Gaussian-, and a sharp, having a Lorentzian lineshape. The results of the deconvolution are summarized in Table 7. Note that for sample SBE46-25 three curves were needed, however, both Lorentzian presented the same linewidth, and thus T_2 time, and were therefore added together in Table 7.

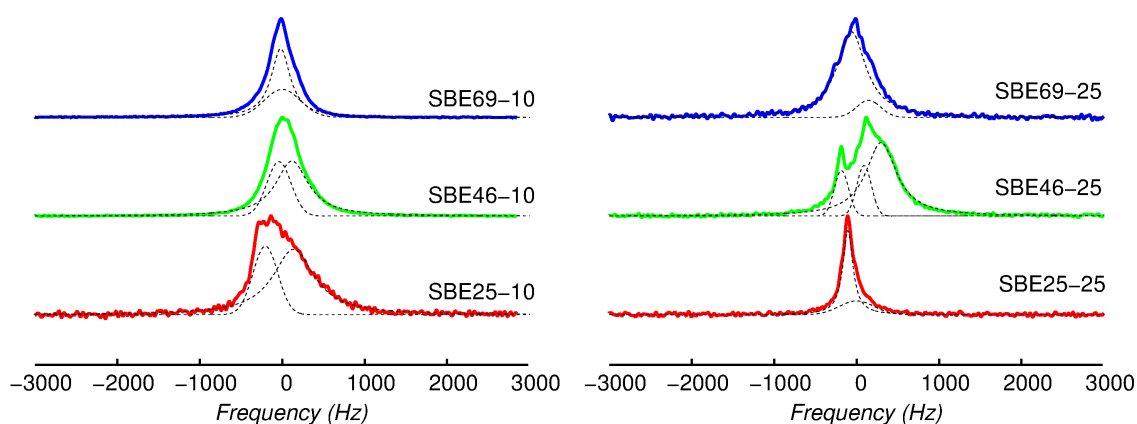


Figure 43 - ^7Li normalized spectra for the doped triblock copolymers PS-PEO-PS at 25°C , deconvolution shown with dotted curves.

Source: By the author.

None of the spectra presented a quadrupolar powder pattern. The DSC data given in Table 2 in chapter 3.1 indicated that the highly doped samples ($y = 10$) do not present crystallinity in the PEO block. The weakly doped samples ($y = 25$) have a reduction of the PEO crystallinity as compared to the pure samples and no further phase transition appears. Even though, the $T_{1\rho}$ measurements showed some residual crystallinity also for the highly doped samples, DSC measurements and ^7Li spectra indicate that the present crystalline phase correspond only to the pure PEO phase and subsequently, all Li^+ ions are in the amorphous phase of the PEO block. This will enable us to compare the results of the high molecular weight triblock copolymer with the results from the low molecular weight PEG samples.

^7Li T_2 relaxation times were measured with the CPMG experiment. The obtained T_2 time distributions are shown in Figure 44 and Table 7. All samples present two different T_2 regions with a ratio of approximately 70-30, being the shorter T_2 always stronger populated. The T_2 times obtained from the CPMG are considerably longer than the ones obtained from the FID, indicating strong heteronuclear dipolar couplings. Furthermore, shorter T_2 relaxation times are related to lower mobility. $T_1 \times T_2$ maps (shown for SBE69-10 in Figure 45) have shown that the component with shorter T_2 presents longer T_1 , indicating that the samples are in the high viscosity regime of the BPP curve. In summary, the Li^+ ions in this large molecular mass triblock copolymer present analogue motional properties as compared to the Li^+ in the low molecular weight PEG. Furthermore, the T_2 values are also very similar as compared to PEG. Therefore, the same hypothesis of the origin of the two different species can be applied: presence of isolated ion-pairs or different binding mechanisms between the ions and the polymer chain.

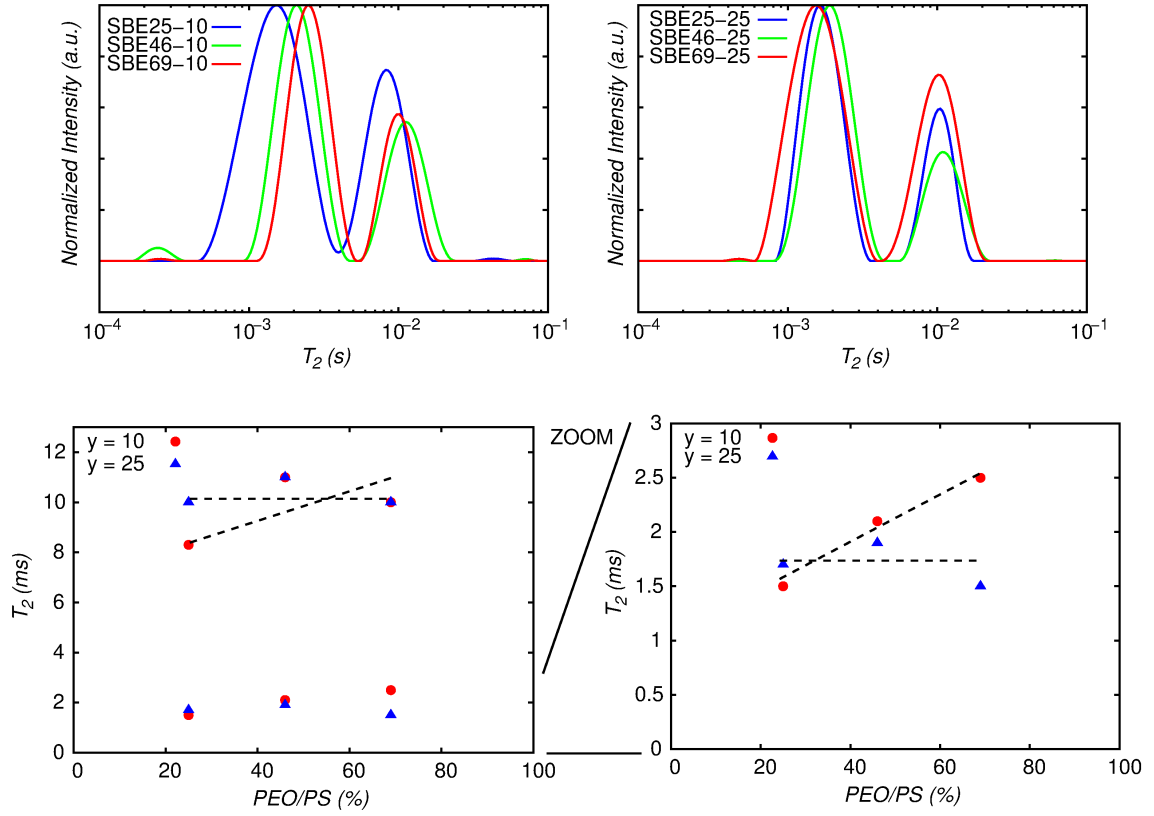


Figure 44 - Top: ${}^7\text{Li}$ T_2 distributions obtained via ILT from the CPMG experiment for the doped triblock copolymers PS-PEO-PS at 25°C. Bottom: Summary of the T_2 values as function of the PEO/PS ratio. Some observed trends are signaled with dotted lines.

Source: By the author.

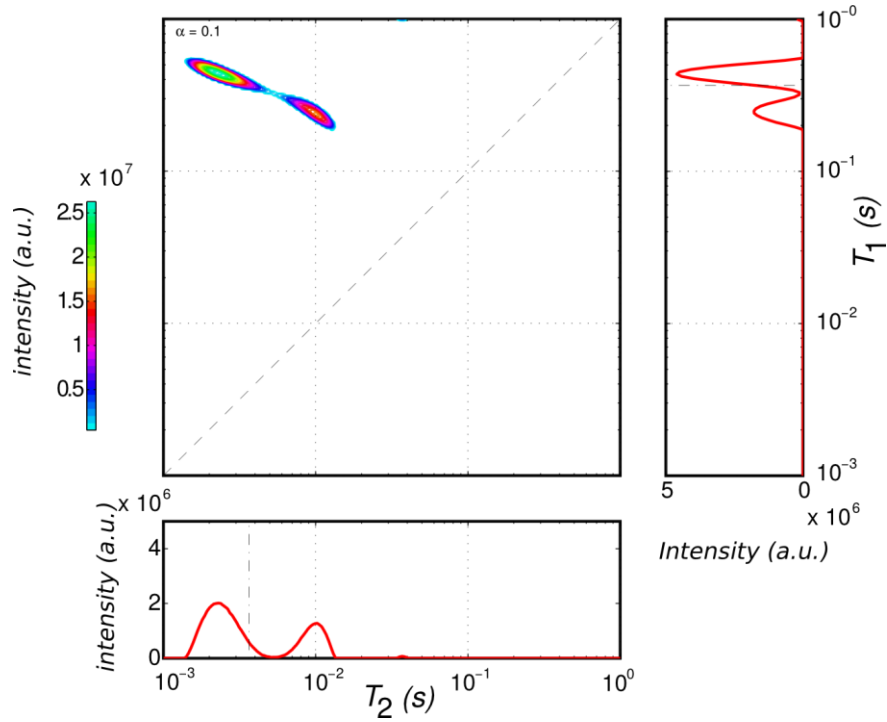


Figure 45 - ${}^7\text{Li}$ $T_1 \times T_2$ 2D map of the sample SBE69-10 at 25°C.

Source: By the author.

By comparing the different block copolymers with each other, it can be seen that the amount of PS has only little influence on the mobility of the Li^+ ions. However, for the highly doped sample ($y = 10$, red dots in Figure 44), a trend can be observed: An increment in the PS block molar mass reduces the mobility of both different types of lithium ions. On the other hand, for the samples with less salt ($y = 25$, blue triangles in Figure 44) the ^7Li T_2 relaxation times are not affected considerably. This can be explained by the presence, and absence, of the pure PEO crystalline phase. Large amounts of crystalline PEO should have a stronger influence on the mobility of the amorphous PEO phases than the PS blocks. In the absence of a crystalline PEO phase, the PS chains should have more influence and increase the overall stiffness of the sample.

These results appear to show different tendencies than the $T_{1\rho}$ measurements of the amorphous polymer chains, where it was found that an increment in the PS fraction reduced the mobility of the amorphous PEO chains for the samples with a doping amount of $y = 25$ while remaining constant for the samples with $y = 10$. This apparent contradiction could indicate that for a high mobility of the present ionic species the amorphous PEO chains must be well folded, even though the mobility of the chains themselves is reduced. In any case, this shows the complexity of the motional behavior of these systems.

Table 7 - ^7Li T_2 relaxation time distribution obtained from the CPMG experiment for the doped triblock copolymers PS-PEO-PS.

Sample	FID				CPMG			
	rigid		mobile		Rigid		mobile	
	T_2 (ms)	Area (%)	T_2 (ms)	Area (%)	T_2 (ms)	Area (%)	T_2 (ms)	Area (%)
SBE25-10	0.52	69	0.90	31	1.5	67	8.3	33
SBE46-10	0.66	66	0.92	34	2.1	67	11	33
SBE69-10	0.62	34	1.1	62	2.5	68	10	32
SBE25-25	0.64	28	2.2	72	1.7	70	10	30
SBE46-25	0.70	70	1.1	30	1.9	73	11	27
SBE69-25	0.75	90	0.93	10	1.5	64	10	36

Source: By the author

Finally, $T_2 \times T_2$ exchange measurements were done on the solid block copolymer electrolytes. Presence of exchange was confirmed with $T_2 \times T_2$ 2D exchange maps (Figure 46). Quantification of the exchange rates was done with the T_2 -filtered 1D variant. The results are

shown in Figure 47 to Figure 54. Due to the low amount of sample available, the signal to noise ratio was very poor, especially for larger filters this led to high dispersion of the T_2 relaxation time distributions obtained from the ILT of the exponential decays. However, the fitted relative intensities as well as the T_1 and T_2 relaxation times showed good agreement with the $T_1 \times T_2$ experiments and it was possible to observe exchange between both sites in all samples.

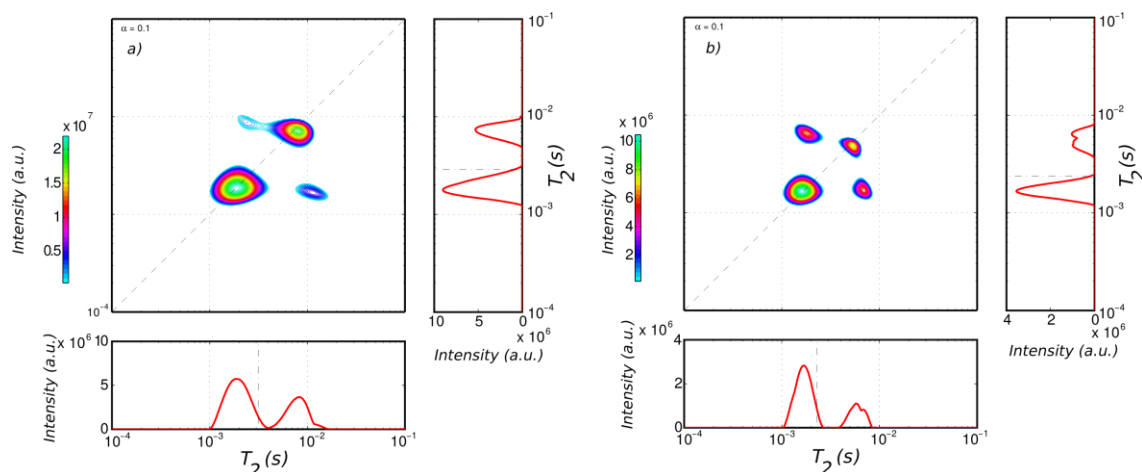


Figure 46 - 2D maps obtained from the ^7Li $T_2 \times T_2$ exchange experiment of the sample SBE69-10 for $\tau_m = 1$ and 500 ms (for a, and b respectively) at room temperature.

Source: By the author.

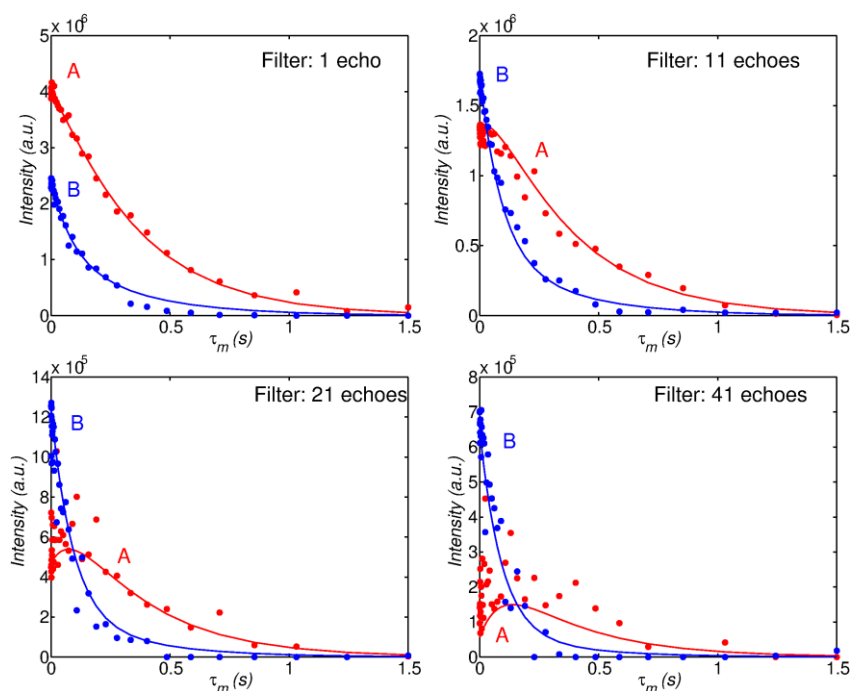


Figure 47 - Fitting curves for the evolution of ^7Li T_2 distribution (A and B are the short and long T_2 times respectively) from the 1D $T_2 \times T_2$ experiment of the triblock copolymer SBE25-10 at 25°C.

Source: By the author.

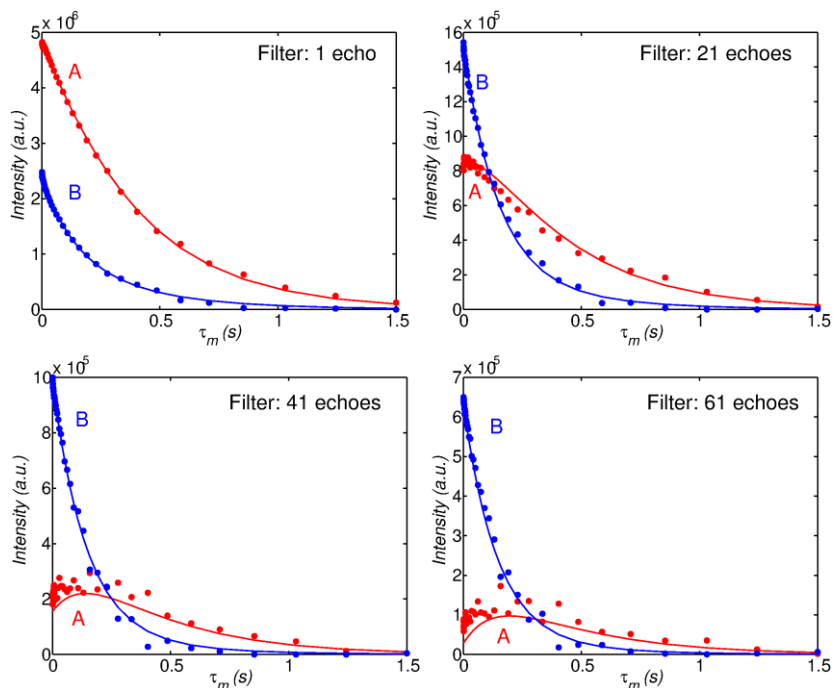


Figure 48 - Fitting curves for the evolution of ${}^7\text{Li}$ T_2 distribution (A and B are the short and long T_2 times respectively) from the 1D $T_2 \times T_2$ experiment of the triblock copolymer SBE46-10 at 25°C.
Source: By the author.

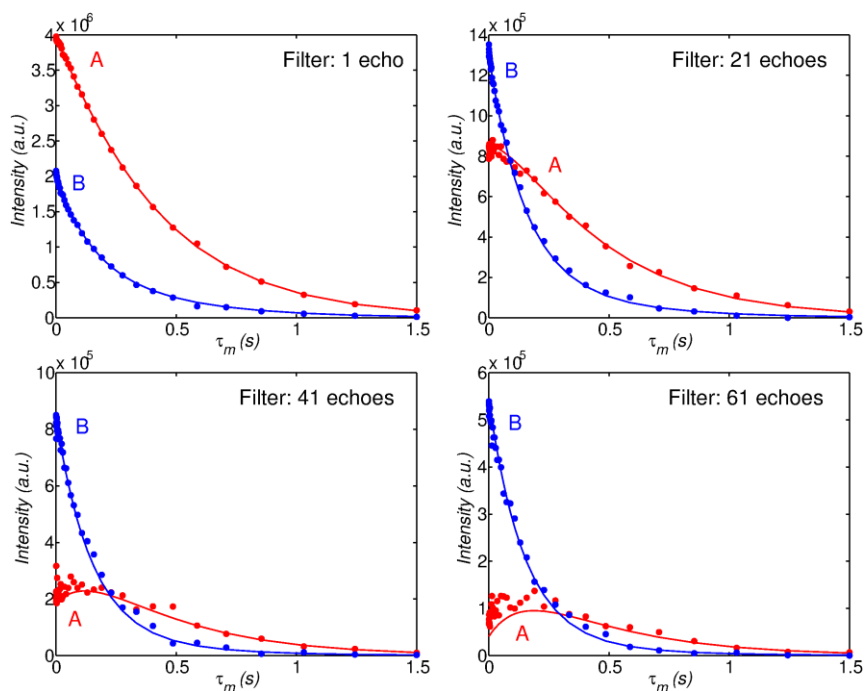


Figure 49 - Fitting curves for the evolution of ${}^7\text{Li}$ T_2 distribution (A and B are the short and long T_2 times respectively) from the 1D $T_2 \times T_2$ experiment of the triblock copolymer SBE69-10 at 25°C.
Source: By the author.

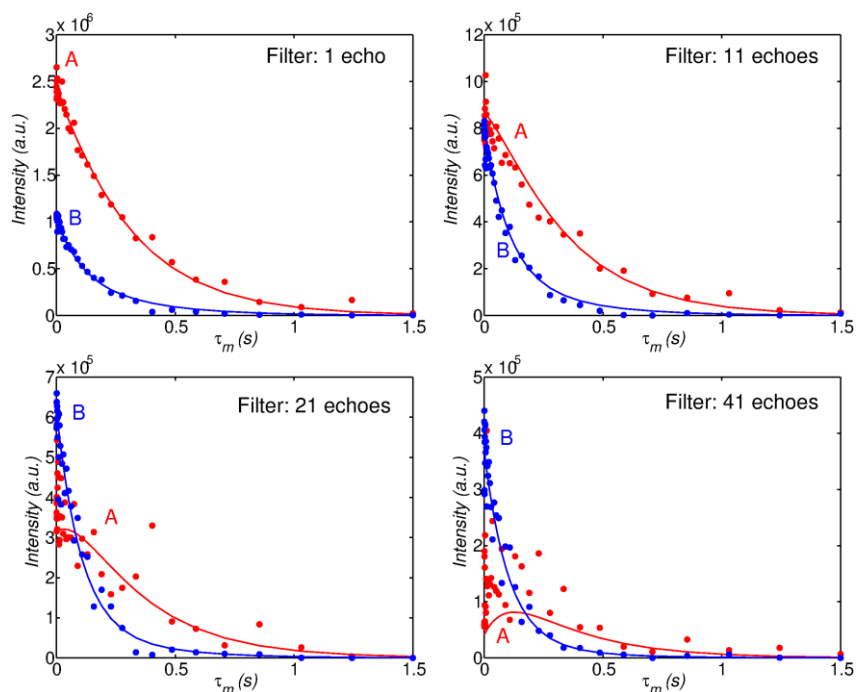


Figure 50 - Fitting curves for the evolution of ${}^7\text{Li}$ T_2 distribution (A and B are the short and long T_2 times respectively) from the 1D $T_2 \times T_2$ experiment of the triblock copolymer SBE25-25 at 25°C .
Source: By the author.

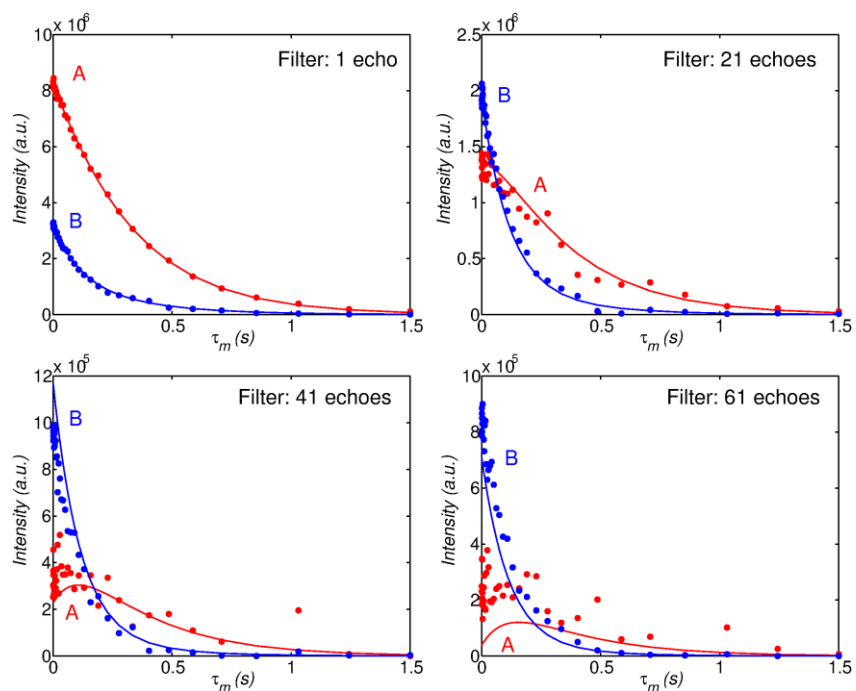


Figure 51 - Fitting curves for the evolution of ${}^7\text{Li}$ T_2 distribution (A and B are the short and long T_2 times respectively) from the 1D $T_2 \times T_2$ experiment of the triblock copolymer SBE46-10 at 25°C .
Source: By the author.

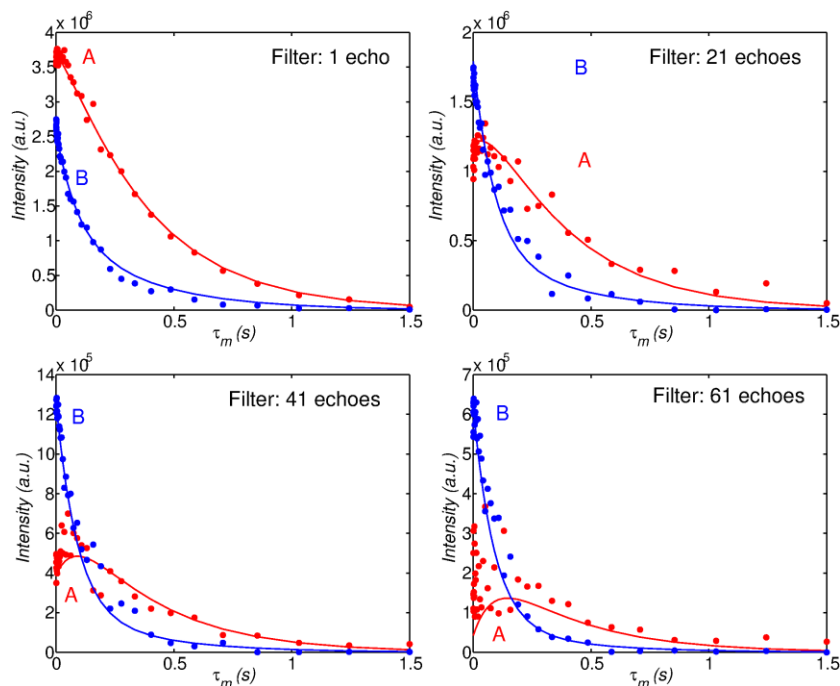


Figure 52 - Fitting curves for the evolution of ${}^7\text{Li}$ T_2 distribution (A and B are the short and long T_2 times respectively) from the 1D $T_2 \times T_2$ experiment of the triblock copolymer SBE69-25 at 25°C.

Source: By the author.

The obtained exchange rates are listed in Table 8. With this quantity of measured samples and the large margin of error it was not possible to determine any trends. Therefore, it would be interesting to measure more samples. Comparing this values to the results obtained for PEG, it can be seen that the obtained values are of the same order of magnitude (disregarding PEG2000 $y = 5$).

Table 8 - Initial magnetization, exchange rates and root mean square deviations (RMSD) obtained from the one-dimensional ${}^7\text{Li}$ $T_2 \times T_2$ correlation experiments for the triblock copolymers PS-PEO-PS.

Sample	M_{0a} (%)	k_{ab} (s^{-1})	k_{ba} (s^{-1})	RMSD (%)
SBE25-10	65	1.7	3.2	18
SBE46-10	68	0.75	1.6	11
SBE69-10	68	0.78	1.6	9
SBE25-25	72	1.1	2.7	21
SBE46-25	73	0.79	2.2	23
SBE69-25	61	2.0	3.2	18

Source: By the author

4.3 PEGD Multiple Quantum Coherence Diffusion Measurements

4.3.1 ^7Li NMR Spectroscopy of PEGD-LiClO₄ ($y = 5$)

In doped PEGD a ^7Li quadrupolar pattern is observed. This is the case even at temperatures above the melting temperature. This was attributed to the presence of an ordered phase which remains up to an order-disorder transition temperature T_{OD} which depends on the doping ratio y . (53) Figure 53 shows the ^7Li spectrum of PEGD ($y = 5$) at various temperatures. The quadrupole splitting $\omega_Q/2$ at room temperature is approximately 500 Hz, and 400 Hz at 50°C. Note that at temperatures around the melting point both phases coexist.

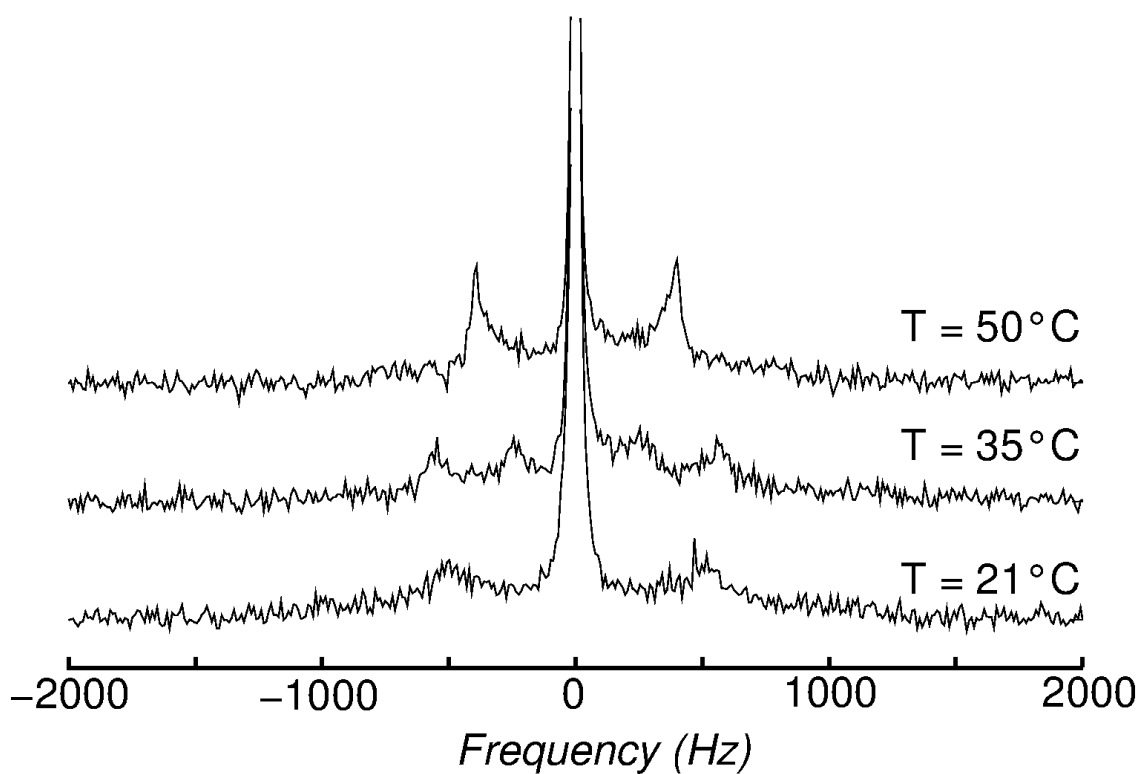


Figure 53 - ^7Li PEGD-LiClO₄ ($y = 5$) spectra at various temperatures.
Source: By the author.

4.3.2 Multiple Quantum Coherence Excitation

Theoretical Calculations

In first place, the pulse sequence for exciting triple quantum coherence of a 3/2 spin was studied in terms of the density matrix and considering the commutation relations given by Bowden and Hutchison (58,59) for hard rf-pulses (during the pulses no internal interaction is considered). At equilibrium the magnetization is oriented along the z-axis:

$$\hat{\rho}(0) \sim \hat{I}_z \sim \hat{T}_{10} \quad (108)$$

The action of an rf pulse is given by:

$$\begin{aligned} \hat{\rho}(1) &= e^{-i\hat{H}t_1} \hat{\rho}(0) e^{i\hat{H}t_1} = e^{-it_1\hat{T}_{11}(a)} T_{10} e^{it_1\hat{T}_{11}(a)} \\ \hat{\rho}(1) &= \hat{T}_{10} \cos(\omega_1 t_1) - i\hat{T}_{11}(s) \sin(\omega_1 t_1) \end{aligned} \quad (109)$$

Where (s) and (a) refer to the symmetric and antisymmetric combinations, respectively, of the $\hat{T}_{\pm 1}$ operator ($\hat{T}_{11}(s) = \frac{1}{i\sqrt{2}}[\hat{T}_{11} + \hat{T}_{1-1}]$; $\hat{T}_{11}(a) = \frac{1}{\sqrt{2}}[\hat{T}_{11} - \hat{T}_{1-1}]$). Looking at equation (109), it can be concluded that a single hard rf-pulse will not create coherence of higher order. Let the pulse be a $\pi/2_x$ pulse:

$$\hat{\rho}(1) = i\hat{T}_{11}(s) \quad (110)$$

After the pulse, let the magnetization evolve under the effect of the quadrupolar Hamiltonian:

$$\begin{aligned} \hat{\rho}(2) &= e^{-i\hat{H}_Q t_2} \hat{\rho}(1) e^{i\hat{H}_Q t_2} \\ \hat{\rho}(2) &= \frac{i}{5} \hat{T}_{11}(s) [3 \cos(\frac{\omega_Q}{2} t_2) + 2] + \frac{1}{\sqrt{2}} \hat{T}_{21}(a) \sin(\frac{\omega_Q}{2} t_2) + \frac{2i}{\sqrt{15}} \hat{T}_{31}(s) [\cos(\frac{\omega_Q}{2} t_2) - 1] \end{aligned} \quad (111)$$

Still no triple quantum coherence can be obtained, thus, for convenience set $\frac{\omega_Q}{2} t_2 = \pi$:

$$\hat{\rho}(2) = \frac{-i}{5} \hat{T}_{11}(s) - \frac{4i}{\sqrt{15}} \hat{T}_{31}(s) \quad (112)$$

And apply a second hard rf-pulse

$$\hat{\rho}(3) = \frac{-i}{5} \hat{T}_{11}(s) - \frac{4i}{\sqrt{15}} [\frac{1}{8} \hat{T}_{31}(s) [5 \cos(2\omega_1 t_3) + 3] - \frac{1}{2} \sqrt{\frac{5}{2}} \hat{T}_{32}(a) \sin(2\omega_1 t_3) - \frac{\sqrt{15}}{8} \hat{T}_{33}(s) [\cos(2\omega_1 t_3) - 1]] \quad (113)$$

Define the pulse as $\pi/2_y$:

$$\hat{\rho}(3) = \frac{-i}{5} \hat{T}_{11}(s) + i \left[\frac{1}{\sqrt{15}} \hat{T}_{31}(s) - \hat{T}_{33}(s) \right] \quad (114)$$

The pulse sequence and the obtained coherence transfer pathways are shown in Figure 54.

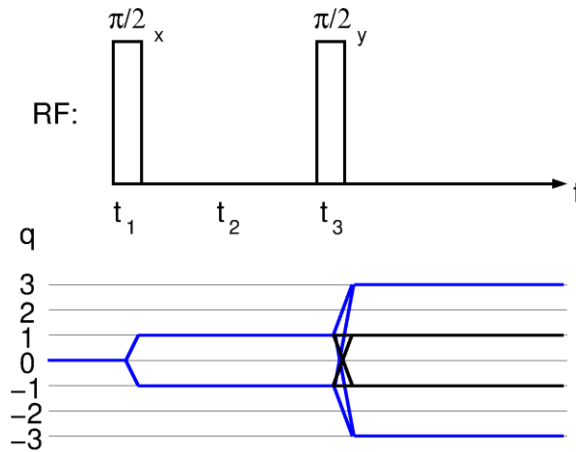


Figure 54 - Excitation of triple quantum coherence with two hard rf-pulses. Desired coherence transfer pathways are emphasized in blue.

Source: By the author.

Alternatively, it is possible to excite triple quantum coherence through application of a single long rf-pulse. In this case, the effect of the quadrupolar Hamiltonian \hat{H}_Q during the long pulse must be considered in addition to the rf Hamiltonian \hat{H}_1 . The combined effect was studied through numerical simulations with the MATLAB software. Therefore, for a given quadrupolar frequency ($\frac{\omega_Q}{2} = 400\text{Hz}$) the pulse length and the pulse intensity was varied. The results of the simulation are shown in Figure 55.

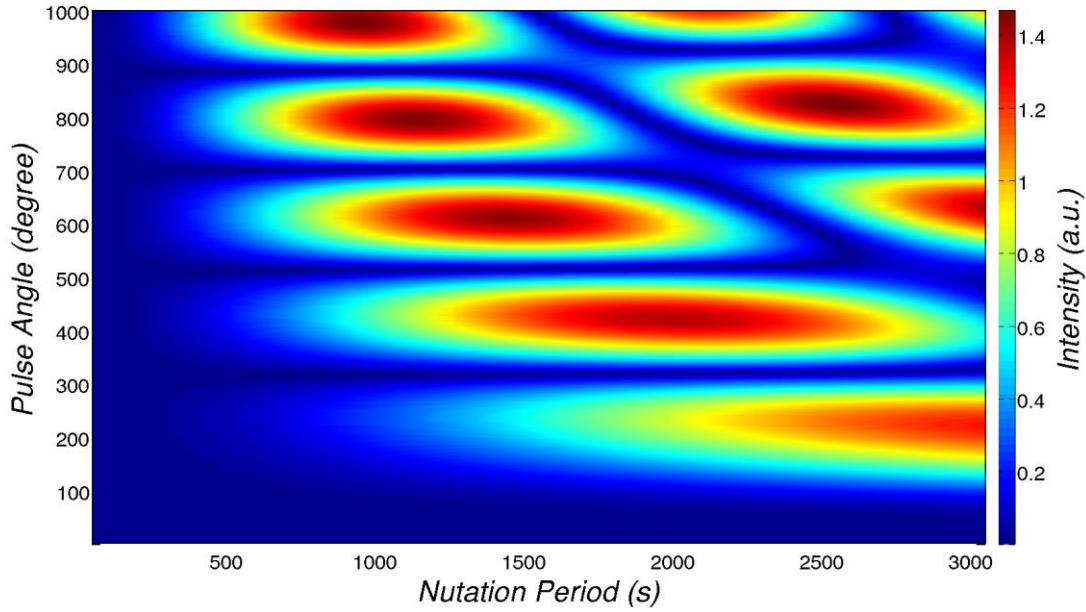


Figure 55 - Simulated 3Q coherence excitation profile for long rf-pulses under the effect of the quadrupolar effect as function of the pulse strength (given as nutation period) and the pulse length (given as flip angle). With a quadrupolar oscillation of $\omega_Q/2 = 400$ Hz.

Source: By the author.

4.3.3 Multiple Quantum Coherence Detection

Until now, nothing has been said regarding the detection of the multiple quantum coherences. Since only single quantum coherences can be measured experimentally, indirect methods to analyze the MQ excitation efficiency will be necessary. A final (hard) rf-pulse is necessary to transform MQ into detectable single quantum coherence. The desired pathway can be isolated through an appropriate phasecycle. Alternatively, the phase increment of the pulses (see equation (33), in section 2.2.1) can be stored in the second dimension and a subsequent Fourier Transform in this dimension will differentiate the magnetization from the distinct pathways. The minimum necessary phases for differentiate all components of the transfer pathway is given by a simple rule:

$$n \geq (\Delta q_{\max} - \Delta q_{\min}) + 1.$$

Figure 56 shows the possible coherence transfer pathways of the used pulse sequence. The phases of the first two pulses were maintained fixed, while the phase φ of the third pulse was varied. The minimum necessary phases to differentiate all possible pathways is $n = 2 - (-4) = 7$. However, in the experimental procedure a 16 step phase increment was performed with $\varphi = n \frac{360}{16}$. The Fourier transform separated the echoes from the different

coherence pathways successfully and the result is shown in Figure 56. The component with the largest intensity is observed at $\Delta q = -1$ and can be associated to the magnetization that relaxed with T_1 during t_4 . The echo of the $-3Q$ component is expected at a time $t < 0$, therefore, the observed intensity is only the echo tail and is smaller than that of the $+3Q$ component.

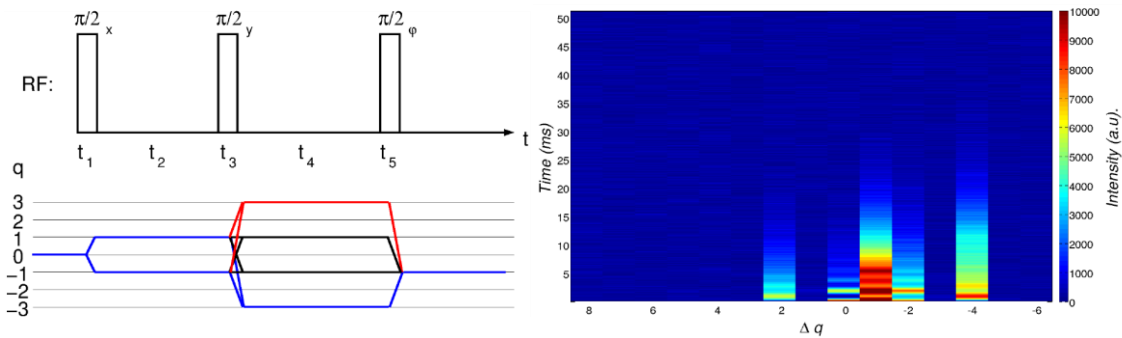


Figure 56 - Multiple quantum excitation and detection. Left, used experiment pulse sequence and quantum coherence pathways. Right, ^7Li measurement of PEGD ($y = 5$) at 50°C with $t_2 = 5.5$ ms, the Fourier transform of the phase increment of the third pulse separate the echoes of the different coherence pathways.

Source: By the author.

According to equation (111), and knowing that \hat{T}_{33} derives only from \hat{T}_{31} the observed $3Q$ coherence pathway is expected to oscillate with the quadrupolar frequency $\omega_Q/2$ as a function of the time between pulses (t_2 in Figure 56). In order to verify this behavior the maximum of the $3Q$ echo was measured for various t_2 . In Figure 57 the obtained results are plotted together with its Fourier transformation. The results are satisfactory and an oscillation of approximately 400 Hz was found.

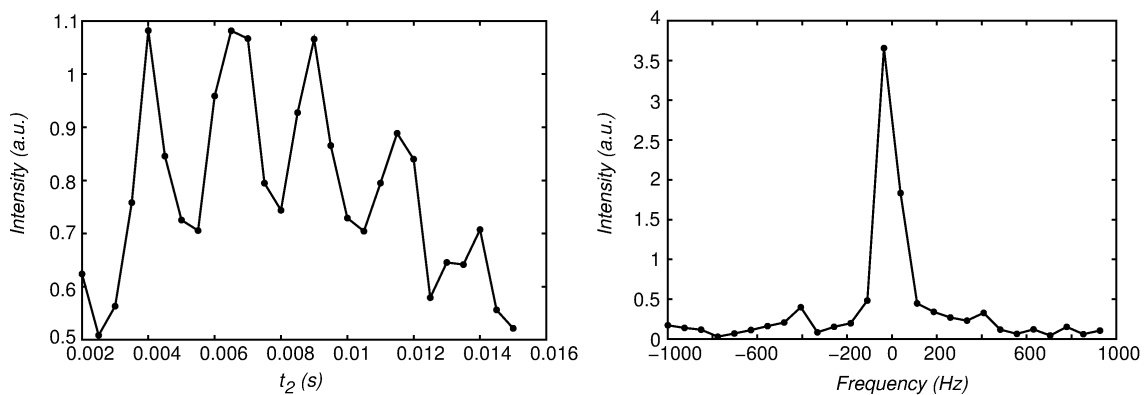


Figure 57 - ^7Li measurement of PEGD ($y = 5$) at 50°C . Left, absolute intensity of the echo of the $+3Q$ component for various times t_2 . Right, Fourier transform of the obtained oscillation.

Source: By the author.

Furthermore, also the single pulse excitation was analyzed. Therefore, firstly the 3Q excitation efficiency was studied. The pulse length was varied for various pulse strengths and compared to the simulated data. Constant pulse strength represents a vertical line in the 2D map shown in Figure 55. For better comparison the simulated data is plotted together with the experimental results in the same pulse length range and are shown in Figure 58. The results showed good agreement between experimental and simulated data. The largest intensity was obtained for a nutation period of $T_{\text{(nut)}} = 3000 \mu\text{s}$ and a pulse length of $2500 \mu\text{s}$. Furthermore, the obtained 3Q excitation efficiency was larger as compared to the one obtained by applying two hard rf-pulses and therefore this pulse was used for 3Q excitation in further experiments.

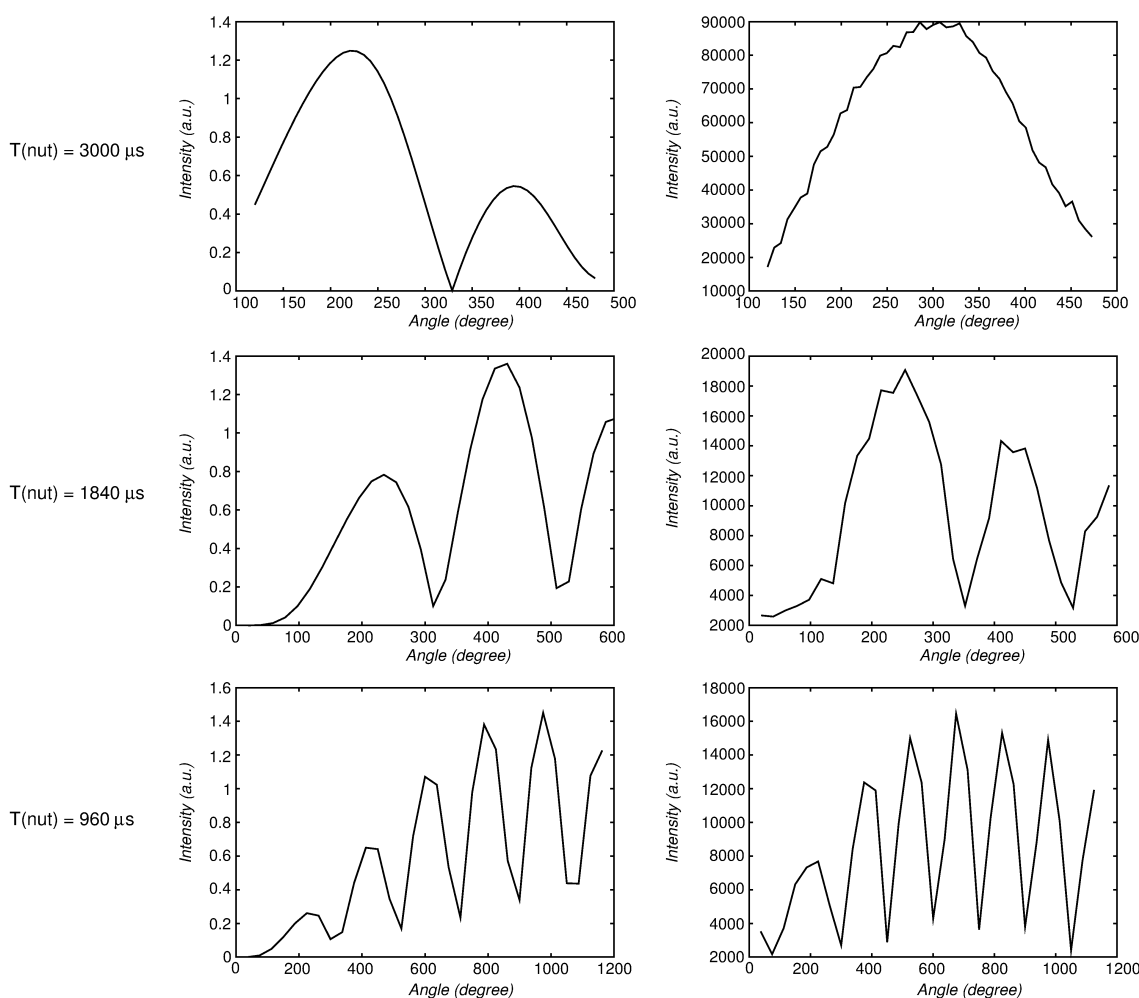


Figure 58 - Simulated (left) and measured (right) 3Q coherence excitation for long rf-pulses under the effect of the quadrupolar coupling ($\omega_Q = 400 \text{ Hz}$). Three different pulse strengths (given as nutation period) were applied and the pulse length (given as flip angle) was scanned. ^7Li measurements performed on PEGD ($\gamma = 5$) at 50°C .

Source: By the author.

In a next step, the free evolution of the 3Q component was studied. The phase gain of a 3Q component is three times faster than that of 1Q components. Thus, the echo of a

component that evolves during a time t_1 with 3Q coherence and is brought to -1Q coherence with a $\pi/2$ pulse is expected to appear at a time t_2 after the pulse of $t_2 = 3t_1$. This was successfully verified for various times t_1 and the results are shown in Figure 59.

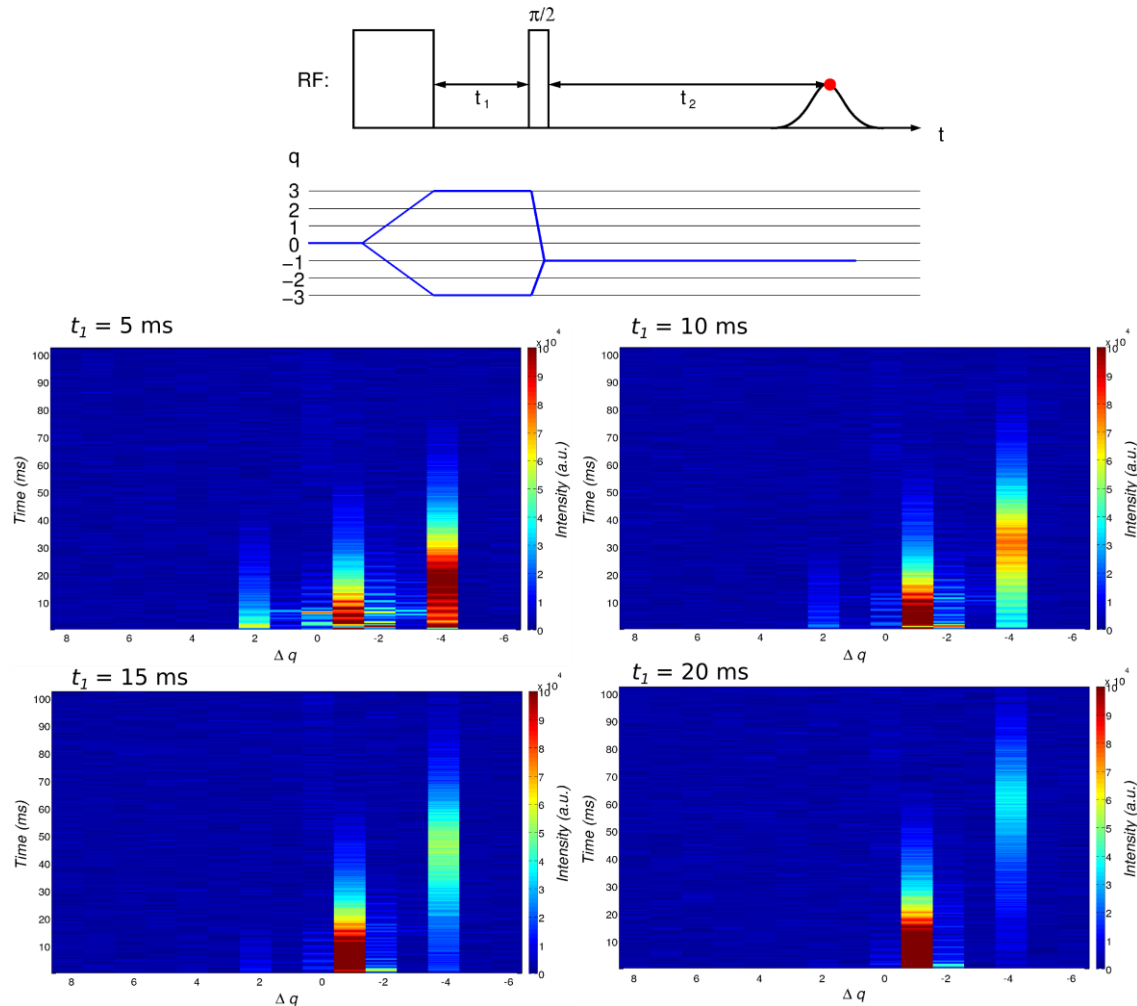


Figure 59 - ${}^7\text{Li}$ echo evolution of PEGD ($\gamma = 5$) at 50°C for $t_1 = 5, 10, 15$ and 20 ms of the pulse sequence shown on top. The component evolving with +3Q coherence appears at $\Delta q = -4$. The maximum of the echo of this component is always at a time $t_2 = 3t_1$.

Source: By the author.

4.3.4 Multiple Quantum Pulse Gradient Measurements

With the previously obtained knowledge on the manipulation of the spin system, 3Q pulse gradient measurements were performed. The diffusion measurements using 3Q coherences were done with a pulse sequence similar to that shown in Figure 21, but with some modifications, since 3Q excitation was done with a single pulse. The modified pulse sequence is shown in Figure 60. Single quantum diffusion measurements were performed

with the conventional Pulse Field Gradient Spin Echo (PFG-SE). The gradient application times were 20 and 30 ms respectively.

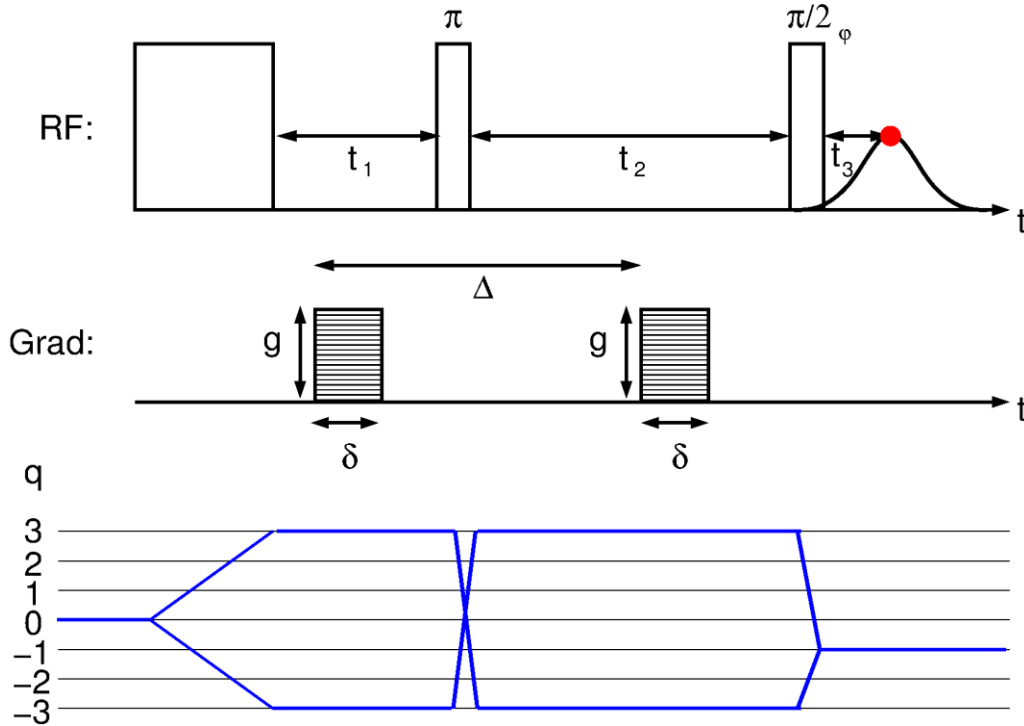


Figure 60 - Modified pulse sequence and coherence transfer pathway of the MQPGSE experiment for nuclei with spin 3/2. The desired coherence transfer pathway is emphasized in blue.

Source: By the author.

The obtained results were fitted with a single exponential decay. The Li^+ ion diffusion coefficient of PEGD doped with LiClO_4 ($\gamma = 5$) at 50°C obtained from the 1Q experiment was

$$D_{1Q} = 4.2 \cdot 10^{-12} \pm 0.2 \cdot 10^{-12} \frac{\text{m}^2}{\text{s}} \text{ and from the 3Q experiment } D_{3Q} = 3.6 \cdot 10^{-12} \pm 0.1 \cdot 10^{-12} \frac{\text{m}^2}{\text{s}}.$$

Thus, the deviation is larger than the error obtained from data processing, and both are

considerably larger than the value reported in literature $D_{lit} = 2 \cdot 10^{-12} \frac{\text{m}^2}{\text{s}}$. (53) A possible

error source could be the use of only a single exponential for fitting the obtained decay, for a reliable multi-exponential fit more points would be necessary.

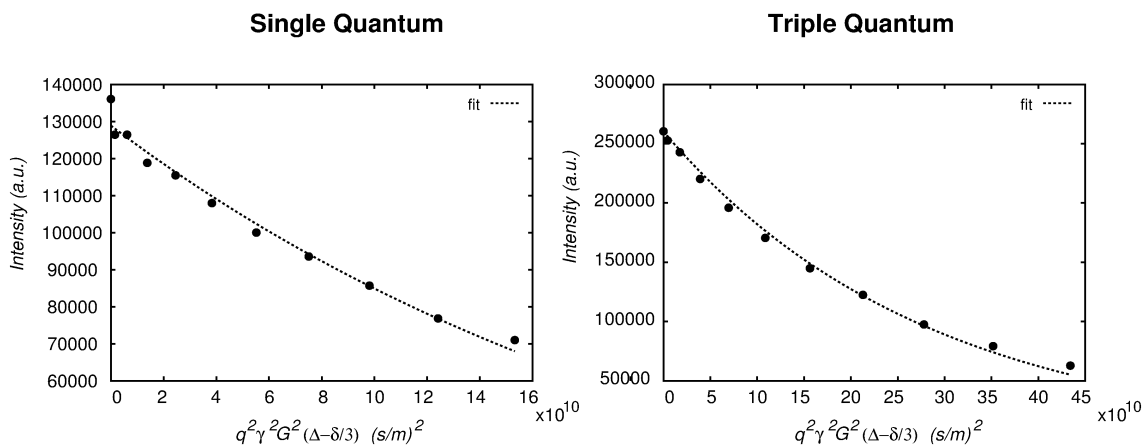


Figure 61 - ${}^7\text{Li}$ diffusion measurements of PEGD ($\gamma = 5$) at 50°C . Left, attenuation obtained from the conventional PFGSE experiment, $D_{1Q} = 4.2 \cdot 10^{-12} \pm 0.2 \cdot 10^{-12} \frac{\text{m}^2}{\text{s}}$. Right, attenuation obtained from the MQ variant of the diffusion experiment, using 3Q coherence, $D_{3Q} = 3.6 \cdot 10^{-12} \pm 0.1 \cdot 10^{-12} \frac{\text{m}^2}{\text{s}}$.

Source: By the author.

However, the consistency of the obtained values should be sufficient for showing that the MQPGSE experiment is a valuable option for measuring diffusion coefficients in this system. While the loss of signal intensity in the 3Q experiment as compared to the 1Q experiment also has to be considered, the factor three represents a considerable gain in the attenuation allowing to determine diffusion coefficients in cases where the instrumental gradient maximum may not be strong enough.

5 Conclusions and Outlook

The subject of this thesis was to study the ongoing molecular dynamics in ion conducting polymers through application of various NMR techniques. This work contributes to the field of solid polymer electrolytes by implementing and validating experiments that, to our knowledge, have not been used in this field so far, such as relaxation exchange or multiple quantum pulse field gradient experiments.

First, the implementation of NMR relaxometry techniques for the study of solid polymer electrolytes was analyzed. Therefore, ^7Li relaxation measurements were done on PEG/LiClO₄ and some promising results were obtained. T_1 and T_2 relaxation times clearly differentiated two types of Li^+ ions with different motional freedom in the amorphous phase. For all measured LiClO₄ doping amount more lithium ions had lower mobility, with a constant ratio of approximately 70:30. Mobility of the ions increase with increasing temperatures, as should be expected. The influence of the doping level on the ion mobility was studied and it was found that two opposite effects occur: first, reduction of crystallinity in the sample enhances the mobility of the polymer chains, and second, the presence of more solvated ions increases the polarity, thus the polymeric chains will be bonded stronger together, increasing their viscosity. The opposition of both effects causes that the sample with a doping ratio $y = 8$ presents a local maxima on the mobility, being the sample having the lowest amount of salt without the presence of a crystalline phase. This result implies that NMR relaxation measurements can help finding optimal doping ratios for solid polymer electrolytes.

Furthermore, T_2 exchange experiments have successfully been applied on the study of PEG/LiClO₄. Chemical exchange between the two ^7Li sites with different motional characteristics has been visualized and quantified exploiting their different relaxation times, in a way it would not have been possible with exchange spectroscopy due to their similar chemical shifts. The sample with a doping ratio of $y = 8$ has the lowest exchange rate. High mobility of the individual lithium ions does not imply high chemical exchange rates.

In a second part of this work, high-resolution solid-state NMR measurements were performed on the triblock copolymer PS-PEO-PS during a four month exchange at the *Iowa State University* in the group of Prof. Klaus Schmidt-Rohr. The samples were prepared by our collaborator Prof. Didier Gigmes and his group from the *Aix-Marseille Université*. Spin

diffusion measurements allowed determining the domain size of the triblock copolymers of lamellar morphology. Linewidth and $T_{1\rho}$ are sensible to variations of the dynamics in the system.

Following, the relaxometry techniques previously applied to PEG were also applied to study the dynamical properties of the lithium ions in the LiTFSI doped PS-PEO-PS system. It was shown that the Li^+ ions are localized in the amorphous regions of the PEO block presenting two different T_2 relaxation times in complete analogy to PEG/ LiClO_4 . Doping ratios and PS content do affect the mobility of the lithium ions. Comparing the $T_{1\rho}$ of the chains with the T_2 results of the Li^+ ions it was observed that a reduced mobility of the polymeric chains could be beneficial for increasing the mobility of the ions.

Finally, a pulse sequence that uses multiple quantum states for measuring translation diffusion was studied. Therefore, it was necessary to guaranty the efficiency of the used tools, which was done through simulations, and experimental analysis. The obtained knowledge allowed manipulating the spin system through the design of different experiments. Diffusion measurements using 3Q states were done on the ionic conductor PEGD doped with LiClO_4 . The results showed that MQ diffusion measurements are a valuable tool for measuring diffusion coefficients in case of a sample presenting short T_2 relaxation times and low diffusion coefficients.

During the elaboration of this thesis multiple scientific ramifications appeared, which would be appealing for future works, such as:

- Experimental confirmation of the origin of the two distinct lithium species. Therefore, an alternative interpretation of the results has to be further studied. It is possible that the origin of the two different encountered ^7Li relaxation times is not due to different motional properties of two distinct Li^+ ion species, but due to quadrupolar relaxation mechanisms. It has been reported in the literature, (83–85) that quadrupolar nuclei (with spin $I > 1$) in a system in which the relaxation is governed by the quadrupolar interactions and which is outside the extreme narrowing case the relaxation will present a multiexponential behavior. In case of a spin $I = 3/2$ the longitudinal and transverse magnetization F_1 and F_2 will reach their equilibrium with a biexponentially, according to: (85)

$$F_1 = \frac{1}{5} e^{-r_1 t} + \frac{1}{5} e^{-r_2 t}. \quad (115)$$

Where

$$r_1 = 2\sigma^2 J_1(\omega_0), \quad (116)$$

$$r_2 = 2\sigma^2 J_2(2\omega_0). \quad (117)$$

And

$$F_2 = \frac{3}{5} e^{-s_1 t} + \frac{2}{5} e^{-s_2 t}. \quad (118)$$

where

$$s_1 = \sigma^2 (J_0(0) + J_1(\omega_0)), \quad (119)$$

$$s_2 = \sigma^2 (J_1(\omega_0) + J_2(2\omega_0)). \quad (120)$$

Where σ^2 is the mean square of the angular quadrupole frequency. Since the predicted ratios are in good agreement with the obtained results, this theory is very promising for explaining the results obtained in this work.

A good approach to study this is by measuring ${}^6\text{Li}$, since ${}^6\text{Li}$ has a spin $I=1$ a monoexponential relaxation behavior is expected. A first measurement was done, and Figure 62 shows the spectra of ${}^6\text{Li}$ and ${}^7\text{Li}$ of PEG2000 with a doping ratio of $y=8$ under the same conditions. In contrast to the ${}^7\text{Li}$ spectrum, it is possible to fit the ${}^6\text{Li}$ spectrum with a single Lorentzian. This first experiment apparently confirms that the quadrupolar relaxation is responsible for the two encountered ${}^7\text{Li}$ relaxation times in the doped PEG monopolymers as well as in the doped triblock copolymers PS-PEO-PS, however more measurements will be necessary in order to definitively confirm this theory. Therefore in the next step, more measurements and a deeper theoretical study will become necessary in order to fully explain the ongoing processes, specially the measured exchange processes will have to be analyzed from a different perspective.

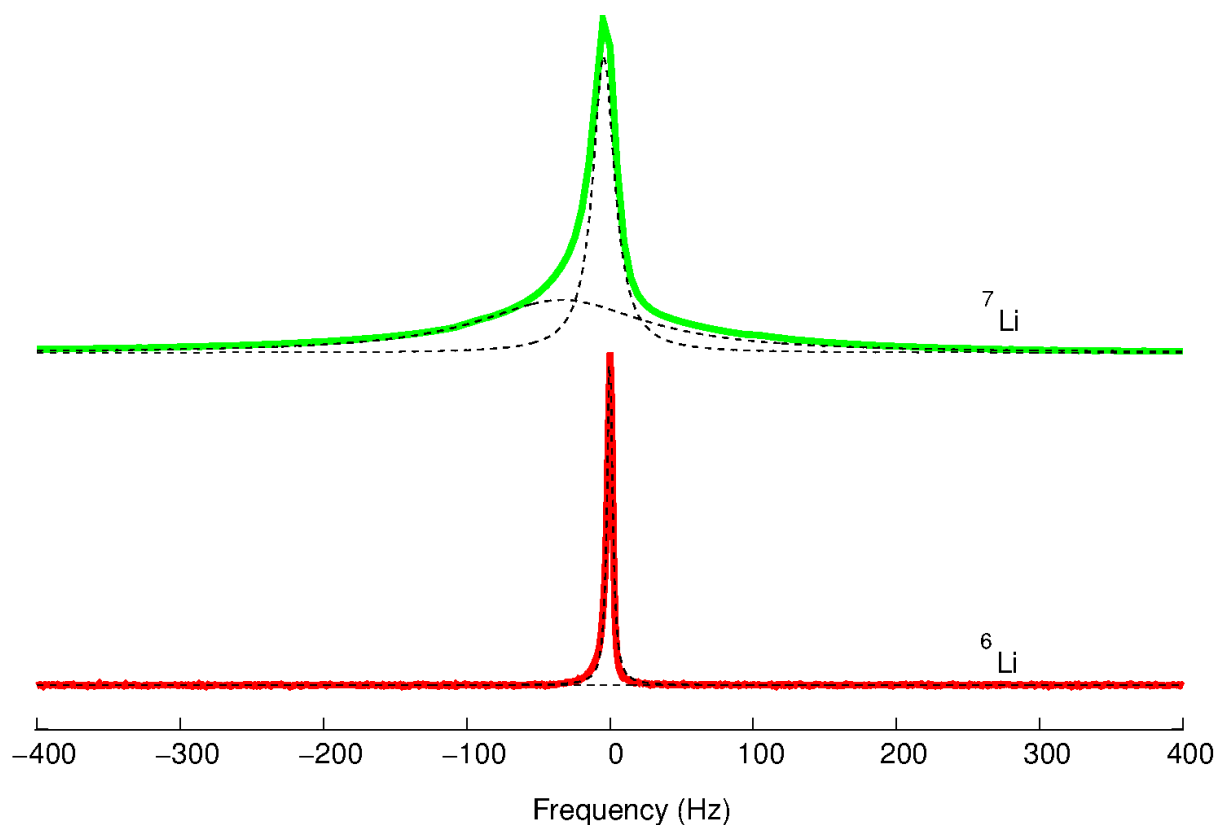


Figure 62 - ${}^7\text{Li}$ (green) and ${}^6\text{Li}$ (red) spectra obtained with 8 and 2048 scans respectively. Both measurements were performed with the same Varian 10-mm liquid probehead at a magnetic field of 9.4 T at room temperature. The ${}^7\text{Li}$ and ${}^6\text{Li}$ 90° pulses were 10 and 30 μs and the recycling delays 3 and 80 s, respectively. The ${}^7\text{Li}$ spectrum was fitted with a Lorentzian and a Gaussian curve, while the ${}^6\text{Li}$ spectrum was fitted with a single Lorentzian.

Source: By the author.

- Study T_2 relaxation time distributions and T_2 exchange of ${}^{13}\text{C}$ in PEG. First preliminary results showed the presence of exchange signals. Comparison with the ${}^7\text{Li}$ results will help understand further the ongoing processes of these materials.
- Study Li^+ ion mobility in the presence of complex crystalline PEO/Li-salt phases. First experiments done with PEO of molar mass $M_n = 1000000$ g/mol, doped with LiCF_3SO_3 showed at least four different T_2 relaxation times. Even though, it was not possible to chemically assign those sites, an exciting result was obtained from the $T_2 \times T_2$ exchange maps (Figure 63). Chemical exchange occurs only between two pairs of sites, implying two isolated systems. The NMR methodology presented in this thesis could offer a powerful tool to study these complex systems.

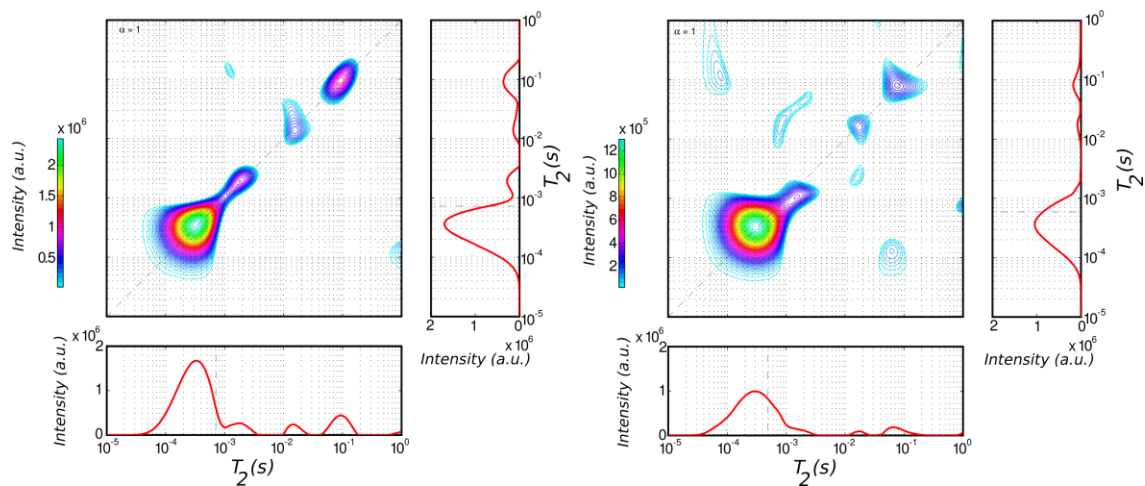


Figure 63 - 2D maps obtained from the ${}^7\text{Li}$ $T_2 \times T_2$ exchange experiment of the sample PEO1000000 doped with LiCF_3SO_3 ($y = 8$) for $\tau_m = 1$ (left) and 300 ms (right).

Source: By the author.

REFERENCES

- 1 NAZRI, G-A.; PISTOIA, G. **Lithium batteries: science and technology**. Boston: Kuwler Academic, 2003.
- 2 ARMAND, M.; TARASCON, J.M. Building better batteries. **Nature**, v. 451, n. 7179, p. 652–657, 2008.
- 3 TARASCON, J.M.; ARMAND, M. Issues and challenges facing rechargeable lithium batteries. **Nature**, v. 414, n. 6861, p. 359-367, 2001.
- 4 SINGH, M.; ODUSANYA, O.; WILMES, G.M.; EITOUNI, H.B.; GOMEZ, E.D.; PATEL, A.J.; CHEN, V.L.; PARK, M.J.; FRAGOULI, P.; IATROU, H.; HADJICHRISTIDIS, N.; COOKSON, D.; BALSARA, N.P. Effect of molecular weight on the mechanical and electrical properties of block copolymer electrolytes. **Macromolecules**, v. 40, n. 13, p. 4578–4585, 2007.
- 5 FENTON, D.E.; PARKER, J.M.; WRIGHT, P.V. Complexes of alkali metal ions with poly(ethylene oxide). **Polymer**, v. 14, n. 11, p. 589, 1973.
- 6 ARMAND, M.B. Polymer electrolytes. **Annual Review of Materials Research**, v. 16, p. 245–261, 1986.doi: 10.1146/annurev.ms.16.080186.001333.
- 7 GRAY, F.M. **Solid polymer electrolytes: fundamentals and technological applications**. New York: VCH Publishers, 1991.
- 8 APPETECCHI, G.B.; CROCE, F.; MARASSI, R.; PERSI, L.; ROMAGNOLI, P.; SCROSATI, B. Lithium insertion into carbonaceous materials and transition metal oxides from high performance polymer electrolytes. **Electrochimica Acta**, v. 45, n. 1, p. 23–30, 1999.
- 9 SONG, J.Y.; WANG, Y.Y.; WAN, C.C. Review of gel-type polymer electrolytes for lithium-ion batteries. **Journal of Power Sources**, v. 77, n. 2, p. 183–197, 1999.
- 10 JUDEINSTEIN, P.; REICHERT, D.; DEAZEVEDO, E.R.; BONAGAMBA, T.J. NMR multi-scale description of ionic conductivity mechanisms inside polymer electrolytes. **Acta Chimica Slovenica**, v. 52, n. 4, p. 349–360, 2005.
- 11 BOUCHET, R.; MARIA, S.; MEZIANE, R.; ABOULAICH, A.; LIENAFI, L.; BONNET, J.; PHAN, T.N.T.; BERTIN, D.; GIGMES, D.; DEVAUX, D.; DENOYEL, R.; ARMAND, M. Single-ion BAB triblock copolymers as highly efficient electrolytes for lithium-metal batteries. **Nature Materials**, v. 12, n. 5, p. 452–457, 2013.
- 12 MURATA, K.; IZUCHI, S.; YOSHIHISA, Y. An overview of the research and development of solid polymer electrolyte batteries. **Electrochimica Acta**, v. 45, n. 8-9, p. 1501–1508, 2000.

- 13 PANDAY, A.; MULLIN, S.; GOMEZ, E.D.; WANAKULE, N.; CHEN, V.L.; HEXEMER, A.; POPLE, J.; BALSARA, N.P. Effect of molecular weight and salt concentration on conductivity of block copolymer electrolytes. **Macromolecules**, v. 42, n. 13, p. 4632–4637, 2009.
- 14 GOMEZ, E.D.; PANDAY, A.; FENG, E.H.; CHEN, V.; STONE, G.M.; MINOR, A.M.; KISIELOWSKI, C.; DOWNING, K.H.; BORODIN, O.; SMITH, G.D.; BALSARA, N.P. Effect of ion distribution on conductivity of block copolymer electrolytes. **Nano Letters**, v. 9, n. 3, p. 1212–1216, 2009.
- 15 TERAN, A.A.; BALSARA, N.P. Thermodynamics of block copolymers with and without salt. **Journal of Physical Chemistry B**, v. 118, n. 1, p. 4–17, 2014.
- 16 BONK, F.A.; CALDARELLI, S.; PHAN, T.; BERTIN, D.; DEAZEVEDO, E.R.; MANTOVANI, G.L.; BONAGAMBA, T.J.; PLIVELIC, T.S.; TORRIANI, I.L. Investigation by combined solid-state NMR and SAXS methods of the morphology and domain size in polystyrene- b- polyethylene oxide- b- polystyrene triblock copolymers. **Journal of Polymer Science B: polymer physics**, v. 48, n. 1, p. 55–64, 2010.
- 17 PERRIN, L.; PHAN, T.N.T.; QUERELLE, S.; DERATANI, A.; BERTIN, D. Polystyrene-block-poly(ethylene oxide)-block-polystyrene: A new synthesis method using nitroxide-mediated polymerization from poly(ethylene oxide) macroinitiators and characterization of the architecture formed. **Macromolecules**, v. 41, n. 19, p. 6942–6951, 2008.
- 18 ROLLET, M.; PELLETIER, B.; ALTOUNIAN, A.; BEREK, D.; MARIA, S.; BEAUDOIN, E.; GIGMES, D. Separation of parent homopolymers from polystyrene- b - poly(ethylene oxide)- b -polystyrene triblock copolymers by means of liquid chromatography: 1. comparison of different methods. **Analytical Chemistry**, v. 86, n. 5, p. 2694–2702, 2014.
- 19 DUER, J.M. **Solid-state NMR spectroscopy: principles and applications**. Oxford: Blackwell Science Ltd, 2002.
- 20 BÖHMER, R.; JEFFREY, K.R.; VOGEL, M. Solid-state Li NMR with applications to the translational dynamics in ion conductors. **Progress in Nuclear Magnetic Resonance Spectroscopy**, v. 50, n. 2-3, p. 87-174, 2007.
- 21 BAIN, A.D. Chemical exchange in NMR. **Progress in Nuclear Magnetic Resonance Spectroscopy**, v. 43, n. 3-4, p. 63–103, 2003.
- 22 CARR, H.Y.; PURCELL, E.M. Effects of diffusion on free precession in nuclear magnetic resonance experiments. **Physical Review**, v. 94, n. 3, p. 630–638, 1954.
- 23 MEIBOOM, S.; GILL, D. Modified spin-echo method for measuring nuclear relaxation times. **Review of Scientific Instruments**, v. 29, n. 8, p. 688–691, 1958.
- 24 WASHBURN, K.E.; CALLAGHAN, P.T. Tracking pore to pore exchange using relaxation exchange spectroscopy. **Physical Review Letters**, v. 97, n. 17, p. 175502, 2006.

- 25 MITCHELL, J.; GRIFFITH, J.D.; COLLINS, J.H.P.; SEDERMAN, A.J.; GLADDEN, L.F.; JOHNS, M.L. Validation of NMR relaxation exchange time measurements in porous media. **Journal of Chemical Physics**, v. 127, n. 23, p. 234701, 2007.
- 26 DORTCH, R.D.; HORCH, R. A.; DOES, M.D. Development, simulation, and validation of NMR relaxation-based exchange measurements. **Journal of Chemical Physics**, v. 131, n. 16, p. 164502, 2009.
- 27 D'EURYDICE, M.N.; MONTRAZI, E.T.; FORTULAN, C.A.; BONAGAMBA, T.J. T2-filtered T2 – T2 exchange NMR. **Journal of Chemical Physics**, v. 144, n. 20, p. 204201, 2016.
- 28 FLEURY, M.; SOUALEM, J. Quantitative analysis of diffusional pore coupling from T2-store-T2 NMR experiments. **Journal of Colloid and Interface Science**, v. 336, n. 1, p. 250–259, 2009.
- 29 CODD, S.L.; VOGT, S.J.; HORNEMANN, J.A.; PHILLIPS, A.J.; MANEVAL, J.E.; ROMANENKO, K.R.; HANSEN, L.; CUNNINGHAM, A.B.; SEYMOUR, J.D. NMR relaxation measurements of biofouling in model and geological porous media. **Organic Geochemistry**, v. 42, n. 8, p. 965–971, 2011.
- 30 MONTEILHET, L.; KORB, J.P.; MITCHELL, J.; MCDONALD, P.J. Observation of exchange of micropore water in cement pastes by two-dimensional T2 - T2 nuclear magnetic resonance relaxometry. **Physical Review E**, v. 74, n. 6, p. 061404, 2006.
- 31 HORCH, R.A.; NYMAN, J.S.; GOCHBERG, D.F.; DORTCH, R.D.; DOES, M.D. Characterization of 1H NMR signal in human cortical bone for magnetic resonance imaging. **Magnetic Resonance in Medicine**, v. 64, n. 3, p. 680–687, 2010.
- 32 DORTCH, R.D.; HARKINS, K.D.; JUTTUKONDA, M.R.; GORE, J.C.; DOES, M.D. Characterizing inter-compartmental water exchange in myelinated tissue using relaxation exchange spectroscopy. **Magnetic Resonance in Medicine**, v. 70, n. 5, p. 1450–1459, 2013.
- 33 HORCH, R.A.; GORE, J.C.; DOES, M.D. Origins of the ultrashort-T2 1H NMR signals in myelinated nerve: A direct measure of myelin content? **Magnetic Resonance in Medicine**, v. 66, n. 1, p. 24–31, 2011.
- 34 FECHETE, R.; DEMCO, D.E.; ZHU, X.; TILLMANN, W.; MÖLLER, M. Water states and dynamics in perfluorinated ionomer membranes by 1H one- and two-dimensional NMR spectroscopy, relaxometry, and diffusometry. **Chemical Physics Letters**, v. 597, n. 1, p. 6–15, 2014.
- 35 CHEUNG, I.W.; CHIN, K.B.; GREENE, E.R.; SMART, M.C.; ABBRENT, S.; GREENBAUM, S.G.; PRAKASH, G.K.S.; SURAMPUDI, S. Electrochemical and solid state NMR characterization of composite PEO-based polymer electrolytes. **Electrochimica Acta**, v. 48, n. 14-16, p. 2149–2156, 2003.

- 36 HAYAMIZU, K.; AIHARA, Y.; ARAI, S.; PRICE, W.S. Self-diffusion coefficients of lithium, anion, polymer, and solvent in polymer gel electrolytes measured using ^7Li , ^{19}F , and ^1H pulsed-gradient spin-echo NMR. **Electrochimica Acta**, v. 45, n. 8-9, p. 1313–1319, 2000.
- 37 DAM, L. VAN; ANDREASSON, B.; NORDENSKIÖLD, L. Multiple-quantum pulsed gradient NMR diffusion experiments on quadrupolar ($I > 1/2$) spins. **Chemical Physics Letters**, v. 262, n. 6, p. 737–743, 1996.
- 38 KUCHEL, P.W.; CHAPMAN, B.E. Heteronuclear double-quantum-coherence selection with magnetic-field gradients in diffusion experiments. **Journal of Magnetic Resonance, Series A**, v. 101, n. 1, p. 53–59, 1993.
- 39 LIU, M.; MAO, X.-A.; YE, C.; NICHOLSON, J.K.; LINDON, J.C. Enhanced effect of magnetic field gradients using multiple quantum NMR spectroscopy applied to self-diffusion coefficient measurement. **Molecular Physics**, v. 93, n. 6, p. 913–920, 1998.
- 40 CAI, C.; CHEN, Z.; CAI, S.; HWANG, L.P.; ZHONG, J. Finite difference simulation of diffusion behaviors under inter- and intra-molecular multiple-quantum coherences in liquid NMR. **Chemical Physics Letters**, v. 407, n. 4-6, p. 438-443, 2005.
- 41 CALLISTER, W.D.; RETHWISCH, D.G. **Fundamentals of materials science and engineering: an integrated approach**. Hoboken: John Wiley & Sons, Inc, 2012.
- 42 SCHMIDT-ROHR, K.; SPIESS, H. **Multidimensional solid-state NMR and polymers**. London: Academic Press, 1994.
- 43 ABETZ, V.; GOLDACKER, T. Formation of superlattices via blending of block copolymers. **Macromolecular Rapid Communications**, v. 21, n. 1, p. 16-34, 2000.
- 44 BERTHIER, C.; GORECKI, W.; MINIER, M.; ARMAND, M.; CHABAGNO, J.; RIGAUD, P. Microscopic investigation of ionic conductivity in alkali metal salts-poly(ethylene oxide) adducts. **Solid State Ionics**, v. 11, n. 1, p. 91-95, 1983.
- 45 VINCENT, C.A. Polymer electrolytes. **Progress in Solid State Chemistry**, v. 17, n. 3, p. 145–261, 1987.
- 46 FULLERTON-SHIREY, S.K.; MARANAS, J.K. Effect of LiClO_4 on the structure and mobility of PEO-based solid polymer electrolytes. **Macromolecules**, v. 42, n. 6, p. 2142–2156, 2009.
- 47 GUPTA, S.; SHAHI, K.; BINESH, N.; BHAT, S. Investigation of the $(\text{PEG})_x\text{LiCl}$ system using conductivity, DSC and NMR techniques. **Solid State Ionics**, v. 67, n. 1-2, p. 97–105, 1993.
- 48 O’GARA, J.F.; NAZRI, G.; MACARTHUR, D. A carbon-13 and lithium-6 nuclear magnetic resonance study of lithium perchlorate/poly (ethylene oxide) electrolytes. **Solid State Ionics**, v. 47, n. 1-2, p. 87–96, 1991.
- 49 SHI, J.; VINCENT, C. The effect of molecular weight on cation mobility in polymer electrolytes. **Solid State Ionics**, v. 60, n. 1-3, p. 11-17, 1993.

- 50 SANGIORGE, C.L.; GOULART SILVA, G.; OLIVEIRA, A.L.; PIMENTA, M.A.; DAMASCENO, O.D.O.; SILVA, R.A. Raman scattering in complexed poly(ethylene glycol-400) distearate-lithium perchlorate systems. **Solid State Ionics**, v. 92, n. 1-2, p. 151–154, 1996.
- 51 OLIVEIRA, A.L.; DAMASCENO, O.D.; SILVA, P.R.; SANGIORGE, C.L.; DONOSO, J.P.; BONAGAMBA, T.J. Disorder model for specific conductivity of lithium perchlorate dissolved in poly(ethylene glycol-400) distearate. **Electrochimica Acta**, v. 42, n. 6, p. 929–935, 1997.
- 52 GIOTTO, M. V.; SANGIORGE, C.L.; HARRIS, D.J.; OLIVEIRA, A.L.; SCHMIDT-ROHR, K.; BONAGAMBA, T.J. Phase behavior and dynamics of the ABA triblock copolymer poly(ethylene glycol) distearate doped with alkali metal salts. **Macromolecules**, v. 35, n. 9, p. 3576–3583, 2002.
- 53 ALVES-SANTOS, M.; DEAZEVEDO, E.R.; VIDOTO, E.L.G.; MANTOVANI, G.L.; RABBANI, S.R.; BONAGAMBA, T.J. ^7Li NMR diffusion coefficient measurements on the Li^+ -doped ABA triblock copolymer poly(ethylene glycol) distearate. **Solid State Ionics**, v. 176, n. 11-12, p. 1123–1129, 2005.
- 54 LEVITT, M.H. **Spin dynamics**. Chichester: John Wiley & Sons Ltd, 2008.
- 55 GÜNTHER, H. **NMR-spektroskopie: eine einföhrung**. Stuttgart: Verlag, Thieme, 1973.
- 56 BODENHAUSEN, G.; KOGLER, H.; ERNST, R.R. Selection of coherence-transfer pathways in NMR pulse experiments. **Journal of Magnetic Resonance (1969)**, v. 58, n. 3, p. 370–388, 1984.
- 57 MEHRING, M. **Principles of high resolution NMR in solids**. New York: Springer-Verlag, 1983.
- 58 BOWDEN, G.J.; HUTCHISON, W.D. Tensor operator formalism for multiple-quantum NMR. 1. spin-1 nuclei. **Journal of Magnetic Resonance (1969)**, v. 67, n. 3, p. 403–414, 1986.
- 59 BOWDEN, G.J.; HUTCHISON, W.D.; KHACHAN, J. Tensor operator formalism for multiple-quantum NMR. 2. Spins $3/2$, 2 , and $5/2$ and general I. **Journal of Magnetic Resonance (1969)**, v. 67, n. 3, p. 415–437, 1986.
- 60 TELES, J. **Tomografia de estado quântico via ressonância magnética nuclear através de rotações globais do sistema de spins**. 2007. 190p. Tese (Doutorado em Ciências) - Instituto de Física de São Carlos, Universidade de São Paulo, São Carlos, 2007.
- 61 GOLDMAN, M.; SHEN, L. Spin-spin relaxation in LaF_3 . **Physical Review**, v. 144, n. 1, p. 321–331, 1966.

62 BUDA, A.; DEMCO, D.E.; BERTMER, M.; BLÜMICH, B.; REINING, B.; KEUL, H.; HÖCKER, H. Domain sizes in heterogeneous polymers by spin diffusion using single-quantum and double-quantum dipolar filters. **Solid State Nuclear Magnetic Resonance**, v. 24, n. 1, p. 39–67, 2003.

63 CALLAGHAN, P.T. **Principles of nuclear magnetic resonance microscopy**. Oxford: Clarendon Press, 1991.

64 BLOEMBERGEN, N.; PURCELL, E.; POUND, R. Relaxation effects in nuclear magnetic resonance absorption. **Physical Review**, v. 73, n. 7, p. 679–712, 1948.

65 SLICHTER, C.P. **Principles of magnetic resonance**. New York: Harper & Row, 1963.

66 KEELER, J. **Understanding NMR spectroscopy**. Chichester: John Wiley & Sons Ltd, 2005.

67 KOWALEWSKI, J.; MAELER, L. **Nuclear spin relaxation in liquids: theory, experiments and applications**. New York: Taylor and Francis, 2006.

68 ABRAGAM, A. **The principles of nuclear magnetism**. Oxford: Oxford University Press, 1961.

69 BLOCH, F. Nuclear induction. **Physical Review**, v. 70, n. 7-8, p. 460–474, 1946.

70 CAVANAGH, J.; FAIRBROTHER, W.J.; PALMER III, A.G.; RANCE, M.; SKELTON, N.J. **Protein NMR spectroscopy: principles and practice**. San Diego: Elsevier Academic Press, 2007.

71 MCCONNELL, H.M. Reaction rates by nuclear magnetic resonance. **Journal of Chemical Physics**, v. 28, n. 3, p. 430, 1958.

72 HAHN, E. Spin echoes. **Physical Review**, v. 80, n. 4, p. 580–594, 1950.

73 SONG, Y.-Q.; VENKATARAMANAN, L.; HÜRLIMANN, M.D.; FLAUM, M.; FRULLA, P.; STRALEY, C. T1–T2 correlation spectra obtained using a fast two-dimensional laplace inversion. **Journal of Magnetic Resonance**, v. 154, n. 2, p. 261–268, 2002.

74 PRICE, W.S. Pulsed-field gradient nuclear magnetic resonance as a tool for studying translational diffusion: part 1. basic theory. **Concepts in Magnetic Resonance**, v. 9, n. 5, p. 299–336, 1997.

75 STEJSKAL, E.O.; TANNER, J.E. Spin diffusion measurements: spin echoes in the presence of a time-dependant field gradient. **Journal of Chemical Physics**, v. 42, n. 1, p. 288–292, 1965.

76 TANNER, J.E. Use of the stimulated echo in NMR diffusion studies. **Journal of Chemical Physics**, v. 52, n. 5, p. 2523–2526, 1970.

77 ERNST, R.R.; BODENHAUSEN, G.; WOKAUN, A. **Principles of nuclear magnetic resonance in one and two dimensions**. Oxford: Clarendon Press, 1987.

78 WUNDERLICH, B. **Macromolecular physics**: crystal melting. New York: Academic Press, 1980. v.3.

79 SINGH, T.J.; BHAT, S. V. Morphology and conductivity studies of a new solid polymer electrolyte: (PEG)_xLiClO₄. **Bulletin of Materials Science**, v. 26, n. 7, p. 707–714, 2003.

80 ASANO, A.; TAKEGOSHI, K.; HIKICHI, K. ¹³C CP/MAS and ⁷Li NMR study of lithium perchlorate/poly(ethylene oxide). **Polymer Journal**, v. 31, n. 7, p. 602–608, 1999.

81 ASANO, A.; TAKEGOSHI, K.; HIKICHI, K. ¹³C CP/MAS NMR study on the miscibility and phase separation of a polystyrene/poly(vinyl methyl ether) blend. **Polymer**, v. 35, n. 26, p. 5630–5636, 1994.

82 JOHANSSON, A.; TEGENFELDT, J. Segmental mobility in complexes of Pb(CF₃SO₃)₂ and poly(ethylene oxide) studied by NMR spectroscopy. **Journal of Chemical Physics**, v. 104, n. 13, p. 5317, 1996.

83 HUBBARD, P.S. Nonexponential nuclear magnetic relaxation by quadrupole interactions. **Journal of Chemical Physics**, v. 985, n. 1970, p. 14–17, 1985.

84 WITSCHAS, M.; ECKERT, H. ³¹P and ²³Na solid-state NMR studies of cation dynamics in HT-sodium orthophosphate and the solid solutions (Na₂SO₄)_x-(Na₃PO₄)_{1-x}. **Journal of Physical Chemistry A**, v. 103, n. 1, p. 10764–10775, 1999.

85 WOESSNER, D. E. NMR Relaxation of spin-3/2 nuclei: effects of structure, order, and dynamics in aqueous heterogeneous systems. **Concepts in Magnetic Resonance**, v. 13, n. 5, p. 294–325, 2001.